Reinventing the Wheel

A Simulation-Aided Design of a Soft, Shape-Adapting, Lugged Wheel for Locomotion on Sandy Terrains

P. Klaassen

Delft University of Technology

TU Delft

Reinventing the Wheel

A Simulation-Aided Design of a Soft, Shape-Adapting, Lugged Wheel for Locomotion on Sandy Terrains

by

P. Klaassen

Master Thesis

in partial fulfilment of the requirements for the degree of

Master of Science
in Mechanical Engineering

at the Department Maritime and Transport Technology of Faculty Mechanical Engineering of Delft University of Technology
to be defended publicly on Friday June 20, 2025 at 2:00 PM

Student number:	5132428	
MSc track:	Multi-Machine Engineering	
Report number:	2025.MME.9059	
Supervisor:	Dr. H. Shi	TU Delft, Mechanical Engineering
Thesis committee chair:	Dr. J. Jovanova	TU Delft, Mechanical Engineering
Thesis committee member:	Prof. dr. ir. D.L. Schott	TU Delft, Mechanical Engineering
Date:	June 20, 2025	

TU Delft

Preface

This thesis presents the work I have done over the past nine months, marking the conclusion of my Master's degree in Mechanical Engineering at Delft University of Technology. Besides, it marks the end of my time as a student, after six years of studying in Delft. This journey has been both enriching and rewarding. I am grateful for the knowledge I have acquired and for the many valuable opportunities that have come my way.

I am pleased to have completed my Master's in Mechanical Engineering with a design project where I had the unique opportunity to reinvent the wheel. As part of this project, I also developed a physical prototype of my design. It has been incredibly rewarding to see my design come to life.

I would like to express my sincere gratitude to my supervisors, Hao Shi and Jovana Jovanova for their guidance and constructive feedback throughout this project. They have always believed in the project and in the ultimate goal of building a prototype. I also would like to extend my thanks to Vittorio Garofano for his insightful discussions and assistance in selecting the actuators and electronics of the prototype.

I also would like to thank my family and friends for their support during this project. I would especially like to thank my roommates of KonQ for their support and the wonderful memories shared over these six years of study. I am grateful to my girlfriend for her encouragement, creative design ideas, and her patience in listening to my technical explanations. Finally, I am deeply grateful to God for the talents he has given me and for his guidance along the way.

Pim Klaassen
Delft, June 2025

Abstract

Locomotion over granular terrain poses significant challenges for autonomous robotic systems, particularly in coastal regions characterized by loose, shifting sands. These sandy surfaces exhibit unpredictable behaviour, alternating between solid-like and fluid-like states, making movement across them particularly difficult. Ensuring reliable mobility on such terrains is essential for tasks like environmental monitoring, infrastructure inspection, and search-and-rescue missions. This thesis presents a simulation-aided design approach to develop a soft, shape-adapting, wheeled locomotion system optimized for sandy terrains. A co-simulation framework combining the discrete element method (DEM) and multibody dynamics (MBD) is employed to simulate the locomotion of a wheeled robot on varying sandy soils, covering both dry and wet sandy soil conditions. DEM models individual sand particles and their contact interactions, while MBD captures the robot's motion and mechanical behaviour. Using this approach, a shape-adapting wheel was designed with inflatable soft elements placed between rigid lugs. The inflation state changes the wheel geometry, allowing it to adapt to different terrain conditions. The wheel can transform between a lugged configuration for increased traction and a circular configurations for smoother travel. The robot prototype, built around this wheel concept, was evaluated in simulations on various sandy soils, including dry, wet, and very wet sand. Additionally, the prototype was evaluated in simulations on different terrain configurations, such as slopes and obstacles. Simulation results demonstrate improved performance of the shape-adapting wheels across a variety of sandy terrains, including slopes and obstacles. Integrating softness into the wheel improves obstacle climbing performance, while a lugged wheel configuration performs particularly well on loose, dry sandy slopes. Overall, the DEM-MBD co-simulation framework offers a powerful tool for evaluating and optimizing robotic locomotion strategies in granular environments. It enables rapid iteration of design configurations without the need for extensive physical prototyping, reducing development time and cost.

Contents

List of Figures

List of Tables

Nomenclature

Abbreviations

CAD	computer-aided design
CMS	component mode synthesis
COG	centre of gravity
COT	cost of transport
CPR	counts per revolution
DC	direct current
DD	dynamic domain
DEM	discrete element method
DOF	degree of freedom
EEPA	Edinburgh-Elasto-Plastic-Adhesive
FEM	finite element method
JKR	Johnson-Kendall-Roberts
KonQ	Kings on Queens
KPI	key performance indicator
LiPo	lithium-ion polymer
MBD	multibody dynamics
PB	periodic boundary
PLA	polyactic acid
PWM	pulse-width modulation
RFT	resistive force theory
RPM	revolutions per minute

Symbols

γ_s	surface energy
λ_p	contact plasticity ratio
μ	coefficient of friction
μ_r	particle-particle coefficient of rolling friction
μ_s	particle-particle coefficient of static friction
μ_{rg}	particle-geometry coefficient of rolling friction

μ_{sg}	particle-geometry coefficient of static friction
ν	particle Poisson's ratio
ν_g	geometry Poisson's ratio
ω	motor rotational speed
ω_0	motor no-load speed
ω_w	wheel angular velocity
ϕ	internal friction angle
ρ	particle density
ρ_g	geometry density
τ_m	motor torque
τ_s	motor stall torque
COT	cost of transport
D	damping coefficient
e	particle-particle coefficient of restitution
e_g	particle-geometry coefficient of restitution
G	particle shear modulus
g	gravitational constant
G_g	geometry shear modulus
K	spring stiffness coefficient
l_l	lug length
l_s	rupture distance
m_r	mass of the robot
P	power consumption
r_w	wheel radius
s	slip ratio
v_r	robot velocity
v_w	wheel linear velocity

Chapter 1

Introduction

Locomotion on granular terrain has been a long-standing challenge in both space exploration and terrestrial applications. One of the most iconic examples is the Moon, where lunar soil poses significant difficulties for robotic and crewed mobility due to its fine, loosely packed particles, low gravity, and lack of atmospheric cohesion. Lunar soil behaves unpredictably. It can offer resistance under compression, but it easily shifts or collapses when pushed or disturbed repeatedly. Rovers and landers operating in such environments often face the risk of entrapment, as was famously the case with NASA's Spirit rover on Mars, which became permanently stuck in soft soil. Figure 1.1 illustrates two robotic systems developed for navigating and exploring loose, granular terrain in space exploration. These systems are combining wheeled and legged locomotion into a integrated wheel-leg system, where the wheels are attached at the end of the legs. The flexibility of the leg allows adaptation to different terrains and obstacles.

(a) Wheeled-leg rover SherpaTT. Adapted from [1].

(b) Resource Prospector 15 (RP15) wheeled-leg rover from NASA. Adapted from [2].

Figure 1.1: Examples of lunar rover systems for locomotion on loose, granular lunar terrain.

The insights and technologies developed to address locomotion on lunar soil have had broader implications for mobility on Earth, particularly in environments with similar mechanical properties. Granular materials like dry sand, loose gravel or volcanic ash pose comparable challenges due to their dual solid-fluid behaviour, which makes predicting and controlling movement difficult. As robotic systems are increasingly deployed for the exploration and monitoring in unstructured terrains, adapting locomotion mechanisms to deal with the transitional nature of granular soils has become an important area of research. While these challenges were first encountered in the context of planetary exploration, they are equally relevant to a wide range of Earth-based applications. In such applications, reliable ground mobility is essential for ensuring operational safety and maintaining efficiency in difficult or unpredictable granular terrains.

1.1 Background

On Earth, desert environments, agricultural fields, and coastal regions represent key examples where robots must navigate loose and shifting substrates. Among these, coastal regions are especially significant, not only for their dynamic and often unstable terrain but also for their ecological and economic importance. Coastal regions are among the most dynamic and vital environments on Earth. They serve as critical interfaces between land and sea, hosting a wide range of ecosystems, supporting major economic activities, and providing habitat for billions of people. Over 40% of the world's population lives in coastal areas [3], and in the Netherlands, this percentage is even higher. With approximately 450 kilometers of coastline, the country has been deeply shaped by its coastal geography [4]. About 75% of the Dutch coastline consists of sandy environments such as beaches and dunes [5], while globally, approximately 31% of all coastlines are sandy [6].

The exploration and monitoring of these sandy coastal zones have gained importance in a variety of fields, including maintenance and inspection of coastal structures, environmental monitoring and search-and-rescue operations. These tasks are conducted in areas that are difficult or dangerous for humans to access, making autonomous robotic systems a valuable tool. However, for robots to operate effectively on their own, they must be able to move reliably across the sandy terrain. If a robot becomes immobilized in the sand, it often requires human intervention to recover it. Therefore, ensuring that robots can avoid getting immobilized is a critical factor in making autonomous operations practical and safe in these sandy environments.

Sandy terrains have complex mechanical behaviour that poses challenges for robotic locomotion. When sand is compressed, such as when a robot's foot or wheel rests on it, the grains lock together and resist deformation. The frictional forces between the grains create internal resistance, which is visible in Figure 1.2. In this state, the sand behaves like a solid, offering support and enabling traction. However, when a robot begins to move, the sand is disturbed and subjected to shear stress, causing the grains to lose contact and start flowing. As a result, frictional forces diminish, and deformation becomes dominated by collisional forces, which is shown in Figure 1.2. In this state, the sand behaves like a fluid, offering little resistance and allowing objects to sink into the sand [7], [8]. This dual nature makes it difficult for robots to gain traction or maintain stability, increasing the risk of slipping, sinking or getting stuck.

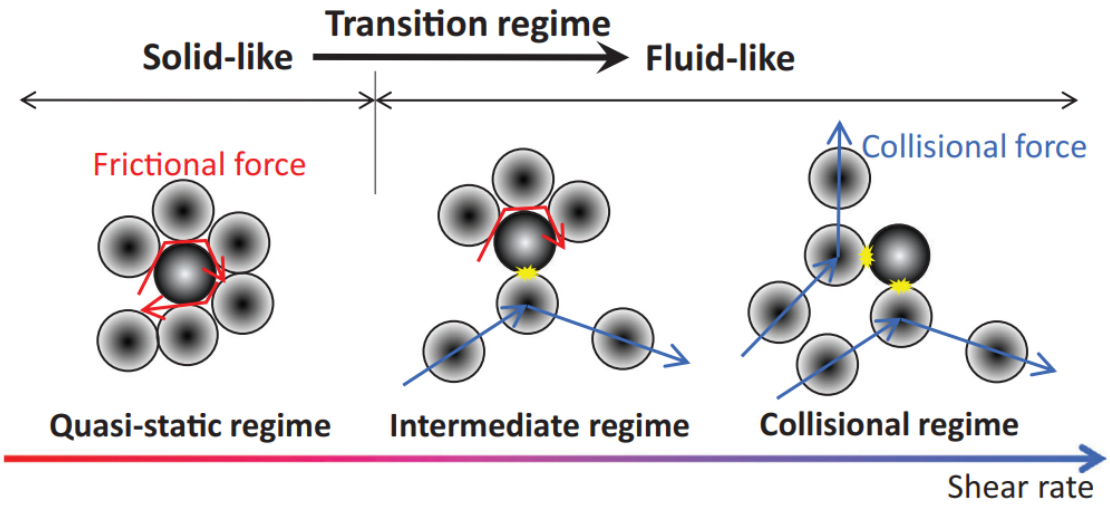

Figure 1.2: Schematic of solid- and fluid-like behaviour of granular material [8].

Traditional wheeled and legged robots often underperform in such conditions. Tires may sink, legs may slip, and rigid locomotion strategies generally fail to cope with the unpredictable response of sandy surfaces. The situation becomes even more complex when natural obstacles such as rocks, vegetation, and slopes are present (see Figure 1.3). For autonomous robots, these uncertainties can lead to mission failure, especially if the robot becomes immobilized in the sandy terrain.

Figure 1.3: Gently sloped sandy beach scattered with rocks, representing common terrain challenges for robotic locomotion [9].

1.2 Motivations

The unpredictable behaviour of sandy terrains requires robotic systems specifically designed to adapt to varying terrain conditions. The design of such systems is essential for successful operation of robotic systems in sandy environments. Combining the advantages of different locomotion strategies can create improved robotic systems, which can adapt to different terrains. An example of this is combining wheeled and legged locomotion into a wheel-leg system, which is already used for lunar rover designs (Figure 1.1). Wheel-leg systems combine wheeled locomotion with legged locomotion [1], [10], [11], where the wheel is attached at the end of the leg. Wheeled locomotion systems have also been combined with undulatory [12] or screw-based locomotion [13] to create improved wheels for locomotion on granular terrains. As a result, wave-like shaped wheels (Figure 1.4a) or screw-wheels (Figure 1.4b) have been developed. Various adaptable wheels are already developed, such as wheels with a variable diameter [14] or extendable lugs [15]. Figure 1.5a shows the design of [15], where the wheel can extend lugs to increase the traction on loose, granular soils. All those wheeled locomotion mechanism consists of rigid bodies only. Soft bodies have been used to develop robots capable of moving on sandy soils, but only for legged [16], snake-like [17] or vibration-based [18] locomotion systems. The soft, legged robot developed by [16] is shown in Figure 1.5b, where the soft legs are highly adaptable to different terrains.

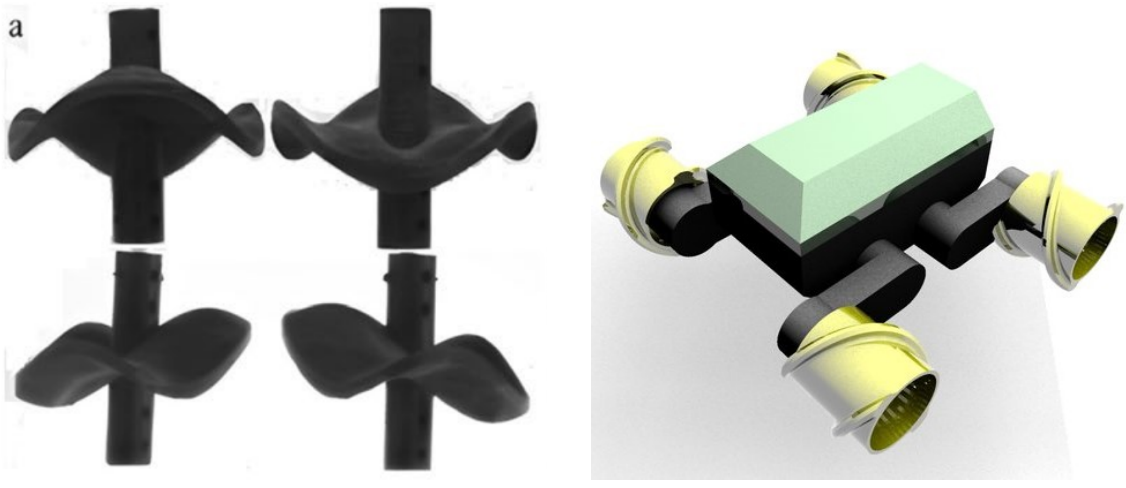

(a) Wheel with wave-like shape. Adapted from [12].

(b) Four-wheeled robot with screw-wheels [13].

Figure 1.4: Examples of wheel designs that combine different locomotion strategies.

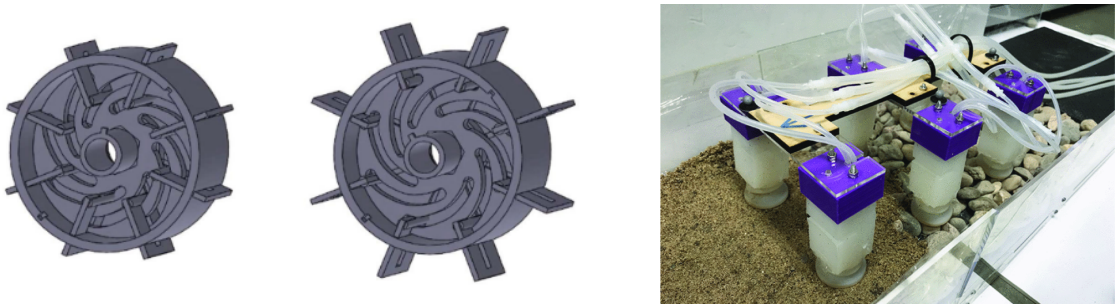

(a) Wheel with extendable lugs. Adapted from [15].

(b) Hexapedal robot with soft, pneumatic legs [16].

Figure 1.5: Examples of adaptable locomotion mechanisms.

Incorporating softness into the robot's design can enhance its ability to traverse obstacles and adapt to unstructured terrains. When combined with wheeled locomotion systems, this approach offers a promising balance between adaptability and efficiency. The added flexibility allows the robot to better tackle unstructured terrains, while the wheeled mechanism ensures effective movement across longer distances. To fully utilize these design advantages and optimize the robot's performance in sandy environments, accurate modelling of terrain-robot interaction is essential. Traditionally terramechanics-based models have been employed to predict how robots interact with deformable soil. Those terramechanics-based models are continuum-based models, which model the granular soil as a continuous medium and rely on empirical relations. The provided mathematical equations related to sinkage and traction require terrain-related parameters, which have to be obtained by performing experiments [19].

While these models provide valuable insights, they rely on empirical relations and simplifications that may not fully capture the complex, particle-based nature of sand. The use of discrete element method (DEM) simulations remains a relatively unexplored approach for evaluating robotic locomotion on sandy terrains. However, DEM models can be a valuable tool to evaluate robotic locomotion on granular terrains. DEM is a numerical modelling approach used to simulate the behaviour of granular materials. DEM represents the granular soil as a finite number of discrete particles, each governed by Newton's laws of motion. The interactions between particles, such as collisions, friction or bonding, are explicitly modelled using contact models. These contact models account for normal and tangential forces, damping and sometimes cohesion [20], [21]. The typical contact model used in DEM is shown in Figure 1.6. The particle-particle interactions are resolved using a spring-damping system in both normal and tangential direction. The normal and tangential component both includes a spring with stiffness K and a damper with damping D, which models how particles resist compression and dissipate energy during collisions. The tangential force computed from the spring damper system is limited by the Coulomb friction law, which is indicated with the slider in the bottom-left of Figure 1.6. The maximum resistive tangential force is determined by the value of the friction coefficient μ.

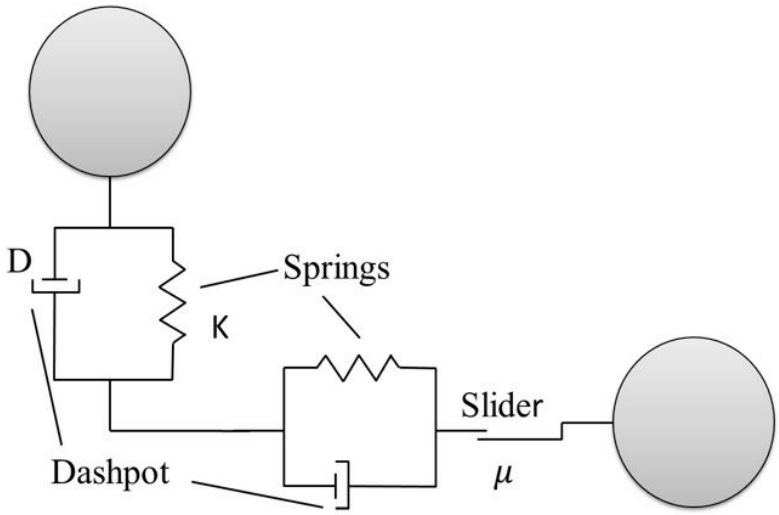

Figure 1.6: Schematic of the typical contact model used in DEM [22].

DEM tracks the motion of each particle over time, capturing the behaviour of the entire granular material. This particle-based modelling approach makes DEM especially suitable for studying how robotic wheels or legs interact with granular terrain. By focusing on local interactions at the particle level, DEM provides detailed insights into phenomena like sinkage and slippage, which are often oversimplified in traditional continuum-based models. Moreover, DEM allows for the exploration of how varying terrain properties such as moisture content can influence locomotion performance. The aim of this research is to use DEM simulations to support the design of a soft, wheeled locomotion system for sandy terrains. By using DEM as a tool to evaluate different designs, this study seeks to answer the following key question:

How can simulation-aided design be utilized to develop a soft, wheeled locomotion system for sandy terrains?

With the following subquestions:

1. What are the available strategies for robotic locomotion on granular terrains?
2. How can the interactions between soft robotic systems and sandy surfaces be modelled?
3. How can locomotion simulations be utilized to the design of a soft, wheeled locomotion system for sandy terrains?
4. How can the performance of a soft, wheeled locomotion system be evaluated?

1.3 Thesis Outline

This thesis is structured around the four subquestions. Chapter 2 gives an overview of the various locomotion mechanisms, the performance evaluation of these locomotion mechanisms and the different methods to model the interactions between robot and terrain. Chapter 3 discusses the design methodology of a robotic locomotion mechanism, including the use of simulations in the design process. The most suitable simulation framework is also identified and elaborated in this chapter. Chapter 4 presents various concept designs and their performance evaluation. In Chapter 5, the best performing concept is identified and further developed into a final prototype design, which is explained in Chapter 5. Chapter 6 is dedicated to evaluate the prototype performances using the developed simulation tools. All the major findings and possible future research are summarized in Chapter 7.

Chapter 2

Literature Review

Moving on granular surfaces is challenging due to the unevenness and fluidity of the granular surface. The difficulty of moving on granular surfaces has led to the development of multiple strategies aimed at overcoming this challenge. The different strategies to move on the granular surfaces are explained in Section 2.1, where the available solutions are categorized into six different groups. The soft, flexible, and adaptable robots in each class are given particular attention, as their enhanced capabilities make them especially interesting and worth exploring in greater detail. The performance of a certain locomotion method can be estimated by multiple key performance indicators (KPI), which have been identified from the literature in Section 2.2. Lastly, different modelling tools which can be used to model the interactions between robots and granular materials are presented in Section 2.3.

2.1 Locomotion Methods

This section classifies the variety of locomotion methods into six different classes. These locomotion methods will be explained in more detail in the following six sections.

2.1.1 Legged Locomotion

Legged locomotion involves the use of limbs to generate movement on granular surfaces. This method mimics biological movement, such as the movement of humans or animals. Legged locomotion can be further classified into four different subclasses.

Walking

Walking locomotion methods are highly effective to traverse various terrains. The flexibility of the legs allows the robots to adapt to uneven and shifting granular surfaces [23]. Bipedal walkers, with two feet, are human-like robots that have only two points of contact with the ground. As a result, achieving stability is quite a challenge. The research for bipedal walkers focuses mainly on different walking gaits [24], [25] (Figure 2.1a) or various feet designs [26]–[29]. The foot design of Zhang et al. [29] has an adaptive variable posture, which can change the shape of the foot to achieve better performance.

Quadrupedal walking can be executed by four-legged robots, which is a more animal-like locomotion method. Remy et al. [30] developed a four-legged robotic dog, but most research focuses on the foot design [23], [31]–[33]. All those designs are adaptable robotic foot structures, which can adapt to various environments. Liu et al. [16] developed a six-legged robot to perform hexapedal walking locomotion, which is shown in Figure 2.1b. This robot consists of soft pneumatic legs, which makes it highly adaptable to various environments.

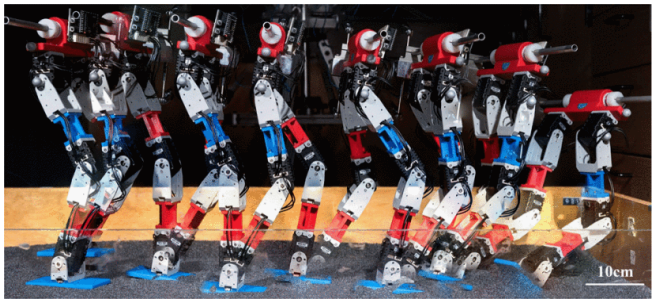

(a) Flat-footed, bipedal walking robot [24].

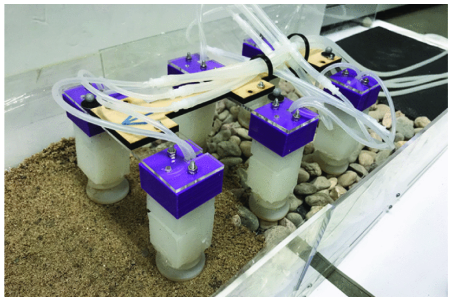

(b) SoRX hexapedal robot with soft, pneumatic legs [16].

Figure 2.1: Examples of walking locomotion mechanisms.

Rotary Walking

Rotary walking locomotion methods are using rotating legs to move on the granular surface. These designs are relatively simple to construct and can achieve high speeds on various granular surfaces [34], [35]. Most research in this category is about rotary walkers with semi-elliptical legs [34]–[43] (Figure 2.2a) or L-shaped legs [44]. The design of Zhang et al. [36] can change the shape of the leg from a straight fin to a bent C-shaped leg, as shown in Figure 2.2b. This makes the design suitable for amphibious locomotion in water and on granular surfaces. The rotary walking locomotion class also contains whegged locomotion, which is a combination of wheeled and legged locomotion. These so-called whegs are wheel-like structures with multiple spokes or legs that create a walking gait when the whegs are rotated [45]–[48] (Figure 2.2c).

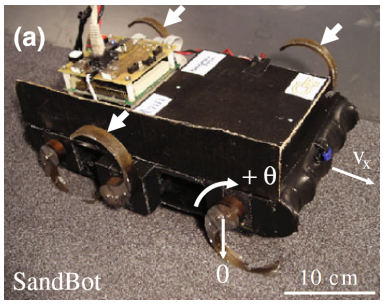

(a) SandBot rotary walker with six C-shaped legs. Adapted from [34].

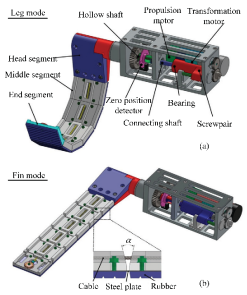

(b) Transformable fin-leg for amphibious rotary walker [36].

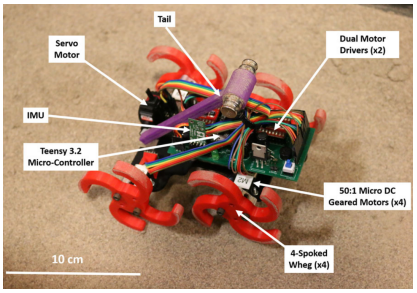

(c) Four-whegged robot with active tail and four-spoked whegs [46].

Figure 2.2: Examples of rotary walking locomotion mechanisms.

Crawling

Crawling locomotion differs from walking locomotion for two reasons. Firstly, the body of the robot remains closer to the ground and secondly the legs of the robot perform a push and pull movement instead of lifting and moving a leg. Therefore, it is more based on friction. The designs are mainly inspired by the movement of animals, such as a turtle-inspired robot [49], salamander-inspired robots [50], [51] (Figure 2.3a) and lizard-inspired robots [52], [53]. All these robots can move the legs vertically and rotate the legs in the horizontal plane to achieve locomotion. Both the salamander and lizard-inspired robots can also bent the body to achieve a crawling gait. Crawling locomotion systems can imitate the effective locomotion methods of desert animals, which can locomote efficiently on granular terrains.

Hopping

Instead of walking or crawling, robots can also hop across granular surfaces. Hopping locomotion mechanisms are not often studied. Roberts & Koditschek [54]–[56] have adapted a four-legged Minitaur hopping robot to make it suitable for locomotion on desert environments (Figure 2.3b). The Minitaur robot is lightweight and can hop very fast over granular surfaces. Buchner et al. [57] investigated the use of electrohydraulic artificial muscles as an energy efficient actuator for a hopping robot.

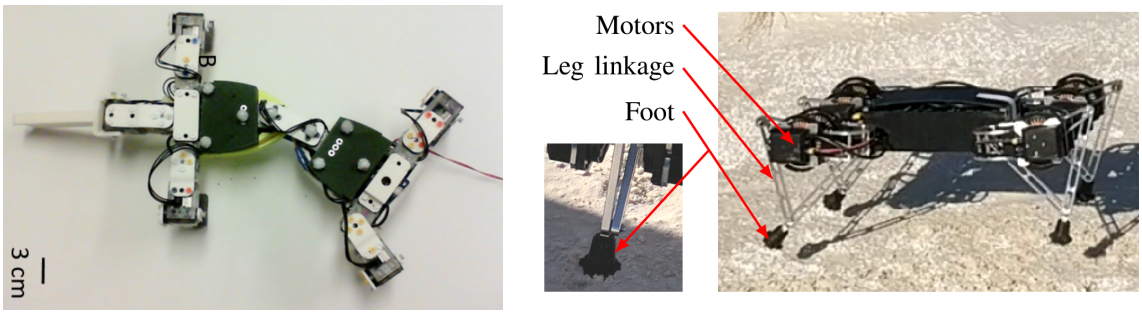

(a) Salamander-inspired crawling robot with four legs and body-bending ability. Adapted from [50].

(b) Minitaur hopping robot with four leg linkages. Adapted from [55].

Figure 2.3: Examples of crawling and hopping locomotion mechanisms.

2.1.2 Wheeled Locomotion

Another approach to traversing granular surfaces involves using wheels to roll over them. Wheeled robotics structures are simple and low-cost [11], [12], [58]. However, the ability to climb obstacles and the adaptation to different terrains are limiting factors for wheeled locomotion methods [11]. The designs of wheeled robots vary in the number of wheels, shape of the wheels and the size of the wheels. Most research is done into wheels which are equipped with lugs on its outer surface [1], [10], [11], [59]–[67]. These lugs will increase the traction when moving on granular surfaces. Multiple authors also researched wheels which can change its shape or stiffness to be able to move on various surfaces. Salazar Luces et al. [15] developed a shape-adapting lugged wheel (Figure 2.4a), where the lugs can be extended or retracted, depending on the soil type. Other authors developed wheels with a variable diameter [14], [68] (Figure 2.4b) or wheels which can transform into a wheg [69]–[73] (Figure 2.4c).

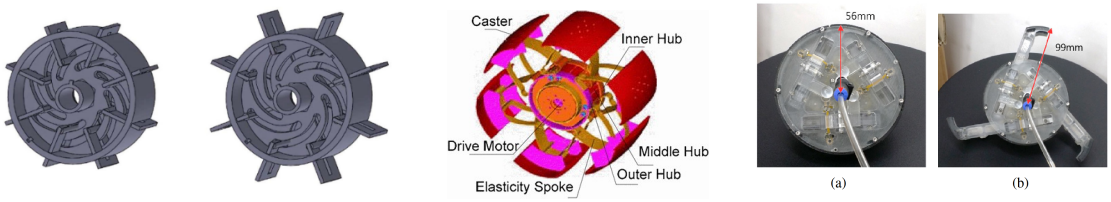

(a) Shape-adapting wheel with extendable lugs [15].

(b) Variable diameter walking wheel [14].

(c) Transformable wheel with extandable whegs [73]

Figure 2.4: Examples of shape-adapting wheel mechanisms.

Iizuka et al. [62] developed a flexible, metal wheel, which deforms when in contact with the surface. Yoon et al. [74] introduced a similar wheel design, incorporating stiffness-adjustment capabilities to enhance adaptability across different terrains (Figure 2.5a). Hojnik et al. [58] developed an adaptable robotic wheel where the centre hub of the wheel can be moved to traverse unstructured terrain (Figure 2.5b). Gkliva & Kruusmaa [75] developed a soft wheel, which can change its shape into a paddle (Figure 2.5c). A fully pressurized actuator creates a soft wheel for locomotion on granular terrains, where a partially deflated actuator creates a paddle for locomotion in aquatic environments.

Combinations of wheeled and other locomotion methods are also researched. Combining wheeled locomotion with legged locomotion creates the so-called wheel-legged robots, where the wheel of the robot is attached to a leg [1], [10], [11], [59] (Figure 2.6a). Other authors combined wheeled locomotion with a peristaltic motion, where the robot can vary its wheelbase [60], [76], [77]. Wheeled locomotion is also combined with undulatory locomotion by designing wheels with a wave-like surface shape to imitate the locomotion of sandfish, lizards and snakes [12], [78] (Figure 2.6b).

(a) Stiffness adjustable wheel mechanism [74].

(b) Three spoked wheel with movable centre hub [58].

(c) Soft transformable wheel [75].

Figure 2.5: Examples of adaptable wheel mechanisms.

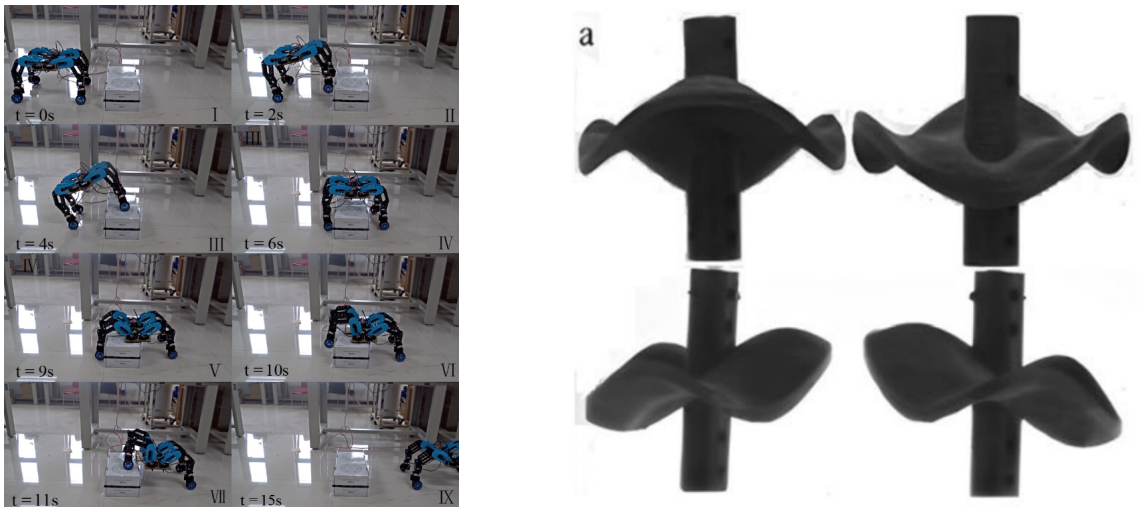

(a) Wheel-legged robot Guardian [11].

(b) Wheel with wave-like surface shape. Adapted from [12].

Figure 2.6: Examples of combinations of wheeled and other locomotion mechanisms.

2.1.3 Tracked Locomotion

Tracked locomotion utilizes continuous tracks to maximize the contact with the terrain. This increased contact area allows tracked locomotion systems to generate high traction. Additionally, distributing the robot's weight over a larger surfaces minimizes the sinkage [79]. Sutoh et al. [63] developed a tracked robot with lugs on its surface and investigated the influence of lug height and lug spacing (Figure 2.7a). Gomez et al. [80] developed a omnidirectional tracked locomotion system for mining environments. Nagatani et al. [79] combined legged and tracked locomotion by designing legs that are equipped with a tracked system (Figure 2.7b).

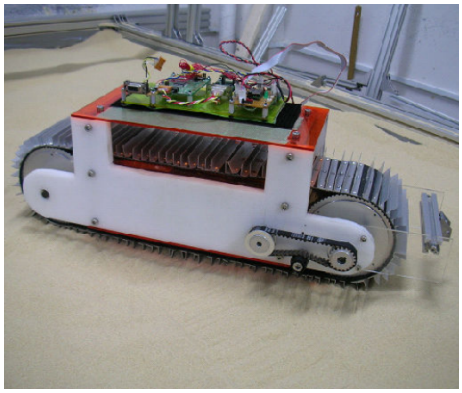

(a) Monotracked rover with lugs [63].

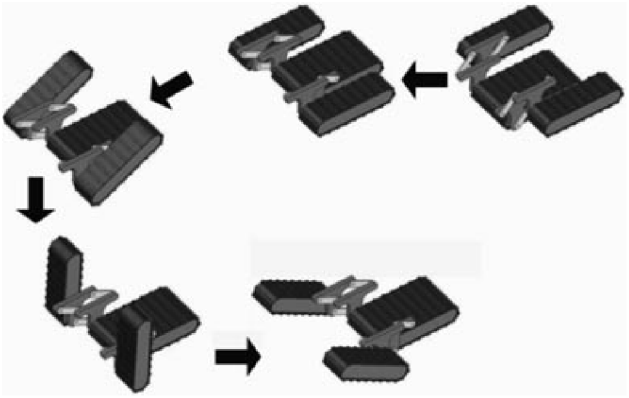

(b) Leg-track hybrid locomotion mechanism [79].

Figure 2.7: Examples of tracked locomotion mechanisms.

2.1.4 Screw-Based Locomotion

Screw-based locomotion is inspired by the Archimedean screw. The robot is propelled by rotation of a helical surface through the granular material. Screw-based locomotion methods are simple to construct [81] and can be operated in a wide range of environments [80], [82], but it is restricted to non-rigid surfaces only [13], [19]. Slippage is minimized as a result of the continuous contact of the screw with the terrain [80], resulting in an effective locomotion method. Mostly, two sets of screws are placed in parallel to translate the rotational motion into linear displacement [19], [80], [81], [83], [84] (Figure 2.8a). Lugo et al. [13] and Huang et al. [67] designed screw-propelled wheels (Figure 2.8b), which are wheels with a helical flange on the outer surface to increase traction. Marteau et al. [82] uses multiple screws in series to construct a screw-propelled, snake-like robot to move on granular materials (Figure 2.8c). For this locomotion method, only rigid bodies are used, as screw-based locomotion works on the principle of displacing the granular material, which can not be effectively done with soft robots.

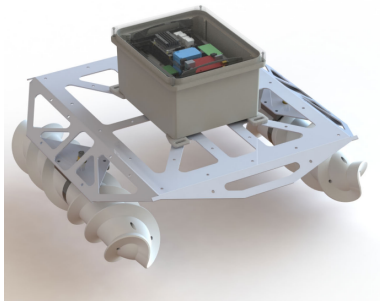

(a) Robot with parallel sets of Archimedean screw actuators. Adapted from [84].

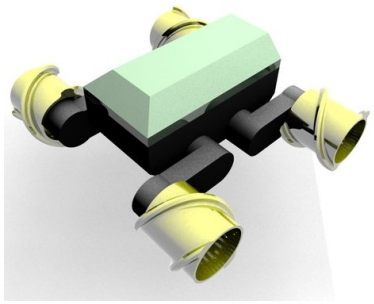

(b) Four-wheeled robot with screw-propelled wheels [13].

(c) Screw-propelled, snake-like robot. Adapted from [82].

Figure 2.8: Examples of screw-based locomotion mechanisms.

2.1.5 Undulatory Locomotion

Undulatory locomotion is inspired by the locomotion of snakes and is characterized by the travelling of waves along the body of the robot. These waves allow the robot to propel itself by interactions with the granular material. Generating enough traction can be difficult [17] but the key advantage is the ability of traversing a wide selection of terrains and complex environments [17], [85], [86]. Sidewinding is one of these bio-inspired undulatory locomotion techniques which is observed in snakes. Multiple authors developed snake-like robotic systems which can perform sidewinding gaits [86]–[88] (Figure 2.9a). Sidewinding of snakes generates waves in the horizontal plane and vertical plane to move and lift the body of the surface. Lateral undulation only generates horizontal waves and some authors developed snake-like robots using this undulatory locomotion principle [17], [85] (Figure 2.9b). Both of

these robots are soft robots, consisting of soft actuators to generate the travelling waves. Li et al. [17] also added scales on the outside of those soft actuators to generate anisotropic friction and improve the performance.

(a) Snake-like robot using sidewinding locomotion. Adapted from [86].

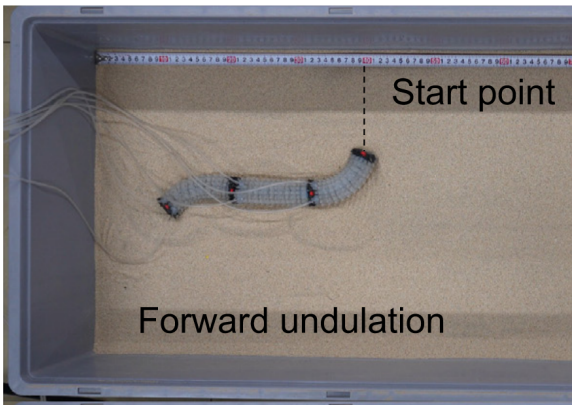

(b) Soft snake-like robot with three soft actuators. Adapted from [17]

Figure 2.9: Examples of undulatory locomotion mechanisms.

2.1.6 Vibration-Based Locomotion

Vibration-based locomotion uses vibrations that interact with the granular surface to generate forces to propel the robot. These locomotion mechanisms are simple and low-cost [18] and are therefore suitable for distributive exploration of challenging terrains with multiple robots [89]. Most vibration-based locomotion mechanisms use an out-of-balance mass [18], [89], [90]. Chen et al. [91] used a push-pull electromagnet to propel the Sand-skier robot (Figure 2.10a). The VibroBot developed by Kühnel et al. [18] (Figure 2.10b) can change its shape and stiffness, because of the soft inflatable body elements. Changing its stiffness will change the locomotion dynamics of the robot and changing its shape increase the ability to traverse obstacles.

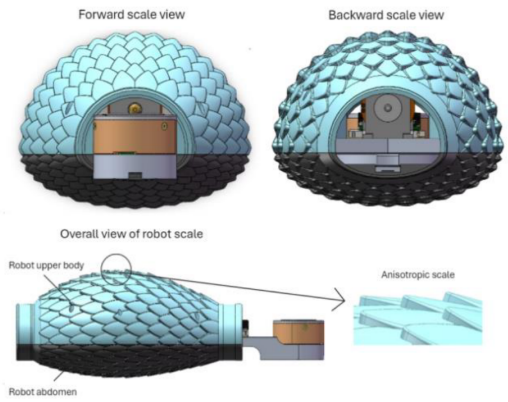

(a) Sand-skier robot propelled by a push-pull electromagnet [91].

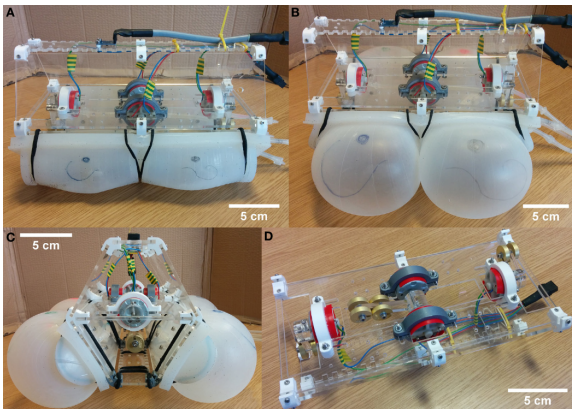

(b) Shape-adapting and variable stiffness robot with soft inflatable bodies (Vibrobot) [18].

Figure 2.10: Examples of vibration-based locomotion mechanisms.

2.2 Performance Indicators

The performance of locomotion mechanisms can be related to several fundamental principles of robotic motion and stability. Firstly, the manoeuvrability performance of robots is important, which is related to the linear and rotational movements of the robot. The most used KPI for linear movement is the speed of the robot [10], [12], [16]–[18], [31], [34], [36]–[40], [42], [44]–[48], [53], [67], [75], [84], [85], [88]–[90]. Performance in rotational movement is rarely quantified, although some studies report rotational displacement in degrees or radians [51]–[53].

The second principle is the sinkage of robotic systems into granular soils. Granular soils are soft and deformable, resulting in sinkage of the robot into the soil. Sinkage can be divided into two types [65], [76]. Static sinkage is generated by a vertical load when the robot is not moving. Dynamic sinkage is generated by a moving robot. Dynamic sinkage is greater than static sinkage due to changes in stress distribution and the flow of deformable soil below the robot. The first cause is shown in Figure 2.11a, where the extra sinkage generates sufficient normal stress to balance the vertical load. The second cause is shown in Figure 2.11b, where the granular material is dipslaced until a steady state is reached, providing sufficient support [19]. The most important KPI for measuring the sinkage is the sinkage depth, which is measured in metric units of distance [19], [20], [32], [33], [35], [36], [62], [83], [92].

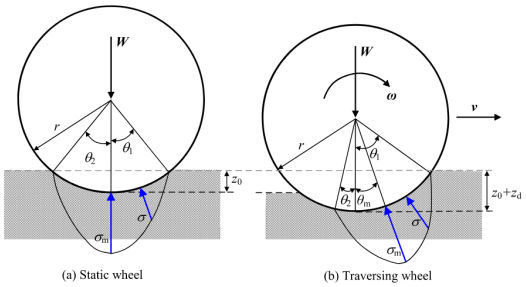

(a) Stress distribution and wheel sinkage for static and dynamic wheels [65].

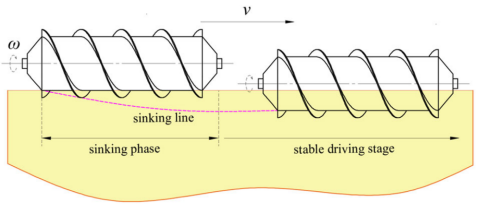

(b) Sinkage process of screw-propelled robot to a steady state [19].

Figure 2.11: Schematic of the sinkage of wheeled and screw-based locomotion methods.

The third fundamental principle of robotic motion and stability is the traction performance of the robot. Generating enough traction can be challenging due to the soft and deformable nature of granular materials. The three most widely used KPIs related to traction are the propulsive force, drawbar pull and slip ratio. The propulsive force, also referred to as traction force, is the available horizontal force to create forward motion (without considering resistive forces) and is usually measured in Newtons [11], [12], [20], [29], [33], [35], [36], [93]. The drawbar pull [13], [19], [61], [64], [65], [92], [94] is the effective horizontal force available for towing or pulling a load. The resistive forces are already taken into account, which makes the drawbar pull less than or equal to the traction force. Traction is closely related to the amount of slip. Slipping means a loss of traction at the contact point between the moving robot and the granular material. The degree of slip in the longitudinal direction can be estimated with the slip ratio [1], [12], [19], [23], [53], [63], [66], [75], [79], [83], [93]. The slip ratio is a relative measure used to indicate the degree of slip and, consequently, the level of traction. The slip ratio of wheels can be calculated with Equation (2.1) [19], [63], [66], [75], [83], [93], where s is the slip ratio, r the wheel radius, ω the angular velocity of the wheel and v_x the linear velocity of the robot.

$$s = \frac{r_w \cdot \omega_w - v_w}{r_w \cdot \omega_w} \tag{2.1}$$

The fourth principle is the energy consumption of the robot, which is important for the operational range of the robot. Energy consumption strongly depends on both the robot's configuration and the terrain type. The energy performance of the robot is quantified by directly measuring the energy consumption in joules [27], [28], [36], [56], [57] or by measuring the power consumption in watts [1], [20], [27], [37], [57], [95]. To compare the energy consumption of different locomotion methods, the cost of transport (COT) can be calculated [37], [46], [57], [75], [90]. The COT quantifies the amount

of energy used by a robot to move a certain distance, relative to the robot weight. The COT can be calculated with Equation (2.2) [57], [75], [90], where P is the power consumption, m_r is the mass of the robot, g is the gravitational constant and v_r is the robot's velocity.

$$COT = \frac{P}{m_r \cdot g \cdot v_r} \tag{2.2}$$

The fifth and last principle is the terrain adaptability of the robot. When moving across these terrains, robots often encounter slopes and small obstacles. The ability to explore inclined granular surfaces can be measured by the maximum slope angle, which is widely used as a KPI for locomotion on granular surfaces [1], [10], [11], [13], [16], [25], [31]–[33], [43], [53], [58]–[62], [66], [77], [79], [80], [82], [86], [90]. The ability to climb obstacles is often investigated by climbing a step size of a certain height, where the height is dependent on the type of robot [11], [16], [18], [32], [36], [43], [48], [59]. To compare climbing ability between different robots the step height can also be calculated as a percentage of the body height [18], [43], [48].

2.3 Modelling Tools

Modelling the interactions between robots and granular materials can enhance the ability to test different terrains and geometries, without the need of building a prototype. Several modelling tools are available to model those interactions. Terramechanics-based models have been employed to predict how robots interact with deformable soil. Those terramechanics-based models are continuum-based models, which model the granular soil as a continuous medium and rely on empirical relations. The provided mathematical equations related to sinkage and traction require terrain-related parameters, which have to be obtained by performing experiments [19].

Another tool is the resistive force theory (RFT), which is a simplified approach to calculate the resistive force based on interactions between local body segments and the granular material (Figure 2.12). The total resistive force of the body is then calculated by summing the resistive forces of the body segments [96]. Multiple studies have shown that RFT can be used to calculate the resistive forces for locomotion methods on granular surfaces [10], [24], [27], [28], [35], [36], [40], [42], [44], [51], [67], [88], [96]–[100]. These resistive forces can be used to simulate the speed or traction forces of robots locomoting on granular surfaces, using a multibody dynamics (MBD) simulation. RFT modelling can model the resistive force of complex geometries without the need of experiments with multiple geometries. Only simple experiments are needed to generate the force data for the small body segments. The method is computationally efficient. However, it relies on idealized terrain properties and does not account for terrain disturbances [96], [98].

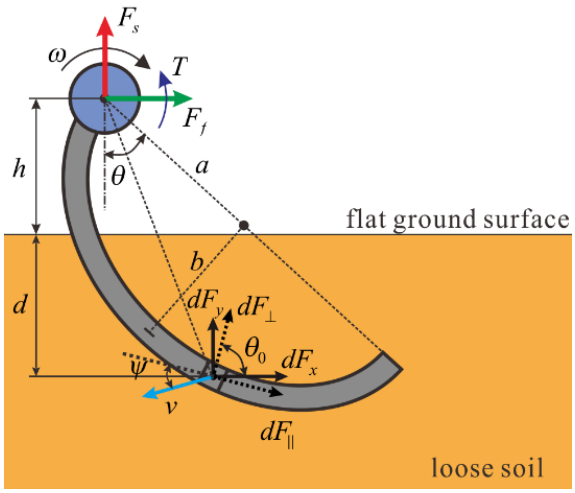

Figure 2.12: Schematic of 2D RFT model for semi-elliptical rotating legs. Adapted from [35].

A modelling tool capable of representing granular terrain more realistically is discrete element method (DEM) modelling. The granular material is modelled as a finite number of discrete particles, with a defined shape, size, position and velocity. A contact model is used to represent the particle-particle and particle-robot interactions, where various contact models can be chosen in the simulation software [20]. It is also possible to simulate heterogeneous granular materials with different particles [41]. DEM simulations are used to obtain the contact forces acting on the robot [20], [36], [38], [67], [82], [83], [97], the displacement of the robot [90], the sinkage of the robot [83] or the kinetic energy used by the robot [56].

DEM simulations can also be used in a co-simulation with other simulation tools. Zhu et al. [101] used a coupling of discrete element method (DEM) simulations with finite element method (FEM) simulations to evaluate the performance for a flexible metal wheel moving on lunar soils. At each timestep, the DEM part calculates the contact forces, which are transferred to the FEM part. The FEM part calculates the deformations and stresses and the updated geometry information is transferred back to the DEM part for the next timestep. This bi-directional coupling of DEM and FEM enables the possibility of simulating deformable bodies on deformable terrain.

Other authors used a coupling of discrete element method (DEM) simulations with multibody dynamics simulations (MBD) to create locomotion simulations with granular materials. MBD simulations can simulate the dynamic behaviour of a system, for example the movement of robots. The DEM part calculates the interactions of the robot with the particles, where the MBD part simulates the dynamic behaviour of each robot component as a result of the interaction forces. Again, this is a bi-directional coupling for each timestep. Co-simulating DEM and MBD can be done for rigid bodies [38], [67], [82], [83], [102]–[104], but also for flexible, deformable bodies [92], [105]–[108]. In that case DEM is coupled with multi-flexible-body dynamics (MFBD), where the DEM part is simulating the granular material and the MFBD part is another co-simulation of MBD and FEM. Using this simulation method allows for simulating movable, soft and flexible robots on deformable, granular soils. The biggest limitation for this method is the computational time, which makes it only possible to simulate those models with advanced computers.

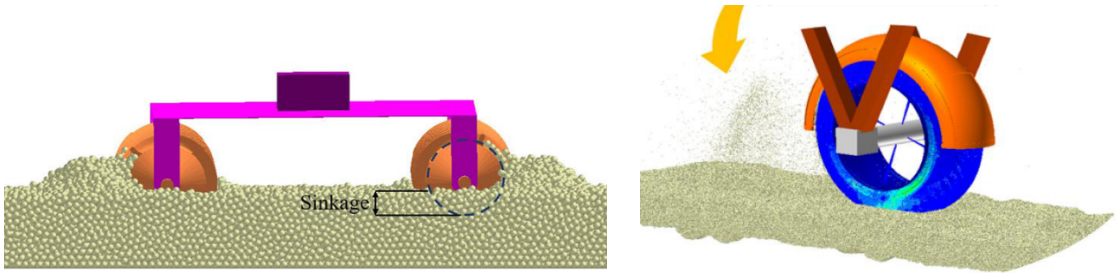

(a) Sinkage of a screw-driven robot in granular material. Adapted from [83].

(b) DEM-MFBD co-simulation of a wheel on granular soil. Adapted from [107].

Figure 2.13: Examples of DEM modelling for locomotion on granular soils.

The main challenges for locomotion on granular terrains are maintaining stability and generating sufficient traction. Solving these challenges can be realized through various locomotion strategies, each presenting distinct challenges. The most commonly used strategies are legged and wheeled locomotion methods, for which various robot designs exist. Improved locomotion methods can be developed if multiple locomotion strategies, each with its own advantages, are combined together. In addition, improvements can be made by developing adaptable, soft locomotion mechanisms that can adjust to various granular terrains and obstacles.

The performance of a certain locomotion mechanism can be evaluated using various KPIs, where KPIs related to manoeuvrability and traction are the most important to evaluate the travelling performance of a robot. Accurately modelling the interactions between robotic structures and granular terrains is also complex. Among the available tools, DEM simulations offer the most realistic approach to model the granular materials. Capturing the complex interactions between the robot and granular material involves integrating DEM with MBD simulations to simulate the behaviour of both the robot and the granular material.

Chapter 3

Methodology

The design problem identified in Chapter 1 will be solved by using simulation-aided design. A schematic overview of the design methodology is shown in Figure 3.1. The first step in this methodology is the concept design phase. Several concepts are developed to solve the design problem of the locomotion of soft, wheeled structures on sandy soils. The performance evaluation of each concept is done with locomotion simulations. For the concept evaluation, a co-simulation of DEM and MBD is used, which is explained in Section 3.1. More details about the different concepts and the performance evaluation are explained in Chapter 4. The best concept is chosen based on the simulation results of all concepts. If its performance does not meet expectations, new concepts may be developed. After selecting the best concept, several co-simulations are conducted to optimize the final prototype design, which will be explained in more detail in Chapter 5. These simulations help determine the optimal parameters for the wheel and overall prototype. If the resulting design does not meet the requirements, additional simulations may be performed for further optimization. If further improvements are not feasible, an alternative concept may be selected and optimized to fulfil the requirements.

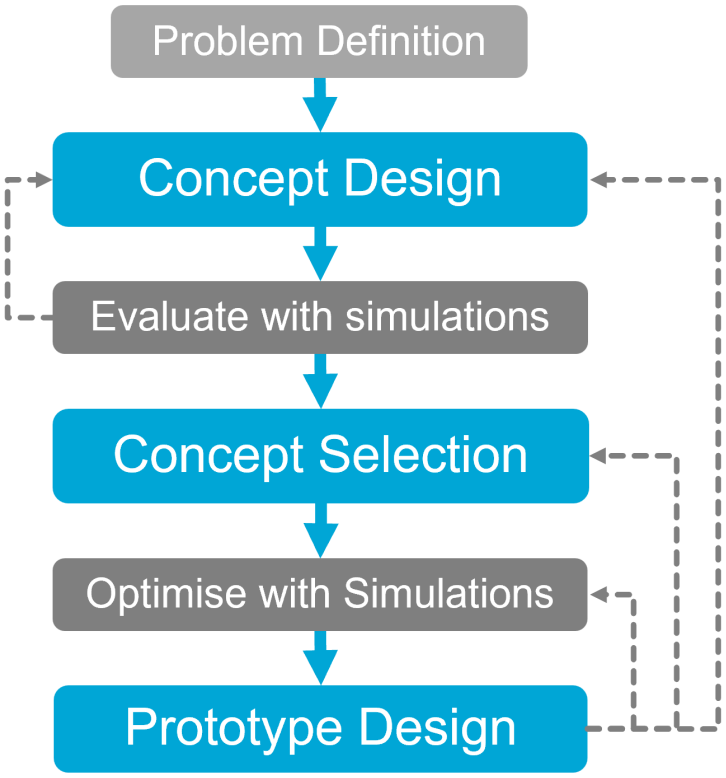

Figure 3.1: Schematic overview of the design methodology.

3.1 Simulation Framework

To simulate the locomotion of robots on granular soils, a coupled simulation method is used. Discrete element method (DEM) modelling will be combined with multibody dynamics (MBD) modelling. For this research, Altair EDEM is used for DEM simulations and Altair MotionView/MotionSolve is sued for MBD simulations, both version 2024.1.

The discrete element method (DEM) is a computational technique to model granular materials and their interactions with equipment, which is already explained in Chapter 1. The multibody dynamics (MBD) simulation predicts the robot's motion based on the interacting forces and system constraints. A multibody system refers to a collection of interconnected bodies. The bodies in the simulation can be rigid or flexible. An overview of the different bodies in the MBD simulation is shown in Figure 3.2. The MBD simulation consists of one rigid main body, 4 rigid wheel hubs and 4 flexbodies. Each body is subject to specific constraints and can experience significant translational and rotational motion. For the simulation setup shown in Figure 3.2 the rigid wheel hubs are constrained to the main body with four joints in the centre of the wheel. The flexbodies are also constrained to the rigid wheel hubs at the same joint. The motion is applied at each of the four joints, resulting in four-wheel-drive. In this simulation, a transient analysis is applied to determine how the system responds to loads and movements that change over time. The systems responses are displacements, velocities, accelerations and forces, which are calculated using the equations of motion [109].

In the co-simulation of DEM and MBD, MotionView will model the mechanical system interacting with the granular material, while EDEM will model the granular material. Both simulations will run in separate processes, but there is bi-directional communication between the DEM and MBD software. MotionView will provide the positions and velocities of the interacting bodies and EDEM returns the forces exerted by the granular material on the interacting bodies. This process is repeated at each point in time [110]. The motion simulation will be constructed with the MBD software. The granular material will be generated in the DEM software, which will be explained in Section 3.1.1.

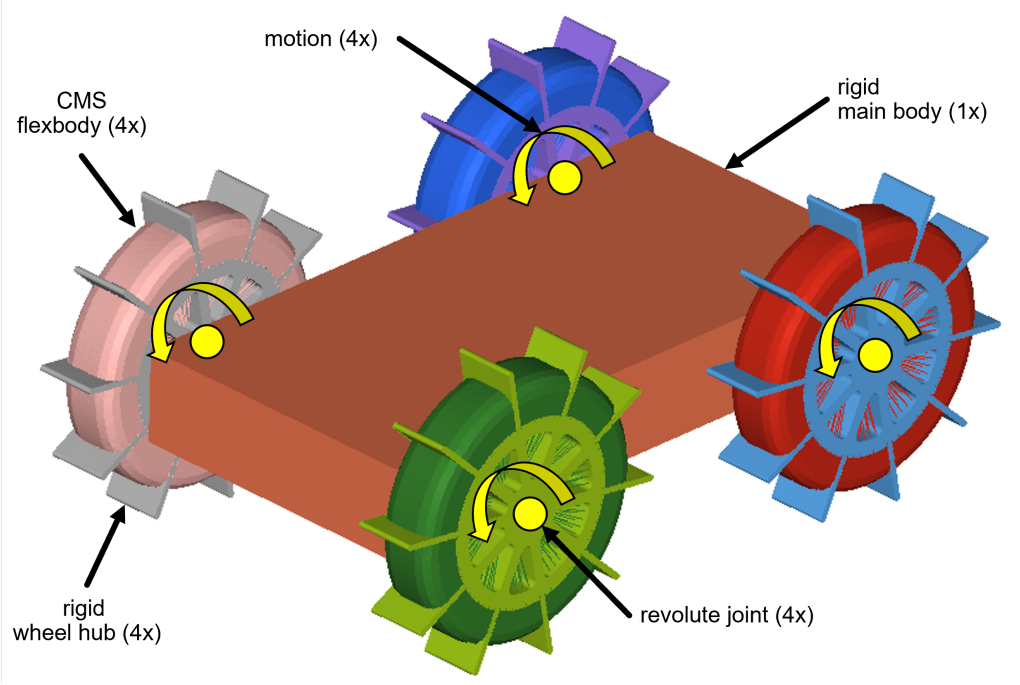

Figure 3.2: Simulation model for a simple, four-wheeled robot.

3.1.1 Granular Soils

One of the design goals is to move on various, granular, sandy soils. Therefore, three different sandy soils are selected, where each soil varies in moisture content. These granular soils are selected from the Soils Starter Pack of Altair EDEM [111]. This material database consists of eight different, soft soils, which can be used to compare equipment designs quickly and easily. The non-compressible dry soil is selected for representing dry sand, the non-compressible, sticky soil is selected for representing wet sand and

the compressible, sticky soil is selected to represent very wet sand or clay. The Poisson's ratio, density, shear modulus, coefficient of restitution, and the friction coefficients are the same, while the surface energy and plasticity ratio are different. The surface energy is a measure for the amount of moisture and therefore the stickiness of the soil. The contact plasticity ratio is measure for the compressibility of the soil and is only applicable for the Edinburgh-Elasto-Plastic-Adhesive (EEPA) contact model. Table 3.1 is showing the parameters of each granular soil. These parameters are obtained from [112]. Each soil also has an associated contact model, which is obtained from [111] and also listed in Table 3.1.

Table 3.1: Parameters of the three different sandy soils.

parameters	non-compressible dry sand	non-compressible, sticky, wet sand	compressible, sticky, very wet sand/clay
contact model	Hertz-Mindlin [113]	Hertz-Mindlin + JKR [114]	EEPA [115]
Poisson's ratio v	0.25	0.25	0.25
density ρ (kg/m^3)	2.6	2.6	2.6
shear modulus G (MPa)	10	10	10
co. of restitution e	0.55	0.55	0.55
co. of static friction μ_s	0.2	0.2	0.2
co. of rolling friction μ_r	0.1	0.1	0.1
surface energy γ_s (J/m^2)	-	3.75	50
contact plasticity ratio λ_p	-	-	0.7

In this research only spherical particles are used to model the sandy soils. Modelling the sand particle as a single sphere will be computationally efficient [116]. The size of the particles is upscaled to bigger particles, because modelling the sand particles with the initial size of 0.063-2.0 mm [117] would require too much computational time. Increasing the particle size by a factor of 1.5 doesn't influence the main behaviour of the granular material [118]. Some simulations have been performed to see the computational time for different particle sizes. The locomotion on dry sand of a small, four-wheeled robot with rigid wheels is simulated for 3 seconds. All parameters are kept constant, except the particle diameter. The simulations are performed by using an Intel® Core™ i7-8750H CPU with 12 cores and a clock speed of 2.20 GHz. The results of those simulations are shown in Table 3.2. Therefore, it can be seen that a particle size of 2 mm can be feasible, but already require 8 hours of computational time for one simulation, which will be increased further when flexible bodies will be used. Therefore, a particle size of 3 mm is chosen to be the best option for this research.

Table 3.2: Comparison of different particle diameters for non-compressible dry sand.

particle diameter (mm)	number of particles	time (h)
4	100000	0.59
3	200000	1.42
2	700000	8.36
1	6000000	100

The granular beds are created using the built-in volume packing tool of Altair EDEM. A certain volume is packed with a large number of particles based on a user-defined solid fraction. The solid fraction used in this research is 70%, which is a high solid fraction to create a well-packed granular bed [119]. The granular bed is generated in a separate simulation and then imported using the simulation deck export tool of Altair EDEM to reduce the computational time of the DEM-MBD co-simulations.

3.1.2 DEM Input Parameters

The DEM simulation first requires the input parameters for the granular material. These input parameters for the three different granular soils are already given in Section 3.1.1. Secondly, the input parameters for the equipment materials should be defined. Two equipment materials are defined for the simulations. The soft parts of the robot are made from silicone rubber. As the exact material is unknown and values for specific silicone materials are rarely available, the properties of standard silicone rubber are used [120], which are listed in Table 3.3. The other robot parts are 3D-printed and made of polylactic acid (PLA), which properties are obtained from [121] and also listed in Table 3.3. The interaction properties between the PLA robot parts and the granular soil are set to the default values of Altair EDEM (see Table 3.3), as these values are hard to find for the specific interactions between sandy soils and PLA. The interaction properties between the silicone soft parts of the robot and the granular soil are obtained from a study on tyre steering on sandy soils [92]. All these interaction parameters are listed in Table 3.3.

Table 3.3: DEM input parameters for the equipment materials and their interactions.

parameters	silicone rubber	polylactic acid (PLA)
Poisson's ratio v_g	0.47	0.36
density ρ_g (kg/m^3)	1100	1250
shear modulus G_g (MPa)	20	1287
co. of restitution e_g	0.48	0.5
co. of static friction μ_{sg}	0.55	0.5
co. of rolling friction μ_{rg}	0.37	0.01

The timestep of the DEM simulation should be set to a fixed value to ensure that the timestep of the DEM simulation is an exact multiple of the communication interval in MotionView. The fixed value of the timestep in the DEM simulation is set to a value such that the Rayleigh percentage is approximately 20% to ensure stable simulations. In certain cases, a smaller timestep is used to enhance stability, which will be specified later if applicable.

3.1.3 MBD Input Parameters

The motion simulation of the robot is constructed in Altair MotionView. The robot consists of a single main body with four wheels attached (Figure 3.2). The wheels consist of a rigid wheel hub with rigid lugs and flexible parts between the lugs of the wheel. The motion of the wheel is generated at the rotational joint between the wheel and the main body. The motion of the wheel can be generated by setting a certain angular velocity, angular acceleration or motor torque, depending on the goal of the simulation. The materials of the rigid body parts are set to PLA and for the soft and flexible parts to silicone rubber, with the parameters as given in Table 3.3. The chassis of the robot is modelled as a solid body, where it is in reality a shell body with a certain thickness. The extra weight of the solid body compensates for the weight of all the actuation and electronic parts. For the simulations with the obstacle, a contact is defined between the wheel bodies and the obstacle. The Poisson model is used to model the normal force of the contacts. The penalty of the normal force is set to a high value to reduce the penetration between the bodies and the coefficient of restitution is set to a low value to limit the bouncing (see Table 3.4). The static and dynamic friction coefficients between the equipment materials and the obstacle are set to the same values as in the DEM simulations (Table 3.3).

Table 3.4: MBD input parameters related to the contacts between the robot and the obstacle.

parameters	value
normal force penalty	500000
normal force co. of restitution	0.1

3.1.4 Modal Flexbody Representation

The soft parts of the robot will deform under the application of force. Therefore, the MBD simulation should be able to capture that deformation. A possible way to do this is by using a finite element model of the soft, flexible body. However, these finite element models have a very high number of degrees of freedom (DOF), which is hard to handle for the MBD solvers. Therefore, the flexible body is reduced to very few modal degrees of freedom. The displacement of a single element in physical coordinates is represented as a linear combination of a small number of modal coordinates. MotionView uses the component mode synthesis (CMS) technique to create a flexible body [122]. This technique reduces the degrees of freedom of the flexible body to a smaller set of modes. A mode is a specific way in which a structure naturally deforms or vibrates. The computational time for CMS flexible bodies is significantly lower than that of full FEM simulations due to the reduced number of DOFs. While FEM models may involve thousands or even millions of DOFs, a CMS flexible body uses only a limited number of selected modes, 15 in this case. As a result, simulations using CMS flexbodies can be 10 to 1000 times faster than full FEM simulations. However, CMS flexible bodies are only suitable for linear systems, so the deformations of the flexible body have to be small. This method is not ideal for simulating soft silicone parts, as these materials exhibit non-linear behaviour and undergo large deformations. CMS flexible bodies can be generated in MotionView using the built-in FlexPrep tool, which requires a FEM file as the input. The FEM file is shown in Figure 3.3a and the generated flexible body for use in MotionView is shown in Figure 3.3b. The flexible body is connected to the robot with the interface node in the centre, which is connected to all the flexible parts via rigid links.

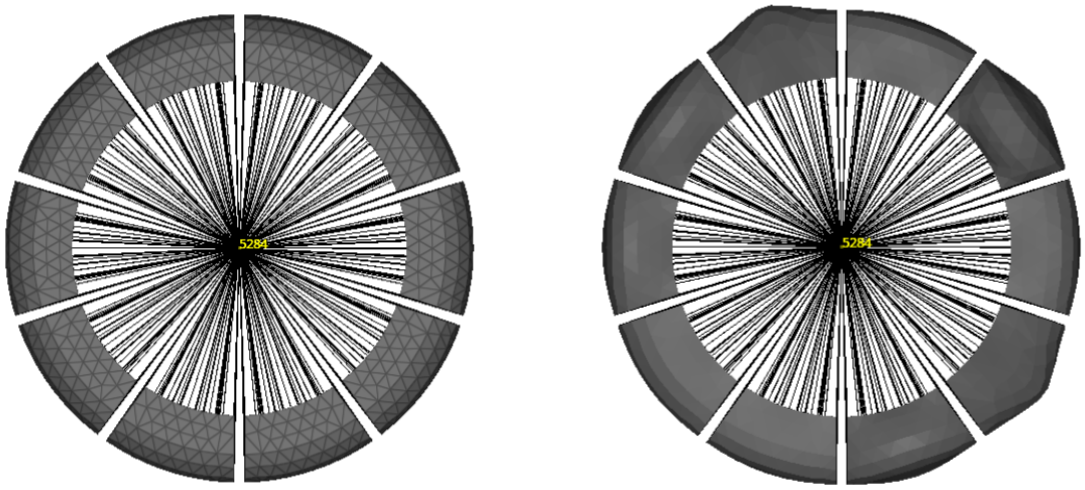

(a) FEM file of the flexible wheel parts.

(b) CMS flexbody for a certain deformation mode.

Figure 3.3: Generation of flexible bodies with the CMS technique.

3.1.5 Discretized Flexbody Representation

Performing a co-simulation of DEM and MBD with flexible bodies with non-linear behaviour and large deformations is difficult to achieve. Using a full nodal analysis is at the moment not possible in Altair MotionView and would also have been computational expensive. Therefore, a simplified approach is used to model the behaviour of the soft, flexible bodies in a more realistic way. These flexible bodies are discretized in multiple smaller bodies, which are connected with bushings to create a chain of bodies (Figure 3.4a). Each small body is also connected to the centre of the wheel with a linear spring-damper, which represents the stiffness of the flexible body (Figure 3.4b). This chain of small bodies can behave like a flexible body and it can undergo large deformations if the spring stiffness is low. In this case the chain of bodies consist of five different bodies. The number of bodies will determine the computational time of the simulation, as each extra body will also add an extra bushing and an extra spring-damper. For this research 5 bodies have been selected, as one simulation with the discretized flexbody representation is already around 15 hours. An odd number of bodies is chosen so that the highest point, where initial contact with the surface occurs, is located at the centre of a body rather than at a connection point. Various parameters must be defined for this type of simulation. Bushings require

translational and rotational stiffness values in all three directions, as well as corresponding translational and rotational damping values. Additionally, stiffness and damping coefficients have to be assigned for the spring-dampers. The exact values of the parameters and the way to obtain those is explained in Chapter 6, where the simulations with a discretized flexbody representation are explained.

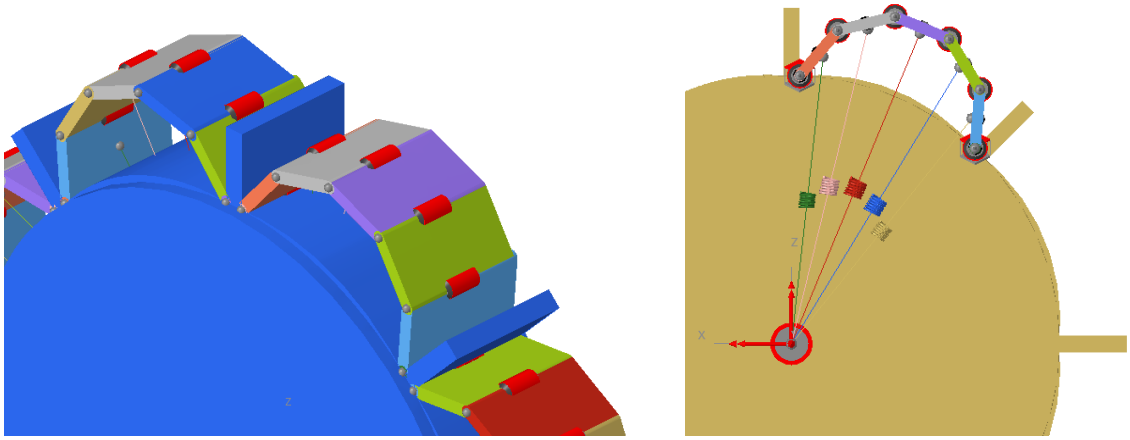

(a) Isometric view of the discretized flexbody representation.

(b) One section of the discretized flexbody representation.

Figure 3.4: Wheel with the discretized flexbody representation.

The main disadvantage of this discretized flexbody representation is the ability to model deformation only in 2 directions. It is not possible to model the deformation of the soft, flexible bodies in the direction parallel to the wheel axis. In reality, the soft, flexible bodies will also deform in that direction. An additional disadvantage occurs when using these discretized flexbodies in DEM simulations with small particles. Those particles can go between the rigid wheel and the chain of discrete bodies, which can result in unstable simulations or unrealistic behaviour. The complex construction of the simulation model is also a disadvantage of this method. Each body in the chain of discrete bodies must be imported individually into the simulation environment, and the bushings and spring-damper elements must be added and configured manually. As a result, any change in the design or the need to test a different configuration requires building an entirely new simulation model from scratch. This significantly reduces the adaptability of the simulation setup and increases the time required for model construction. Consequently, this type of simulation is not well-suited for exploring a wide range of design configurations efficiently.

3.2 Benchmark Simulations

A few benchmark simulations have been performed to investigate the influence of each part of the co-simulation and the influence of certain settings. The locomotion of a small, four-wheeled robot with rigid wheels is simulated for 3 seconds. The used granular material is the dry sand with a particle diameter of 4 mm. A list of the important simulation setting is given in Table 3.5. The computational times of those simulations are shown in Table 3.6. Those simulations are also performed by using an Intel® Core™ i7-8750H CPU with 12 cores and a clock speed of 2.20 GHz. Firstly this is done with a MBD simulation only. After that, the coupling with EDEM is made and the co-simulation of DEM and MBD is performed. The results show that the DEM part is the most computational expensive. Periodic boundaries (PB) are added on the sides of the granular bed to create a granular bed of infinite width. This means that particles leaving the boundary on one side are added back on the other side [123]. The results in Table 3.6 does show a small improvement in computational time when periodic boundaries are applied. A more significant improvement is found by using dynamic domains (DD). Adding a dynamic domain means only the particles around the robot are active. Outside the dynamic domain the particles are frozen, which reduces the computational time significantly [124]. Lastly, changing the bodies from rigid to flexible will increase the computational time, as can be seen in Table 3.6.

Table 3.5: Overview of the key simulation parameters used for the benchmark simulations

simulation parameter	setting
granular material	dry sand
particle diameter	4 mm
granular bed dimensions	1000x400 mm
granular bed thickness	50 mm
robot dimensions	240x150 mm
wheel diameter	100 mm
wheel thickness	20 mm
wheel angular acceleration	3 rad/s^2
simulation duration	3 s

Table 3.6: Computational times of benchmark simulations to investigate the influence of different simulation settings.

simulation type (4 mm particles)	time (h)
MBD only	0.0025
MBD + DEM	1.2
MBD + DEM + PB	1.12
MBD + DEM + DD	0.42
MBD + flexbody	0.025
MBD + DEM + PB + DD + flexbody	0.59

Interactions between soft robotic structures and sandy soils can be simulated by using a locomotion simulation which combines MBD and DEM simulation techniques. Two different types of simulation will be used in this research. The first type is a locomotion simulation with CMS flexbodies, which will be used for evaluating the concept designs and for optimizing the design of the selected concept. The advantage of this simulations is the low computational time. The second simulation is a locomotion simulation of the final prototype design with the discretized flexbody representation. This simulation type is computationally expensive and therefore only used to evaluate the performance of the final prototype design. The final prototype's performance is evaluated on three types of sandy soils with different moisture levels: dry sand, wet sand, and very wet sand or clay.

Chapter 4

Concept Design

The challenge of locomotion on granular soils can be addressed through various approaches, as outlined in Chapter 2. This thesis specifically focuses on the design of wheel-like locomotion mechanisms. This also includes the whegged locomotion mechanisms, which is the combination of a wheel and a wheg, as explained in Section 2.1.1. Seven different concepts have been developed, each incorporating soft and flexible parts to enhance adaptability to various granular terrains.

The selection of the best concept is explained in Section 4.8 and is based on the performance of each concept. The performance is evaluated using motion simulations on granular soil. A co-simulation of DEM and MBD is used to evaluate the performance of each concept, as described in Section 3.1. The flexible bodies are represented by a modal representation, as explained in Section 3.1.4. The dry sand granular material (see Section 3.1.1) is selected as the granular material, because the locomotion will be the most challenging on the dry sand, due to its softness. The dimensions of the granular bed are set to 1000 mm long and 400 mm wide. The thickness of the granular bed is set to 50 mm. The robot is modelled as a simple main structure with four wheel-like structures. The total length and width of the robot are 240 mm and 150 mm respectively. Each wheel-like concept has a wheel diameter of 100 mm and a thickness of 20 mm. Each concept is evaluated by simulating the locomotion of the robot during 3 seconds, where each wheel is accelerated with 3 rad/s^2. The important simulation settings are also summarized in Table 4.1. The performance of this simulation is evaluated with one KPI, which is the total distance travelled by the robot. This distance is a measure for the amount of traction generated.

Table 4.1: Overview of the key simulation parameters used for analysing different concept designs.

simulation parameter	setting
granular material	dry sand
particle diameter	3 mm
granular bed dimensions	1000x400 mm
granular bed thickness	50 mm
robot dimensions	240x150 mm
wheel diameter	100 mm
wheel thickness	20 mm
wheel angular acceleration	3 rad/s^2
simulation duration	3 s

The seven concepts are presented in the following seven subsections (Sections 4.1 to 4.7). The concept designs are presented with schematic drawings of the different configurations. In all drawings, rigid bodies are indicated in black and flexible, soft bodies are indicated in blue. The simulation results of each concept are presented by some figures, showing the robot on the simulated sandy soil. In these figures, rigid bodies are indicated in grey, where flexible, soft bodies are coloured with a contour plot, showing the deformation of the flexible, soft bodies. The corresponding values of the contour plot are shown in the legend on the left side of each figure. The values, provided in meters, are all very small, typically less than a millimeter, due to the simulation method being limited to small deformations.

4.1 Concept 1

The first concept is a combination of a rigid and soft lugged wheel (Figure 4.1a). Four lugs of the wheel are rigid, where the other four lugs are soft and flexible. The rigid wheel hub is connected to four soft and flexible parts. Those parts can deform around obstacles to increase the grip on the obstacle. The performance of this concept is evaluated by a motion simulation on dry sand (Figure 4.1b). The total distance travelled is 536 mm.

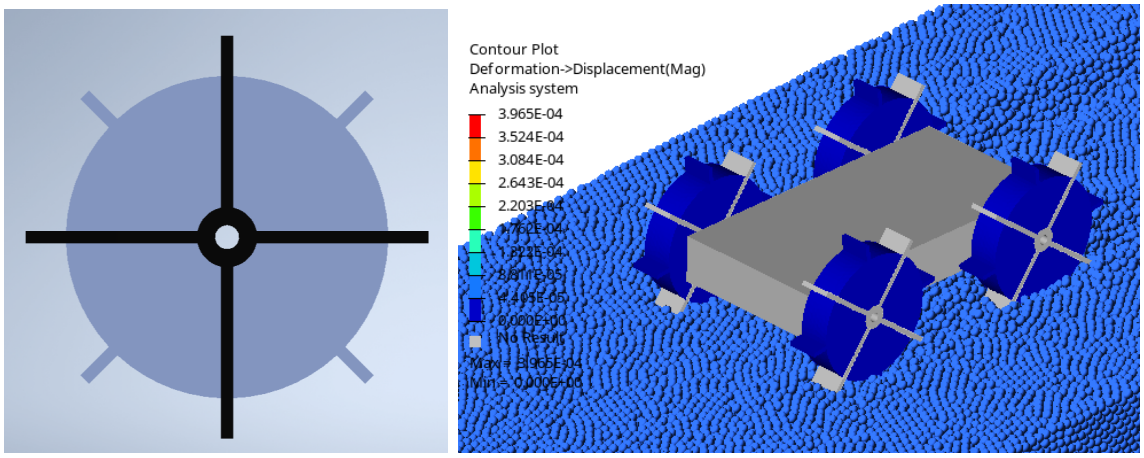

(a) Wheel design of concept 1. (b) Simulation of concept 1.

Figure 4.1: Wheel design and simulation results for concept 1.

4.2 Concept 2

The second concept is a wheel with a star shape when it is deflated (Figure 4.2a). The rigid wheel hub is connected to four soft, flexible parts, which have a concave shape. In this configuration, the wheel has four spikes which can increase traction on loose granular soils. If the soft parts are inflated, a circular, convex shape is created (Figure 4.2b). This configuration creates a larger contact surface with the soil and is therefore more suitable for more rigid soils. The flexibility of the soft parts of the wheel allows easy adaptation to obstacles in the terrain. The performance of both configurations is evaluated with simulations (Figures 4.3a and 4.3b). The total distance travelled is 475 mm for the deflated star-shaped wheels and 455 mm for the inflated circular-shaped wheels.

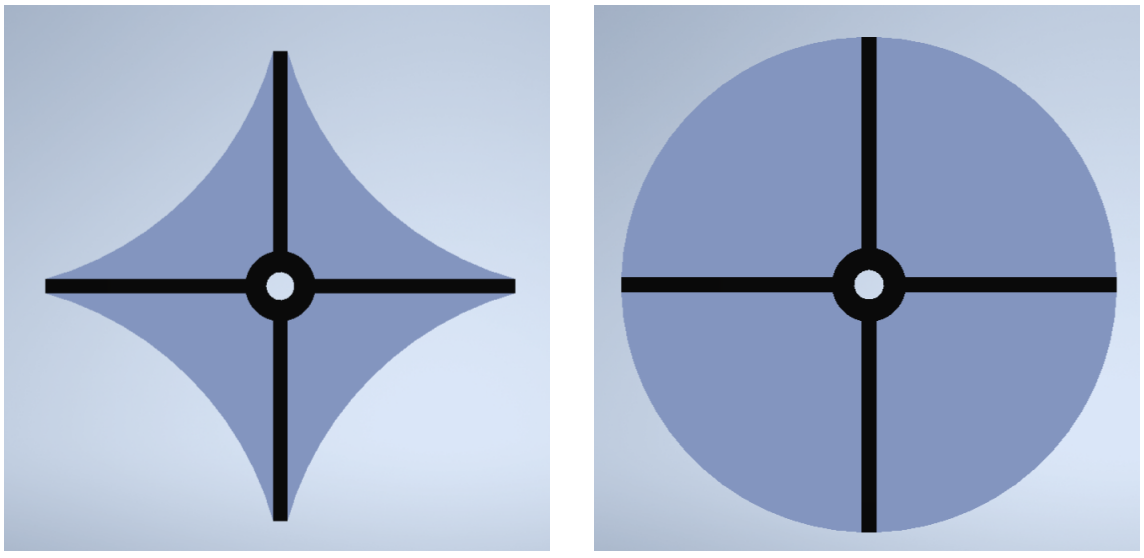

(a) deflated configuration (b) inflated configuration

Figure 4.2: Two different configurations of the wheel design of concept 2.

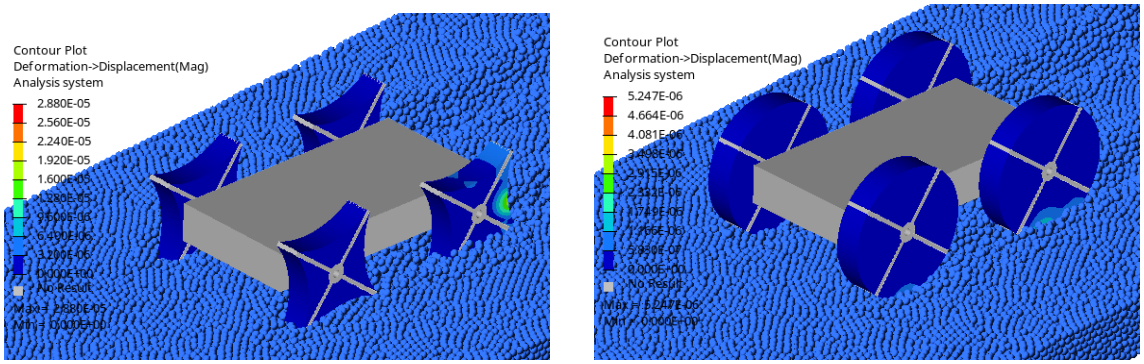

(a) deflated configuration (b) inflated configuration

Figure 4.3: Simulation results for both configurations of concept 2.

4.3 Concept 3

The third concept is a soft wheel with a rigid inner wheel hub (Figure 4.4a). The soft wheel has inflatable chambers on the outside of the wheel, which can be inflated to create lugs (Figure 4.4b). These lugs can improve the traction performance of the wheel in loose granular soils. For more rigid soils, the circular wheel can generate more traction due to a larger contact surface. The performance of the wheel is evaluated for the wheel with lugs, for the inflated configuration (Figure 4.5). The performance for the deflated configuration is not evaluated, as this is just similar to the circular wheel of concept 2 (Section 4.2). The total distance travelled for the wheel with lugs (inflated configuration) is 590 mm.

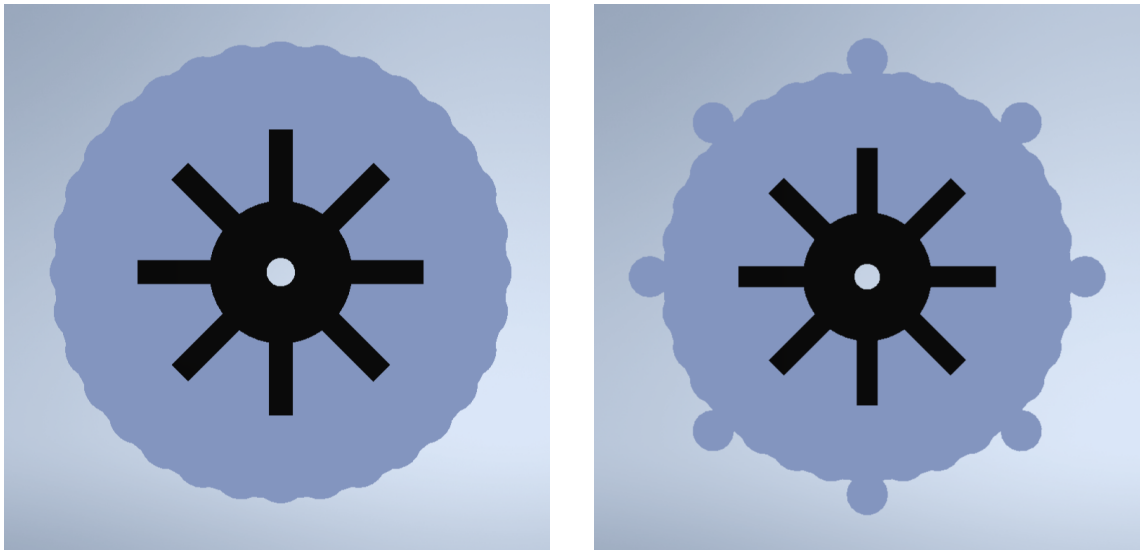

(a) deflated configuration (b) inflated configuration

Figure 4.4: Two different configurations of the wheel design of concept 3.

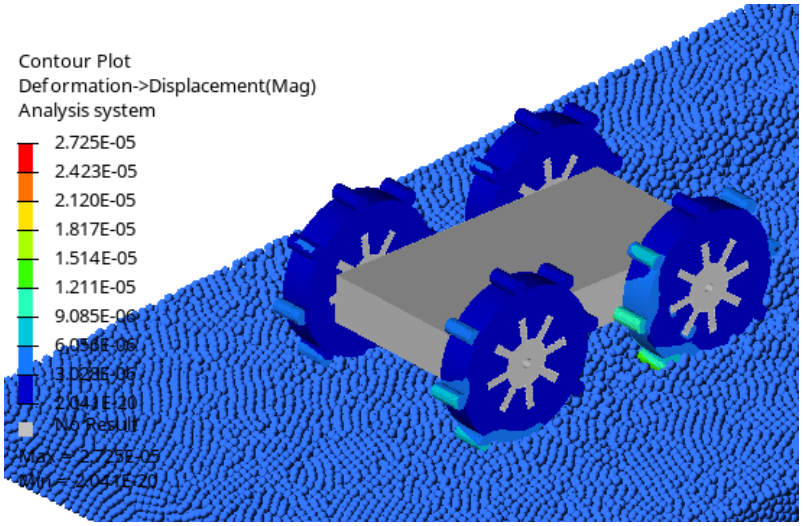

Figure 4.5: Simulation results for the inflated configuration of concept 3.

4.4 Concept 4

The fourth concept is a lugged wheel with flexible, shape-shifting bodies between the lugs. Those flexible bodies can be inflated or deflated to change the shape and stiffness. In the deflated configuration (Figure 4.6a), a lugged wheel is created, which can generate a lot of traction in soft, granular surfaces. For the inflated configuration (Figure 4.6b) the lugged wheel is changed into a more circular wheel, which can generate more traction on rigid surfaces or more sticky granular surfaces. Another advantage of the flexible, inflatable parts is the ability to climb certain obstacles. Those flexible parts can generate more grip on obstacles due to the ability to deform around the obstacle. The inflated version of the wheel increases the contact area with the obstacle or soil, which increases the traction performance. The performance of both wheel configurations is evaluated by simulations (Figures 4.7a and 4.7b). The total distance travelled is 527 mm for the deflated wheel and 559 mm for the inflated wheel.

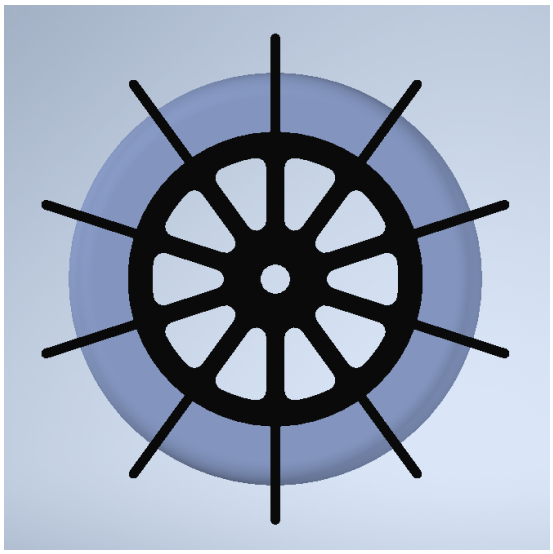

(a) deflated configuration

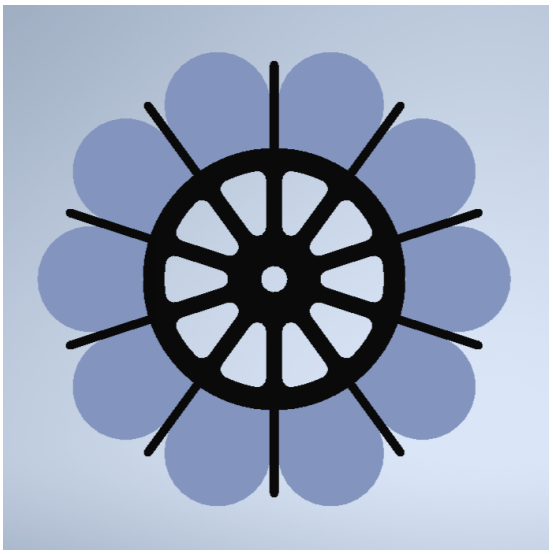

(b) inflated configuration

Figure 4.6: Two different configurations of the wheel design of concept 4.

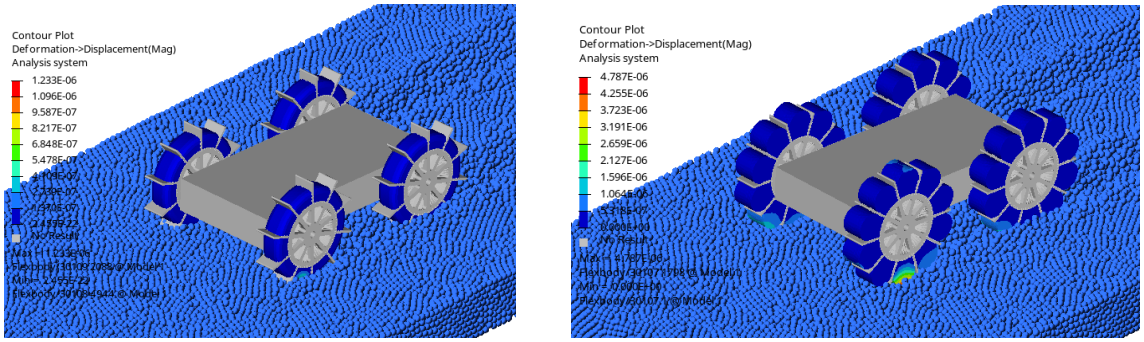

(a) deflated configuration (b) inflated configuration

Figure 4.7: Simulation results for both configurations of concept 4.

4.5 Concept 5

Concept 5 is a shape-shifting design which can change from a wheel to a wheg. In the deflated configuration it forms a soft, circular wheel (Figure 4.8a). The soft parts of the wheel can be inflated, which will increase the radius of those parts. As a results, soft parts of the wheel will stick out to create a so-called wheg (Figure 4.8b). This wheg will increase the traction performance of the design, especially in loose granular soils. The performance of those whegs is evaluated with a simulation (Figure 4.9), where the total distance travelled is 638 mm. The performance of the deflated configuration of the design is not evaluated by simulations, as this wheel design is almost similar to the circular wheel of concept 2, where the performance is evaluated in Section 4.2.

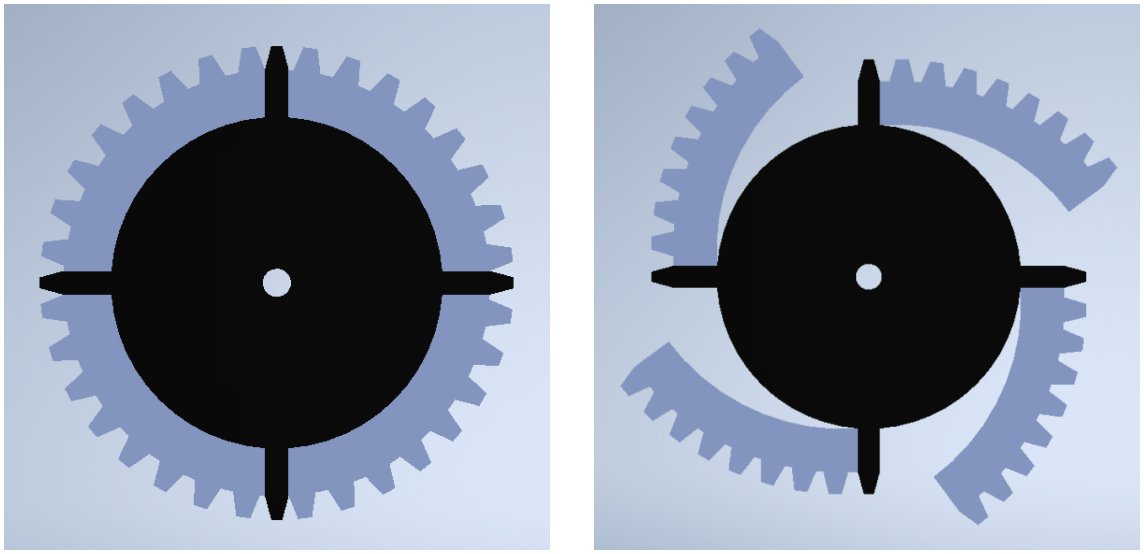

(a) deflated configuration (wheel) (b) inflated configuration (wheg)

Figure 4.8: Two different configurations of the wheel design of concept 5.

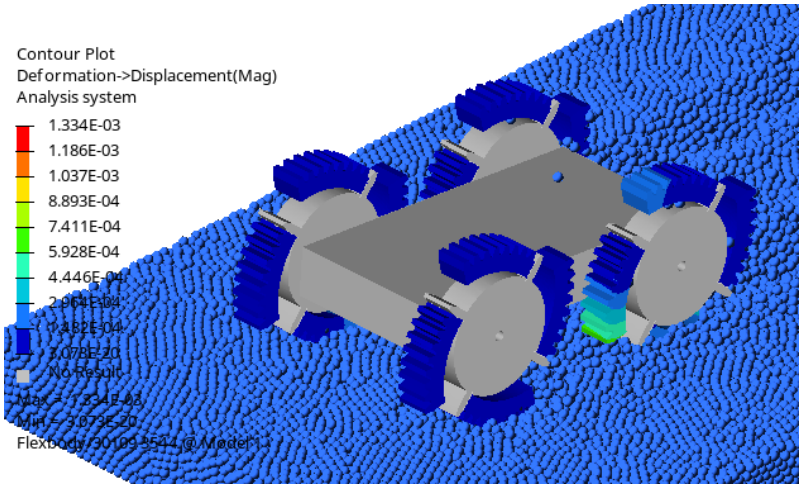

Figure 4.9: Simulation results for the inflated (wheg) configuration of concept 5.

4.6 Concept 6

Concept 6 is the design of a wheg with four legs. In the deflated configuration the legs are straight, creating a plus symbol (Figure 4.10a). Inflating the legs will create curved legs (Figure 4.10b). The shape-shifting mechanism of this concept can be used to adapt the robot to different terrains or obstacles. The performance of both configurations is evaluated with simulations (Figures 4.11a and 4.11b). The total distances travelled for the deflated, straight wheg and for the inflated, bent wheg are 432 mm and 579 mm respectively.

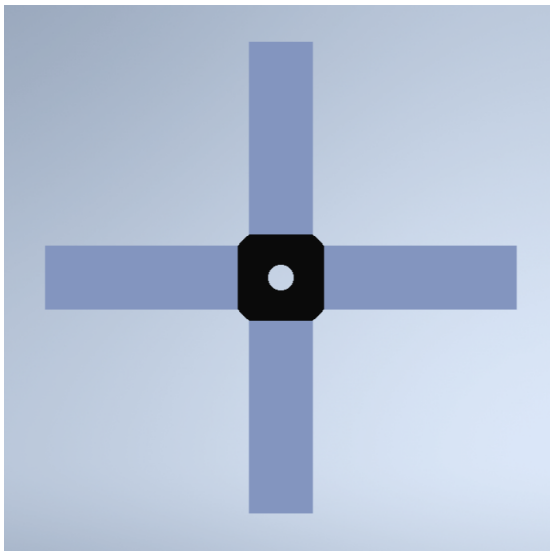

(a) deflated configuration

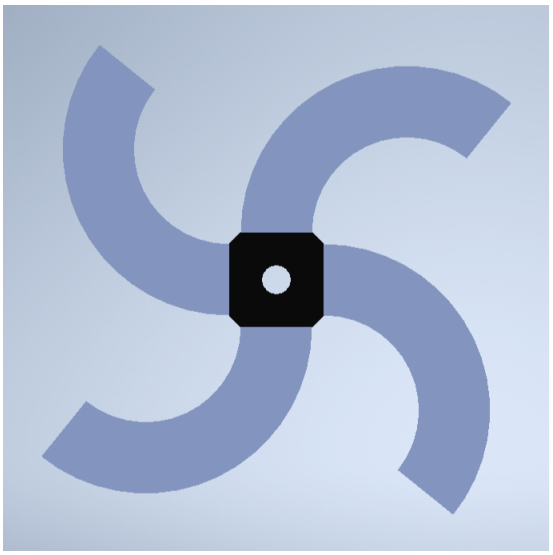

(b) inflated configuration

Figure 4.10: Two different configurations of the wheg design of concept 6.

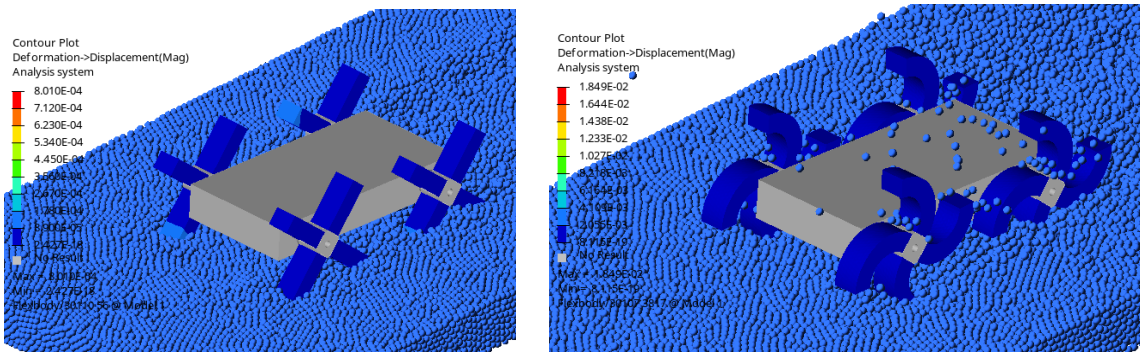

(a) deflated configuration (b) inflated configuration

Figure 4.11: Simulation results for both configurations of concept 6.

4.7 Concept 7

The seventh and last concept is again a wheg design. For this concept, a rigid, curved wheg is designed. Soft bodies are placed between the whegs (Figures 4.12a and 4.12b). Those soft bodies can increase the adaptability of the robot, especially in exploring unstructured terrain with different obstacles. The stiffness and shape-shifting capabilities of the soft bodies enhance the ability to traverse a wider range of obstacles. The performance of the two variants is also evaluated with simulations (Figures 4.13a and 4.13b). The total distance travelled is 440 mm for the deflated configuration and 473 mm for the inflated configuration.

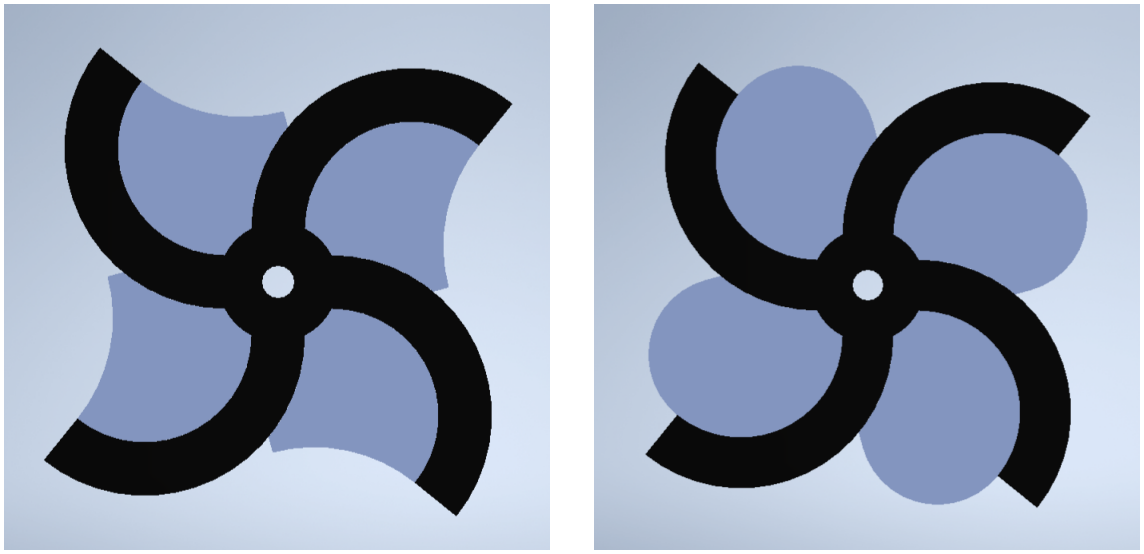

(a) deflated configuration (b) inflated configuration

Figure 4.12: Two different configurations of the wheel design of concept 7.

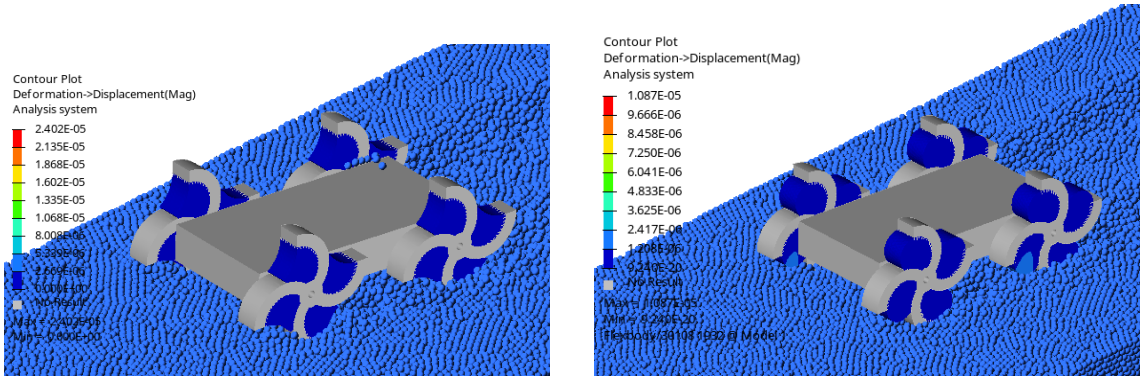

(a) deflated configuration (b) inflated configuration

Figure 4.13: Simulation results for both configurations of concept 7.

4.8 Concept Selection

The selection of the best concept is based on several aspects. Firstly, performance evaluation from simulations is used to compare the different concepts, with travelled distances listed in Table 4.2. However, simulation results alone are not sufficient. Adaptability to different terrains or obstacles and fabrication feasibility are also considered. Some concepts require very strong materials, which would reduce the softness of the soft bodies and thus diminish their added value. Additionally, the selected concept must be practical to fabricate.

Table 4.2: Total distances travelled for all configurations of each concept.

concept	distance deflated (mm)	distance inflated (mm)
concept 1	536	-
concept 2	475	455
concept 3	590	-
concept 4	527	559
concept 5	638	-
concept 6	432	579
concept 7	440	473

The results in Table 4.2 show that concept 1, concept 3, concept 4, concept 5 and the inflated configuration of concept 6 have the best travelling performances. The total distance travelled is way lower for concept 2, concept 7 and the deflated state of concept 6. The adaptability to different terrains and obstacles is high for concept 3, concept 4 and concept 5. The adaptability of concept 1 is low, because this is just a soft wheel with four rigid lugs. The adaptability of concept 2 and concept 6 is high, but the travelling performance of the deflated configuration is very low compared to the other concepts. Therefore, concept 3, concept 4 and concept 5 can be considered as the best performing and the best adaptable concepts.

When looking into the feasibility, concept 4 would be the most feasible to construct. Constructing concept 3 would require the design of different chambers in the soft body to enable the inflation of lugs on the outside of the wheel. The principle of concept 4 is almost similar to concept 3, but constructing concept 4 would be much easier. The feasibility of concept 5 would also be questionable. The material of the soft bodies needs to be very strong, as it should be able to withstand all the forces on the soft legs. Next to this, the granular material will go in-between the rigid wheel hub and the soft bodies, which will have a negative effect on the performance. Therefore, the selected concept will be concept 4. This concept has a high travelling performance combined with adaptability to different terrains and obstacles due to its shape-shifting ability. The structure is simple and can be easily fabricated. The detailed design of this concept will be explained in the next chapter.

Chapter 5

Prototype Design

The previous chapter has explained the developed concept and the selection of the best concept. In this chapter, the selected concept will be further detailed and the design of the prototype will be explained. The prototype design can be separated in two different parts. The first part (Section 5.1) is about the wheel design of the robot, which is the most important part of the prototype design. The second part (Section 5.2) is the design of the robot chassis, which contains the electronics and motors to power the robot.

5.1 Wheel Design

The selected concept, concept 4 (Section 4.4), is a lugged wheel design with shape-shifting ability. The shape-shifting of the wheel is achieved by using soft, inflatable elements. The concept design of the wheel is shown in Figure 5.1a. There are 5 parameters of the wheel which can be varied to create the optimal wheel design for locomotion on sandy soils. Firstly, those 5 parameters will be explained and the influence on the performance will be discussed (Sections 5.1.1 to 5.1.5). Then a final, optimized wheel design is proposed and the fabrication method is explained (Section 5.1.6). Lastly, the design and fabrication of the soft, inflatable elements will be explained in more detail in Section 5.1.7.

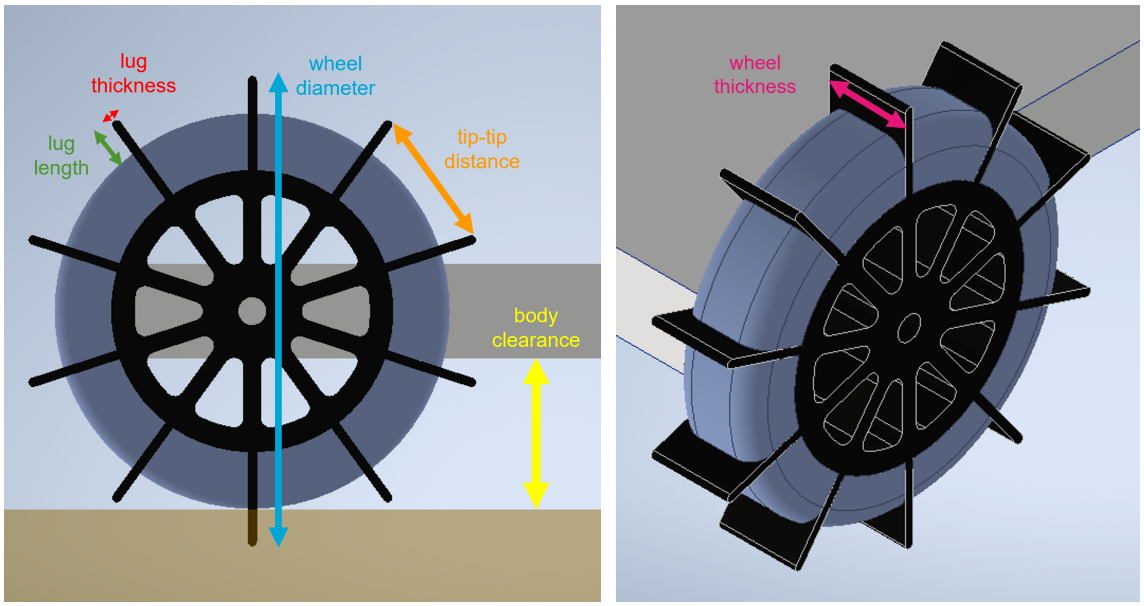

(a) side view (b) iso view

Figure 5.1: Schematic of the wheel parameters and the robot's body clearance for the selected concept design.

5.1.1 Wheel Diameter

The wheel diameter is indicated with the blue arrow in Figure 5.1a and includes also the lugs. For the concept wheel this value is set to an arbitrary value of 100 mm. One important aspect to take into account is the body clearance of the robot with the granular soil [66]. The body clearance is indicated with the yellow arrow in Figure 5.1a. A minimum wheel diameter is required to maintain sufficient body clearance and prevent the robot from becoming stuck on an obstacle or from dragging its body on the ground. For the wheel design of the prototype the wheel diameter is set to a value of 120 mm. This higher value is required to create enough body clearance between the robot and the granular soil. The height of the robot chassis, which is explained in more detail in Section 5.2, is increased, because of the size of the components. As a result, the wheel diameter is increased to create sufficient clearance with the granular soil.

5.1.2 Wheel Thickness

The wheel thickness is indicated with the pink arrow in Figure 5.1b. The wheel thickness corresponds to the width of the wheel in the lateral direction, perpendicular to the direction of travel. The wheel thickness affects stability and the contact area with the ground. Thicker wheels provide a larger contact area with the ground, resulting in increased friction and improved stability. However, thicker wheels also increase the total weight of the robot and therefore influence the performance, especially on slopes. For steep slopes, thinner wheels have better performance due to their lower weight. On small slopes, thicker wheels have better performance, as they can generate more traction [66]. For the prototype wheel design the thickness of the wheel is set to 20 mm, which is equal to the wheel thickness of the concept design. This value is based on the overall dimensions of the prototype and the weight of the wheel. The wheel thickness of 20 mm should be wide enough to generate enough support and it is also feasible for the fabrication of the soft, inflatable elements.

5.1.3 Lug Length

The length of the lugs is indicated with the green arrow in Figure 5.1a. It is the distance from the top of the lug to the top of the soft body in deflated configuration. Increasing the lug length increases the travelling performance of the robot [63], [66]. However, the lug length is also determined by the design of the inflatable elements. When inflated, these elements should protrude beyond the wheel's surface, meaning the lug length must be less than or equal to the maximum extension achieved through inflation. The soft, inflatable elements will be made of silicone rubber, which can be easily stretched to more than 200%. The selected lug length for the optimized wheel design is set to 12 mm. Figure 5.2b shows the soft element in inflated configuration for a lug length of 12 mm. Increasing the lug length results in deformation of the soft element due to contact with the lug. The goal of this design is to prove the working principle of the shape-shifting wheels. Therefore, the lug length is set to a conservative value to make sure the soft elements can be inflated without obstruction.

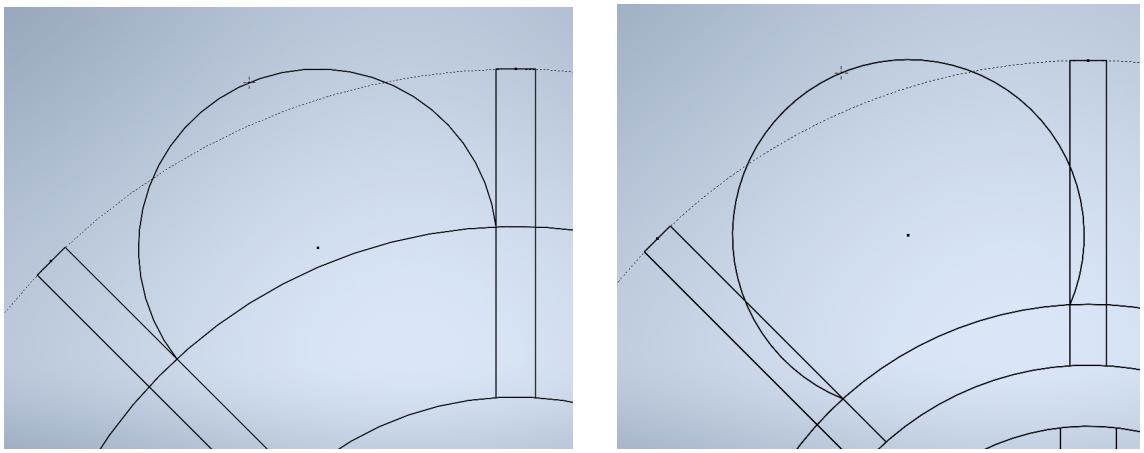

(a) lug length of 12 mm (b) lug length of 20 mm

Figure 5.2: Schematic of the inflation of the soft elements for two different lug lengths.

5.1.4 Lug Thickness

The influence of the lug thickness on the wheel performance is not investigated in literature. Increasing the lug thickness decreases the tip-tip distance. So, the thickness of the lugs could have an influence on the wheel performance. To investigate this, a few motion simulations have been performed. Four different lug thicknesses have been investigated with simulations: 2 mm, 5 mm, 10 mm and 15 mm thick lugs. The simulation models for the 2 mm and the 15 mm lugs are shown in Figures 5.3a and 5.3b. The robot design is similar to the concept design. The simulation is used to investigate the influence of the thickness of the rigid lugs, which is not influenced by the design of the soft elements. Therefore, the wheels are modelled as rigid bodies to reduce the computational time. The total weight of the robot is set to approximately 2 kg, where the weight of the wheels is equal for all configurations. For the wheels with thicker lugs, the density is decreased to have the same weight. The dry sand granular material is used for these simulations, as the lugs are the most beneficial on loose soils. The robot design and the granular bed are similar to the concept simulations. The important simulation parameters are listed in Table 5.1. Detailed information about the simulation framework is described in Section 3.1. The performance of each configuration is evaluated with one single KPI, which is the total distance travelled. The results of those simulations are listed in Table 5.2. The results show that the travelling performance decreases when the lug thickness increases. Therefore, the optimal lug thickness is as small as possible, which depends on the structural strength of the lug. For the optimized wheel design, the lug thickness is set to 3 mm, to ensure the structural integrity of the lugs.

Table 5.1: Overview of the important simulation parameters used for analysing different lug thicknesses.

simulation parameter	setting
granular material	dry sand
particle diameter	3 mm
granular bed dimensions	1000x400 mm
granular bed thickness	50 mm
robot dimensions	240x150 mm
robot weight	$\approx$ 2 kg
wheel diameter	100 mm
wheel thickness	20 mm
lug length	15 mm
lug thickness	2-15 mm
number of lugs	8 lugs
wheel angular velocity	5 rad/s
simulation duration	3 s

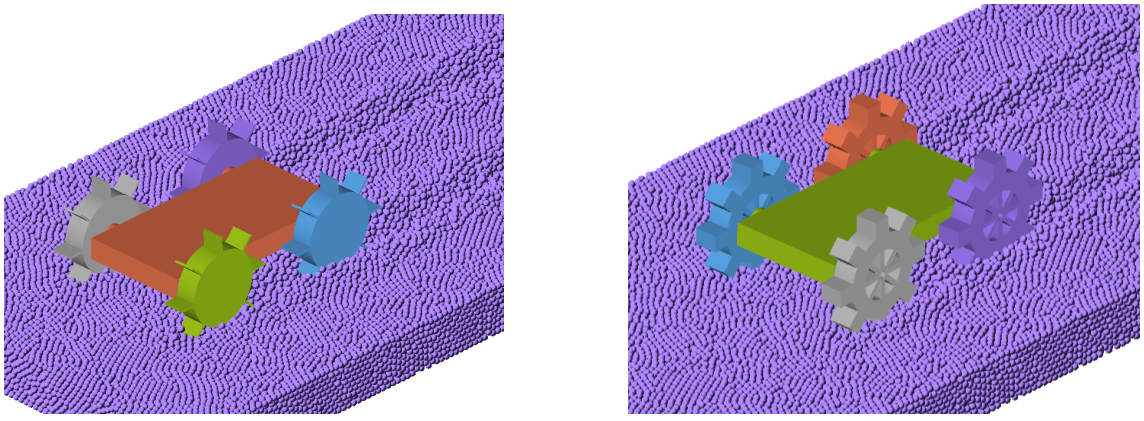

(a) lug thickness of 2 mm

(b) lug thickness of 15 mm

Figure 5.3: Motion simulations of robot with two different lug thicknesses.

Table 5.2: Total distances travelled for wheels with four different lug thicknesses.

lug thickness (mm)	distance travelled (mm)
2	620
5	610
10	580
15	540

5.1.5 Lug Spacing

The lug spacing has significant influence on the performance of the wheel. The lug spacing can be indicated with different measures, namely the tip-tip distance, angle between two lugs or the number of lugs on the whole wheel. The tip-tip distance is the distance from the tip of one lug to the other lug, which is indicated with the orange arrow in Figure 5.1a. The lug spacing has influence on the traction, but also on the ability to traverse obstacles. In general, the smaller the lug spacing, the better the generated traction [63]. However, the tip-tip distance should be smaller than or equal to the rupture distance, which is dependent on the lug length and the granular material [63]. The soil in front of the lug is pushed, which creates a destructive phase in the soil (Figure 5.4). The rupture distance is the horizontal distance of the destructive phase of soil and is dependent on the internal friction angle ϕ of the soil. The rupture distance can then be calculated with Equation (5.1) [63], where l_s is the rupture distance of soil, l_l is the lug length and ϕ is the internal friction angle. The lug length for the optimized wheel is 12 mm and the internal friction angle of dry sand is 28.9 degrees [125].

$$l_s = \frac{l_l}{\tan(45° - \phi/2)} \tag{5.1}$$

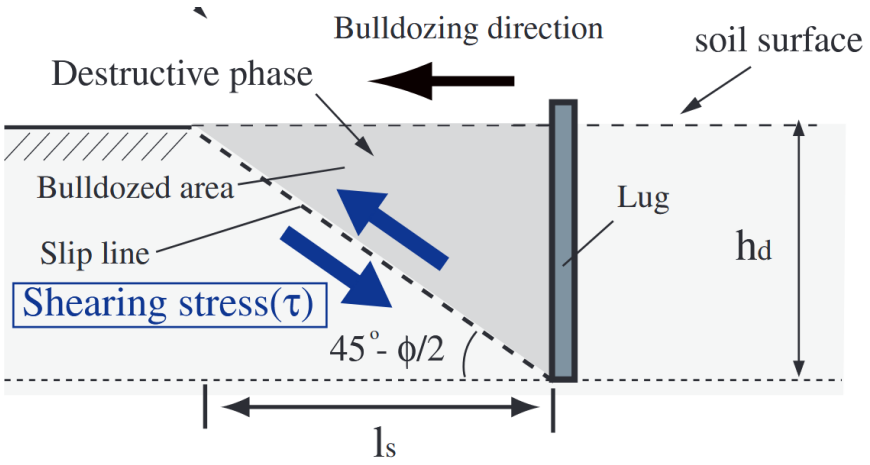

Figure 5.4: Schematic of the soil rupture distance for a lugged wheel. Adapted from [63].

The calculated soil rupture distance for the optimized wheel design is 20 mm. This would require a tip-tip distance smaller than or equal to 20 mm to achieve optimal performance. However, the tip-tip distance should also be large enough to be able to construct the soft, inflatable elements. A larger tip-tip distance is also beneficial for the traversing of obstacles, as the robot can climb larger obstacles when the tip-tip distances is larger. The grip on obstacles is way better when touching with the soft, inflatable elements instead of touching the obstacle with the rigid lug. To investigate the optimal lug spacing for both soil and obstacles, a few simulations of different lug spacings have been performed. Three different configurations have been tested, which details are listed in Table 5.4. The important simulation settings for the lug spacing simulations are listed in Table 5.3. The robot motion is simulated for 4 seconds, which is long enough to travel to the end of the granular bed with obstacles. The used granular material is the dry sand material. Some obstacles are added to evaluate the influence of the lug spacing on the obstacle climbing performance. These obstacles are modelled as large particles composed of four spheres arranged in a pyramid shape (Figure 5.5a). The total particle dimensions are

16 mm in length, width, and height. The robot for the configuration with 8 lugs per wheel is shown in Figure 5.5b.

Table 5.3: Overview of the important simulation parameters used for analysing different lug spacings.

simulation parameter	setting
granular material	dry sand
particle diameter	3 mm
granular bed dimensions	1000x400 mm
granular bed thickness	50 mm
robot dimensions	240x150 mm
robot weight	$\approx$ 2 kg
wheel diameter	100 mm
wheel thickness	20 mm
lug length	10 mm
lug thickness	3 mm
number of lugs	6-10 lugs
wheel angular velocity	5 rad/s
simulation duration	4 s

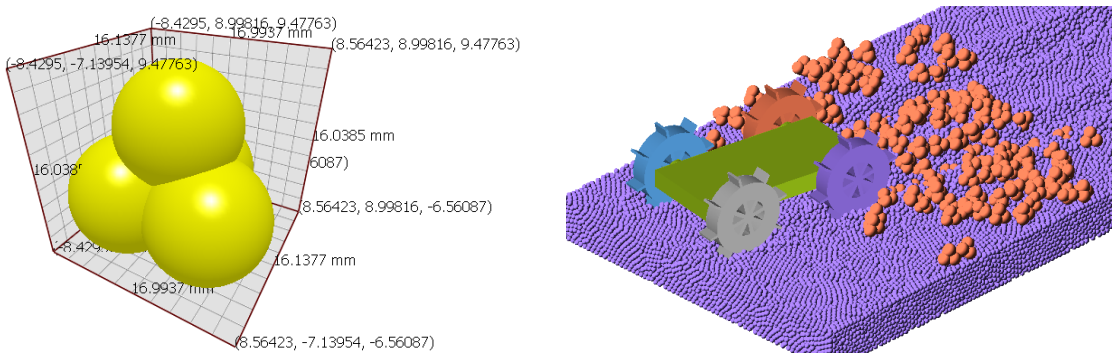

(a) Shape and dimensions of the obstacles.

(b) Simulation with 8 lugs per wheel

Figure 5.5: Motion simulations of robot with two different lug thicknesses.

The performance of each configuration is again evaluated with one KPI, which is the total distance travelled. The results of those simulations are listed in Table 5.4. The results show that the travelling performance increases with an increasing number of lugs, which is as expected from the literature [63]. It is also shown, that for those small obstacles, a wheel with 10 lugs performs better than wheels with 6 and 8 lugs. For the optimized wheel design a lug spacing of 8 lugs per wheel is selected. The tip-tip distance of the wheel with 10 lugs (Table 5.4) is too small for the fabrication of the soft, inflatable elements.

Table 5.4: Total distances travelled for wheels with three different lug spacings.

number of lugs	angle between lugs (deg)	tip-tip distance (mm)	distance travelled (mm)
6	60	47	710
8	45	35	770
10	36	28	830

5.1.6 Optimized Wheel Design

In the previous subsections all wheel parameters have been discussed and determined. A summary of those parameters is given in Table 5.5. The design of the optimized wheel is shown in Figure 5.6. The lugs are not connected to the centre of the wheel, to leave space for the soft, inflatable elements. With this design, the soft, inflatable elements can be combined into one soft body, which requires only one air inlet instead of requiring separate air inlets for each element. The two halves of the wheel are fastened with M3 bolts, which can be added at each lug and in the centre of the wheel. The centre of the wheel is also connected to the robot via a motor coupling nut, which can be inserted into the hexagon hole in the centre of the wheel cover. A more detailed list of all the required parts and their specifications is given in Appendix B. For the air inlet, a hole is added in the main part of the wheel. Both sections of the wheel are 3D-printed by using PLA as the selected material.

Table 5.5: Overview of the wheel parameters for the optimized wheel design.

wheel parameter	value
wheel diameter	120 mm
wheel thickness	20 mm
lug length	12 mm
lug thickness	3 mm
lug spacing	8 lugs

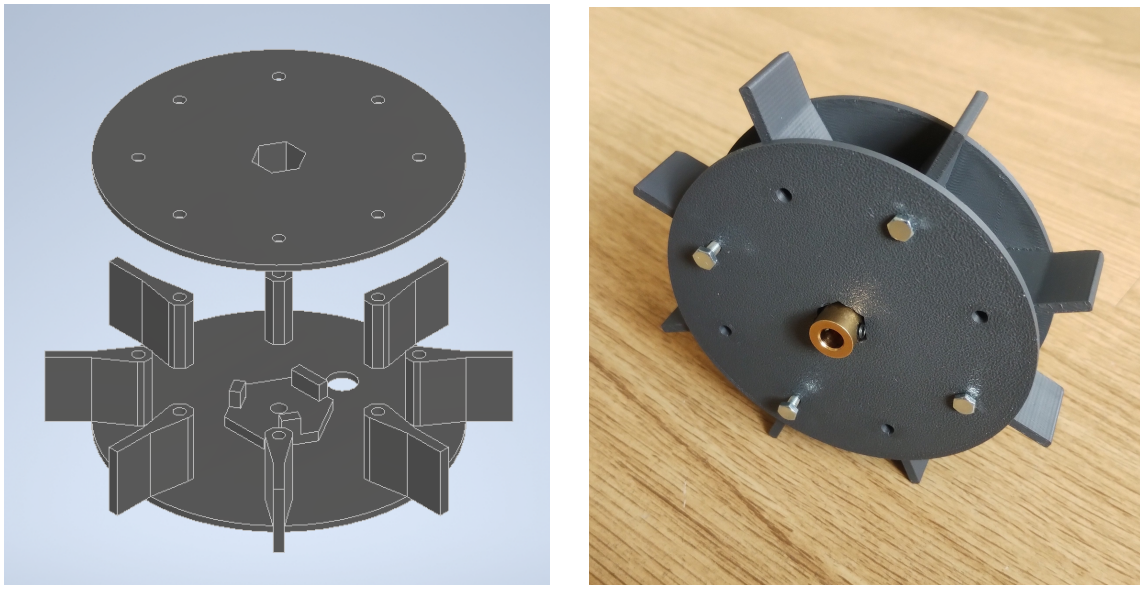

(a) CAD model (b) fabricated wheel

Figure 5.6: CAD model and fabricated model of the optimized wheel design.

5.1.7 Soft Inflatable Elements Design

The soft inflatable elements are combined into one soft body, with one air inlet. The soft elements are placed between the lugs and are connected via a ring in the centre of the wheel. Combing those elements creates the soft, inflatable part shown in Figure 5.7. The soft body can be placed inside the wheel and can be secured by bolting the two wheel parts together. The soft inflatable element has been fabricated by pouring silicone rubber into a mold. A more detailed description of the fabrication method and the mold design is given in Appendix A. The used material is the Smooth-On Ecoflex^{TM} 00-50 rubber. The Ecoflex^{TM} 00-50 material is selected from the available materials because it has the highest shore hardness (00-50). The thickness of the silicone soft part is set to 3 mm, except for the surfaces that can inflate to create the bulb between the lugs. That surface has a thickness of 2 mm and

is indicated in red in Figure 5.7a. The air inlet is constructed by attaching a small tube on the outside of the soft part. A small throttle valve is inserted into the small tube to control the air pressure inside the soft part, which is shown in Figure 5.8b. The assembled wheel is inflated by pressurizing the soft part via the throttle valve, which creates the inflated configuration of the wheel shown in Figure 5.8b.

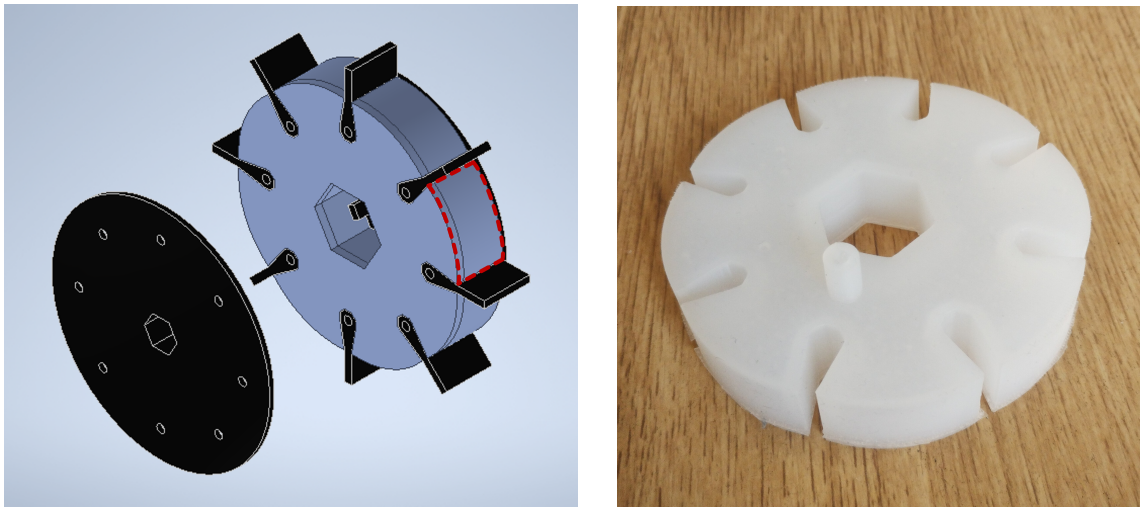

(a) CAD model (b) fabricated silicone part

Figure 5.7: CAD model and fabricated model of the soft, inflatable part.

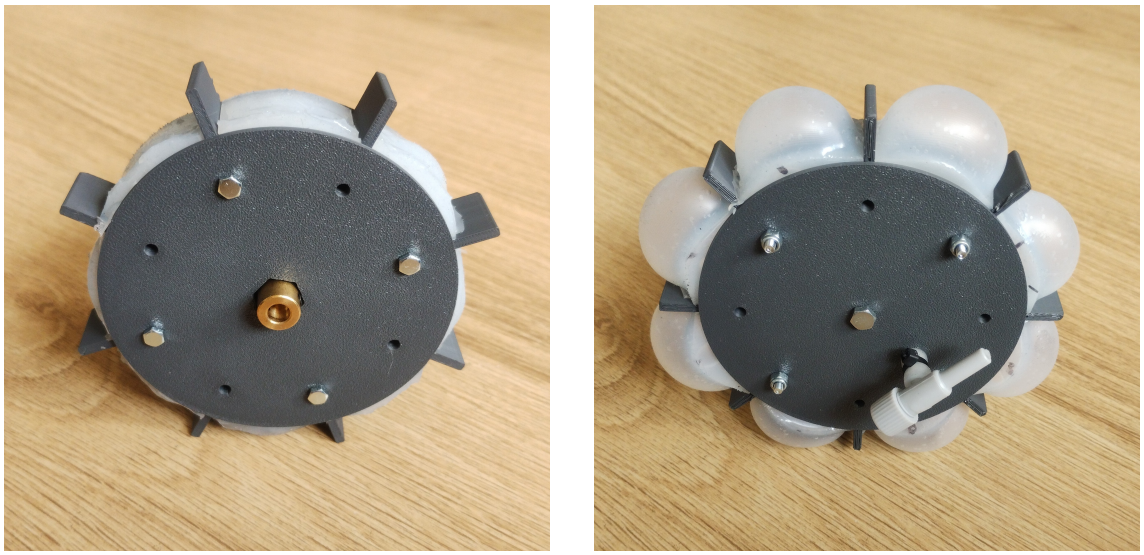

(a) deflated (b) inflated

Figure 5.8: Assembled wheel in inflated and deflated configuration.

5.2 Integrated Robot Design

Not only the wheels have been completely designed, but also the robot chassis and all other corresponding parts. Using an existing robot design and only design new wheels would result in a less optimized robot. In this case, the design of the robot chassis is completely optimized for the wheels and the selected actuators and electronics. This section will explain the integration of all those parts together into one prototype. The designed prototype is a four-wheeled robot, where each wheel is individually actuated by a separate motor (Figures 5.9 and 5.10). The designed structural parts of the prototype are listed in Appendix B. The chassis is designed around those four motors and the total dimensions of the robot are minimized to create a lightweight, small robot prototype. The motors are connected to

the sides of the chassis and an extra bracket is placed on the other end of the motor (see Figure 5.9b). The wheels are connected with the motor shaft via the motor coupling nut. The heaviest component of the robot is the battery, which is placed in the middle of the chassis to optimize the weight distribution (see the red part in Figure 5.9b). The battery cover is designed for easy removal, allowing quick access to the battery. All the other electronic components are placed on top of the robot chassis by using spacer nuts to create some air flow for the cooling (see Figure 5.9a). More details of the electronic parts are explained in Section 5.2.2. A detailed list with all components and their specifications is given in Appendix B. Extra holes have been added in the robot chassis to reduce the weight and to guide the wiring from the components. For the connection of the parts, mostly M3 bolts have been used, which are small and lightweight. The total weight of one wheel is around 135 g and the total weight of the prototype around 2.5 kg. A detailed overview of prototype weight is given in Appendix B, where also the location of the COG of the prototype is shown.

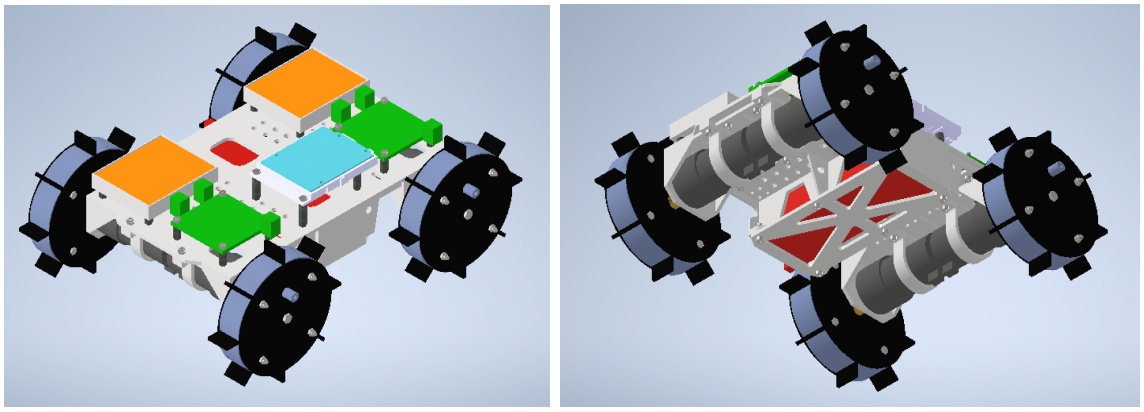

(a) top isometric view (b) bottom isometric view

Figure 5.9: Isometric view of the prototype CAD model.

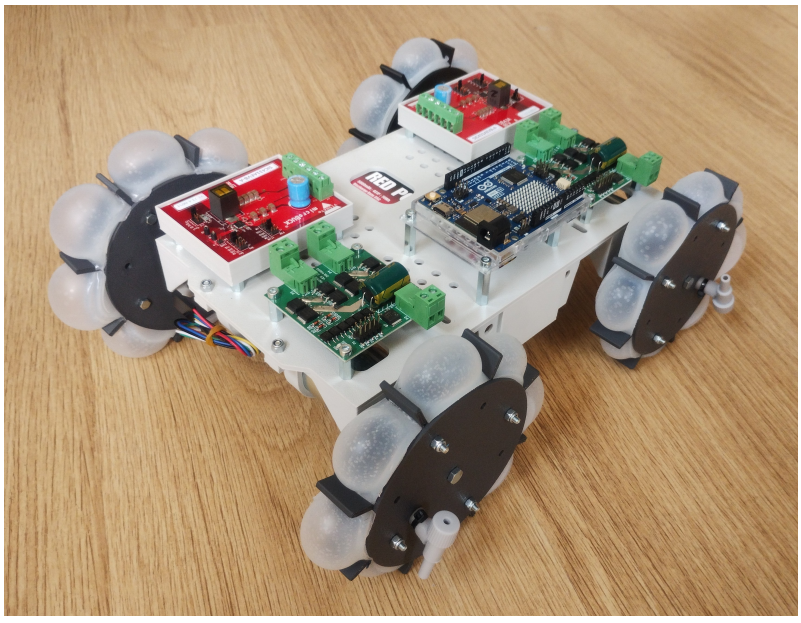

Figure 5.10: Isometric view of the assembled prototype.

The most important parameter for the selection of the motors and electronics is the required torque, which determines the size of the motors and the specifications of the electronic components. The estimation of the required torque and the selection of the motors is explained in the next paragraph (Section 5.2.1). The selection of the electronics based on the selected motor is explained in more detail in Section 5.2.2.

5.2.1 Motor Selection

Two parameters are important for the selection of the motors. The rotational speed of the motor is important, as this determines the speed of the robot. The output rotational speed is often indicated in revolutions per minute (RPM). The second parameter is the motor torque. A certain motor torque is needed to generate propulsion in soft, granular terrains and to traverse obstacles such as slopes. The prototype is used to demonstrate the principle of the shape-shifting, soft wheels. Therefore, the robot should only move at slow speeds. The required torque is estimated by using simulations on soft, granular soil with some obstacles. The used robot model is similar to the simulation model for estimating the performance of the concept design (Section 4.4). The required torque is estimated for a very slow rotational speed of 3 rad/s and a rotational speed of 15 rad/s, which is set as the maximum speed of the robot. The rotational speeds in revolutions per second are given in Table 5.7. The robot motion is simulated for 3 seconds. The used granular material is dry sand and some obstacles are added to evaluate the required torque to traverse those obstacles. The obstacles are large particles composed of four spheres arranged in a pyramid shape, identical to the obstacles defined in Section 5.1.5. The important simulation parameters are listed in Table 5.6. The required torque of each wheel is measured, where the results for the motion simulation of 3 rad/s are shown in Figure 5.11.

Table 5.6: Overview of the important simulation parameters used for the estimation of the required motor torque.

simulation parameter	setting
granular material	dry sand
particle diameter	3 mm
granular bed dimensions	1000x400 mm
granular bed thickness	50 mm
robot dimensions	240x150 mm
robot weight	≈ 2 kg
wheel diameter	100 mm
wheel thickness	20 mm
lug length	10 mm
lug thickness	2 mm
number of lugs	10
wheel angular velocity	3-15 rad/s
simulation duration	3 s

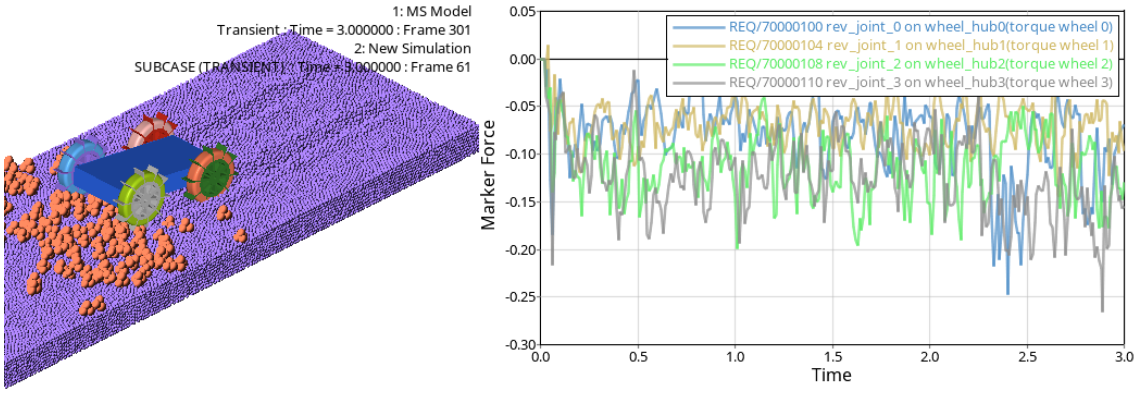

Figure 5.11: Simulation to estimate the required motor torque for a rotational velocity of 3 rad/s.

Table 5.7: Torque estimation for two different rotational velocities.

rotational speed (rad/s)	rotational speed (RPM)	nominal torque (Nm)	peak torque (Nm)
3	29	0.12	0.27
15	143	0.2	0.71

Table 5.7 shows the required nominal and the required peak torque for angular velocities up to 143 RPM. Therefore, the selected motor should have a no-load speed around 200 RPM to ensure that the motor generates enough torque at a speed of 143 RPM (15 rad/s). The stall torque of the motor should be above 1.0 Nm to ensure that there is enough torque available at a speed of 143 RPM. The motor should be a geared DC motor, as the speed of DC motors can be easily controlled. The gearbox is needed to reduce the high rotational speed of the DC motor to the desired rotational speed. Based on the available motors at the suppliers, a DC geared motor with a no-load speed of 251 RPM and a stall torque of 1.77 Nm is selected. More details about the selected DC motor are given in Appendix B.

5.2.2 Electronics Selection

The electronics for the control and power supply of the robot can be selected once the DC motor is selected. The specifications of the DC motor determine the specifications of the electronics in terms of current, voltage and energy consumption. Detailed specifications of all the electronic parts are listed in Appendix B. The battery is selected based on the maximum current, motor voltage and the energy consumption of the motors. The chosen battery technology is lithium-ion polymer (LiPo), as these batteries were available from the supplier and are capable of delivering high discharge currents thanks to their high C-rate. The maximum stall current of the motor is 7 A, so the battery should be capable of delivering 28 A. The operating voltage of the DC motor is 12 V, so a battery with a voltage of 14.8 V is selected to ensure that the input voltage to the motors is 12 V. The motors draw around 1 A when providing the nominal torque, so a battery of 5 Ah is selected to ensure the robot can be operated for approximately one hour.

The speed of the DC motors is controlled by using an Arduino (indicated in blue in Figures 5.9a and 5.12) and a motor driver. The Arduino provides the PWM signal for the motor driver, which regulates the speed of the DC motor. A dual motor driver is selected with a maximum continuous operating current per channel which is equal or higher than the stall current of the motor. The dual motor driver can control the speed of each of the two DC motors independently. One motor driver is used for the front wheels and one for the rear wheels, which are indicated in green in Figures 5.9a and 5.12. One motor driver is also used to power the Arduino with 5 V. This 5 V is generated by the motor driver, which steps down the input voltage of the motor driver. The input voltage of the motor driver and the motors is 12 V and is regulated by two DC-DC converters, one for each motor driver, indicated in orange in Figures 5.9a and 5.12. The DC-DC converter steps down the 14.8 V of the battery to 12 V. The maximum current of the DC-DC converter is also equal or higher than the sum of the stall currents of 2 motors. For safety reasons, a fuse of 20 A is added between the battery and the DC-DC converter and a diode is placed parallel to the DC motor to prevent the motor driver from voltage spikes.

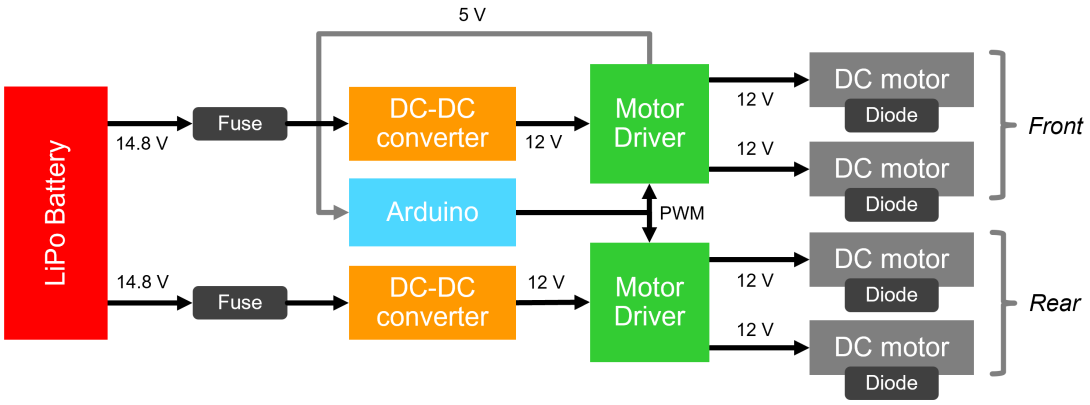

Figure 5.12: Schematic overview of the electronic components of the prototype.

In summary, locomotion simulations have been successfully used to optimize the parameters of the wheel design and to estimate the required torque of the motors. The wheel parameters are selected based on the results of a few locomotion simulations. As a result, a shape-adapting wheel is designed, with a soft silicone inflatable part to adapt the shape of the wheel to different terrains. The wheels are attached to a small and lightweight chassis, which is completely optimized around the selected electronic components. The motor is selected based on the estimation of the required motor torque, which is done by using a few locomotion simulations. The selection of the electronic components is then based on the characteristics of the selected motor.

Chapter 6

Prototype Locomotion Simulations

The prototype design is evaluated with various simulations to get insight into the locomotion performance of each configuration of the prototype on different soil types and for different obstacles. The used simulation method is a co-simulation of DEM and MBD, as explained in Section 3.1. Two configurations of the prototype are evaluated: the fully deflated configuration and the fully inflated configuration. For the deflated configuration, the wheels are modelled as completely rigid (Figure 6.1a), as the soft, inflatable elements will not have significant influence on the performance, since the granular soil contacts only the rigid sides of the wheel. Simulating only rigid bodies decreases the computational time significantly. The inflated configuration is simulated by using the discretized flexbody approach, as explained in Section 3.1.5. The soft, inflated elements will have interaction with the granular material. The discretized flexbody approach models these soft, inflatable elements as a chain of bodies, connected via bushings (Figure 6.1b). The stiffness and damping of the soft, inflated elements are modelled by multiple spring-damper systems, which are connected to each of the bodies of the discretized flexbody.

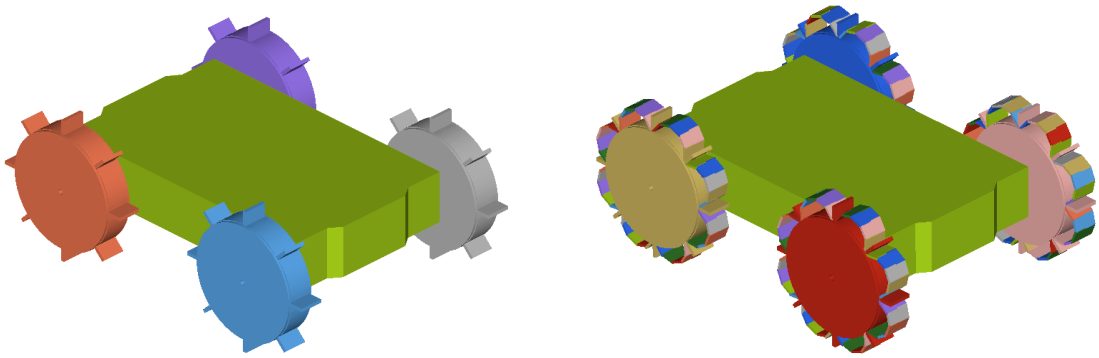

(a) deflated (b) inflated

Figure 6.1: Simulation models for both the deflated and inflated configuration of the prototype.

The performance of the prototype will be evaluated for two different cases. The first case is evaluating the performance of the prototype when climbing a slope of 20 degrees. The generated sand bed is shown in Figure 6.2a, where the total length, width and thickness of the sand bed are 1500 mm, 500 mm and 50 mm respectively. The second case is evaluating the performance of the prototype on a flat, sandy surface that includes a rigid obstacle, shown in Figure 6.2b. The obstacle is modelled as a rigid 30x30 mm square beam. The size of the obstacle is determined based on the body clearance of the prototype, which is approximately 37 mm for normal sinkage. Therefore, the body of the prototype will never touch the obstacle. The dimensions of the flat sand bed are equal to the dimensions of the sloped sand bed. For both sand beds, the particle diameter is 3 mm. Both cases are evaluated for two configurations of the prototype across three types of sandy surfaces with varying moisture content. These surfaces are selected to represent different levels of soil cohesion: dry sand (low cohesion), wet sand (medium cohesion), and very wet sand (high cohesion). Since wet sandy soil is more cohesive than dry sandy soil, testing on these variations allows for evaluating how each configuration performs under different soil conditions.

Simulations are evaluated using two KPIs: static sinkage and total distance travelled. Static sinkage refers to the vertical displacement of the prototype, before motion starts. Wheel motion begins after 0.5 seconds, allowing the prototype to sink into the sandy soil, enabling static sinkage to be estimated at 0.5 seconds. This metric is important, as it affects the prototype's travelling performance. Less sinkage can enable higher speeds, while greater sinkage may improve traction. The second KPI is the estimation of the total distance travelled by the prototype. This KPI reflects the prototype's overall locomotion capability and is used to assess how effectively the prototype moves across the sandy terrains.

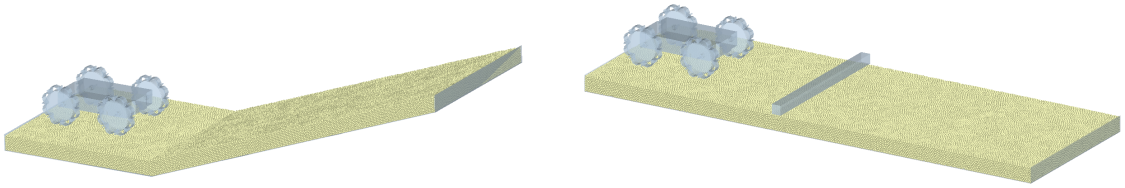

(a) sloped sand bed (b) flat sand bed with obstacle

Figure 6.2: Generated sand beds for the two different simulation cases.

The input parameters for the prototype locomotion simulations are explained in the next section, where also the method is explained to get the right parameters for modelling the soft, inflatable elements. An overview of the prototype locomotion simulations is given in Table 6.2. A total of 12 simulations is required, where 6 simulations are only rigid-body simulations and the other 6 also include the more computational expensive discretized flexbodies. The results of those simulations are presented in Section 6.2

6.1 Simulation Input Parameters

Twelve prototype locomotion simulations were conducted using comparable simulation parameters. A list with the important input parameters that are equal for all simulations is given in Table 6.1. Most of them have already been discussed earlier in the report. However, some of the simulation input parameters are varied per simulation and those parameters are listed in Table 6.2. The simulation duration of the sloped sand bed simulation is a bit longer than the simulation duration of the flat sand bed with obstacles. The travelling of the slope takes more time than travelling on a flat sand bed with obstacles. The timestep is set to 2.0e-05 or 2.5e-05 seconds, corresponding to a Rayleigh percentage of approximately 18%, which is suitable for most of the simulations. However, for the inflated configurations on the loose, dry sand, a lower timestep of 7.0e-06 seconds (≈5%) is used to ensure simulation stability.

Table 6.1: Overview of the important simulation parameters for the prototype locomotion simulations.

simulation parameter	setting
particle diameter	3 mm
granular bed dimensions	1500x500 mm
granular bed thickness	50 mm
robot dimensions	310x225 mm
robot weight	≈ 2.5 kg
wheel diameter	120 mm
wheel thickness	20 mm
lug length	12 mm
lug thickness	3 mm
number of lugs	8 lugs

Table 6.2: Overview of the required simulations with associated simulation parameters.

simulation case	configuration	granular soil type	simulation duration (s)	timestep (s) (Rayleigh %)	torque (%)
slope	deflated	dry sand	3.0	2.5e-05 (≈18%)	75
slope	inflated	dry sand	3.0	5.0e-06 (≈5%)	75
slope	deflated	wet sand	3.0	2.5e-05 (≈18%)	50
slope	inflated	wet sand	3.0	2.0e-05 (≈18%)	50
slope	deflated	very wet sand	3.0	2.5e-05 (≈18%)	50
slope	inflated	very wet sand	3.0	2.0e-05 (≈18%)	50
obstacle	deflated	dry sand	2.5	2.5e-05 (≈18%)	50
obstacle	inflated	dry sand	2.5	7.0e-06 (≈5%)	50
obstacle	deflated	wet sand	2.5	2.5e-05 (≈18%)	50
obstacle	inflated	wet sand	2.5	2.5e-05 (≈18%)	50
obstacle	deflated	very wet sand	2.5	2.5e-05 (≈18%)	50
obstacle	inflated	very wet sand	2.5	2.5e-05 (≈18%)	50

The motion of the wheels is generated by applying a torque to each of the four wheels. In the previous simulations, the angular velocity or angular acceleration was set to define the motion. For these prototype locomotion simulations, the motion of the wheels in the simulation is generated according to the selected motor specifications. The torque applied to the wheels is dependent on the angular velocity of the wheel. The torque applied to each wheel in the MBD simulation is set by using Equation (6.1) [126]. This equation is representing the speed-torque relationship of the DC motor, which is a linear approximation of the motor curve. In Equation (6.1) is τ_m the motor torque, τ_s the stall torque of the motor, ω the rotational speed of the motor and ω_0 the no-load speed of the motor. Figure 6.3 shows this relationship, where the horizontal axis is representing the torque and the vertical axis the rotational speed of the motor. The maximum torque, which is the stall torque τ_s is occurring at zero speed. The maximum speed, which is the no-load speed ω_0, is occurring at zero torque. The motors are not always operated at full power, as this is not the most efficient operating point of the motor. In the simulations, the motors are operated at 50% and 75% of their maximum power. This results in the motors operating at scaled torque and speed values corresponding to these power percentages, following the linear motor characteristic shown in Figure 6.3. Table 6.2 shows the percentage of torque used in each simulation. For most simulations, this percentage is 50%, but for the sloped simulations on the dry sand the percentage is increased to 75% to have enough power to climb the slope.

$$\tau_m = \tau_s\left(1 - \frac{\omega}{\omega_0}\right) \tag{6.1}$$

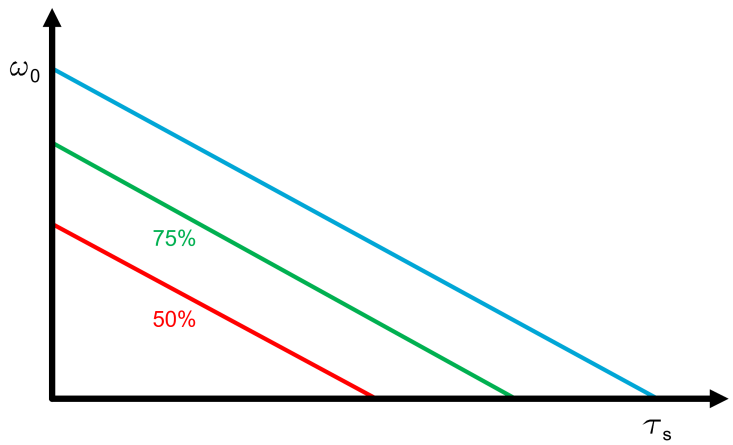

Figure 6.3: Speed-torque relationship for different percentages of motor power.

The input parameters for modelling the discretized flexbodies have to be approximated, as the exact values are unknown. The model of one soft, inflated element is shown in Figure 6.4. For the bushings, four parameters are required. The stiffness in translational and rotational directions of the bushing has to be set in X, Y, and Z direction. The translational and rotational stiffness values have been set to 1000 N/m and 1000 N·m/rad respectively, for all directions, to reduce the number of variables to be approximated.

The translational and rotational damping of the bushings are also set to the same values for all three directions. The damping value is important to achieve stable simulations. A low damping value can cause instability in the simulations. Initially, the translational and rotational damping values of the bushings were set to 5 N·s/m and 5 N·m·s/rad respectively The simulation cases for both wet and very wet sand were completed successfully. The results of those simulations with low damping are added in Appendix C. The simulation for loose, dry sand proved to be unstable, even for a very low timestep. As a result, the robot was unexpectedly launched into the air and the particle bed was exploding, which is shown in Figure 6.5. To solve this problem, the translational and rotational damping values of the bushings have been increased to 15 N·s/m and 15 N·m·s/rad respectively, for all simulations. Due to the increased damping, the peak forces acting on the particles were reduced, resulting in a stable simulation.

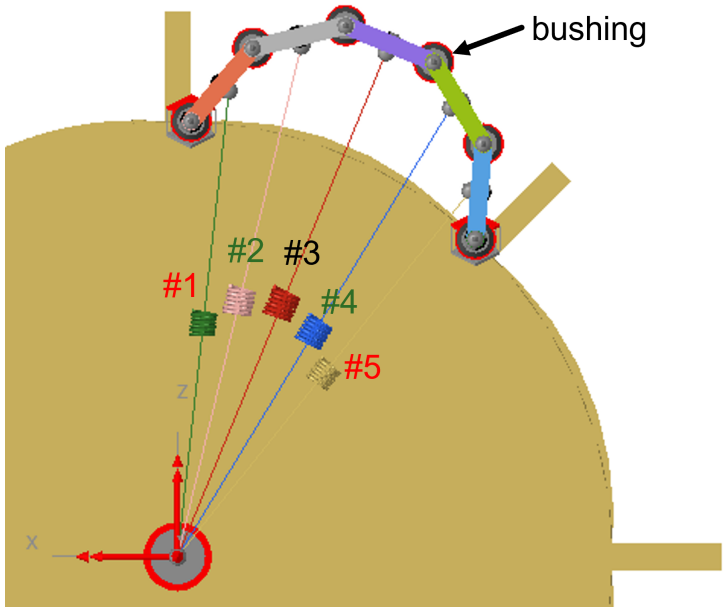

Figure 6.4: Model of one soft, inflated element with the numbered spring-damper systems.

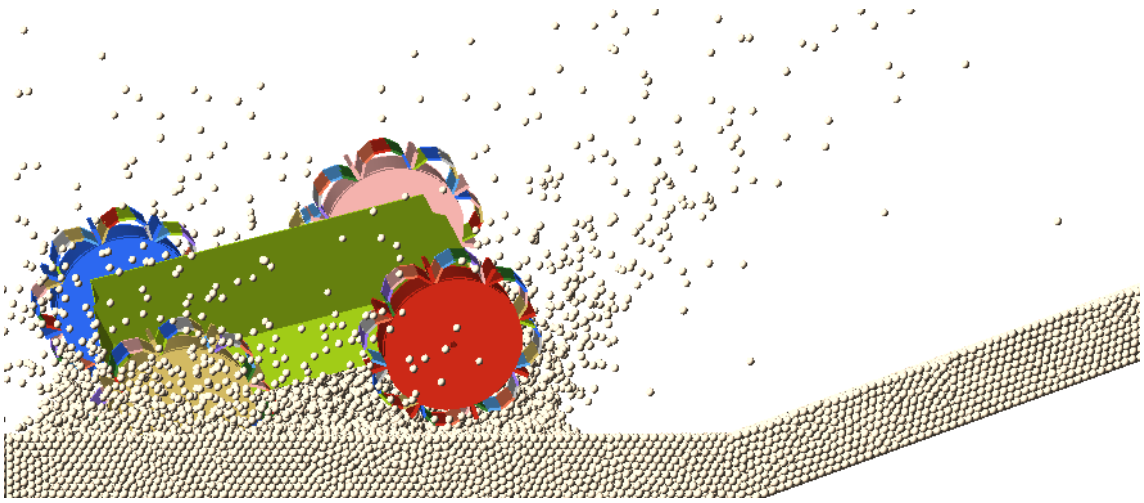

Figure 6.5: Results of an unstable locomotion simulation with loose, dry sand.

For the spring-damper systems, 4 different variables are required. The stiffness values of the springs are not all equal, as the stiffness of the soft, inflated elements is much higher at the sides compared to the stiffness in the middle of the soft, inflated element. The model of one soft, inflated element is shown in Figure 6.4, where the different springs are numbered. The stiffness of spring 1 and 5 are set to the same value of 15 N/m, due to symmetry. The same applies for spring 2 and 4, which values are set to 11 N/m. The stiffness of the middle spring is a separate value, which is 7 N/m. The damping of all springs is considered equally, so one value of 10 N·s/m is set for the damping of the spring-damper systems.

The values of the bushing and spring-damper parameters were estimated by comparing simulation results with experimental observations of the physical prototype. To evaluate the behaviour of the soft, inflated elements when encountering a small obstacle, both simulations and physical experiments were conducted. The obstacle used in both cases was 15 mm high and 30 mm wide. The prototype was slowly driven over the obstacle, and its motion was recorded on video. This footage was then compared to simulations in which the parameter values were varied. Two representative moments, captured both in the experiment and in the corresponding simulations, are shown in Figure 6.6. The parameter set that produced the closest match to the observed behaviour was selected for use in further locomotion simulations. The final parameter values are listed in Table 6.3. The stiffness values of the bushings are set to relatively high values, which is required to achieve stable simulations. Low stiffness values would result in high deformations, which require a smaller timestep to model those deformations. The stiffness of the whole chain of discrete bodies is not solely dependent on the spring stiffness. The stiffness of the bushings is also playing a significant role in determining the softness of the discretized, flexbody. The damping values are also set to high values to reduce the bouncing in the simulation, which enables stable simulations for a higher timestep, and therefore minimizing the computational time.

Table 6.3: Overview of the input parameters for the modelling of the soft, inflatable elements.

simulation parameter	setting
bushing translational stiffness (X,Y,Z)	1000 N/m
bushing rotational stiffness (X,Y,Z)	1000 N·m/rad
bushing translational damping (X,Y,Z)	15 N·s/m
bushing rotational damping (X,Y,Z)	15 N·m·s/rad
spring stiffness #1 & #5	15 N/m
spring stiffness #2 & #4	11 N/m
spring stiffness #3	7 N/m
spring damping	10 N·s/m

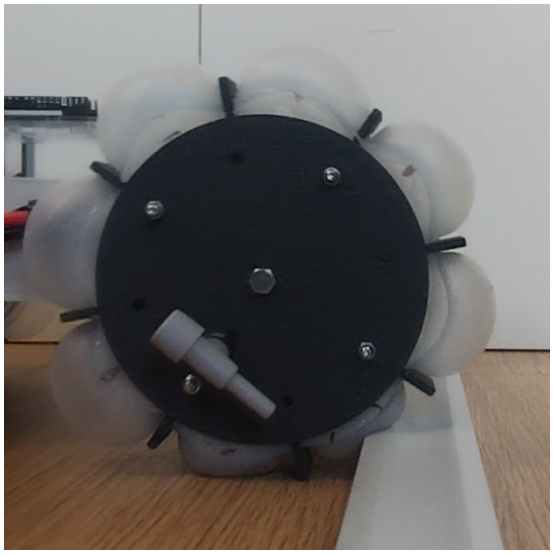

(a) moment 1 physical prototype

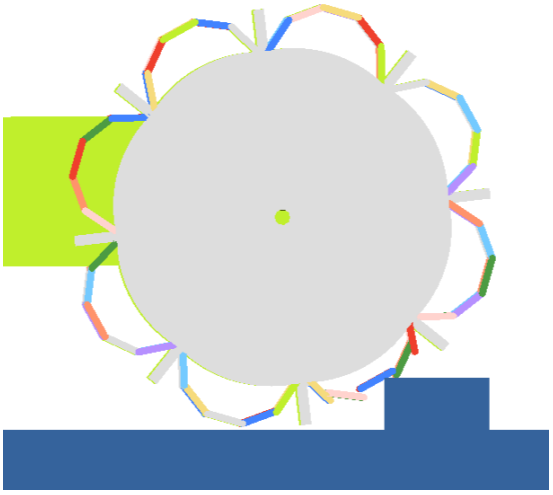

(b) moment 1 simulated prototype

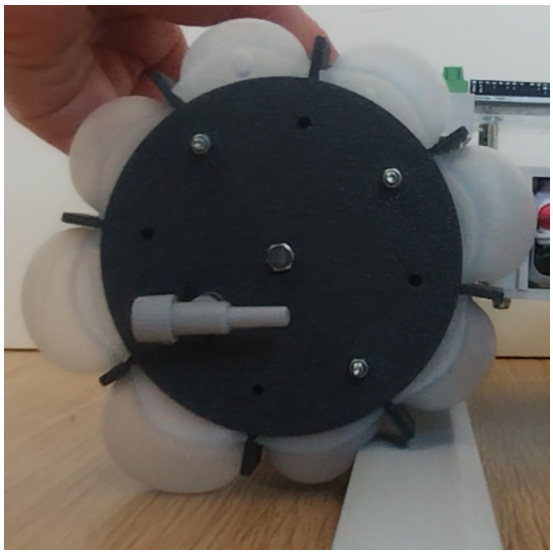

(c) moment 2 physical prototype

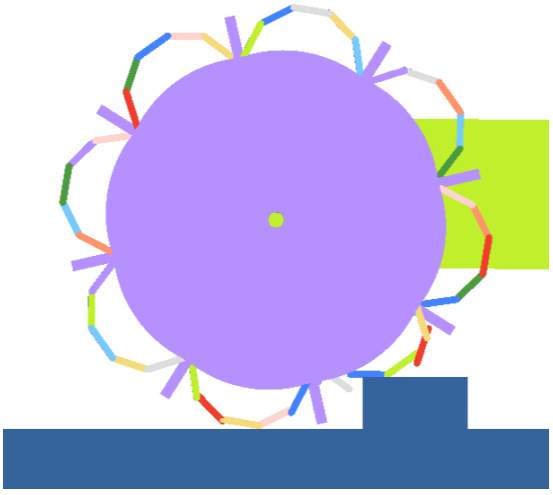

(d) moment 2 simulated prototype

Figure 6.6: Comparison of the prototype and simulation at two key moments during traversal of a 15 mm high, 30 mm wide obstacle.

6.2 Simulation Results

The performance of the prototype is evaluated by using 12 simulations, where half of the simulations are on a sloped sand bed and the other half on a flat sand bed with an obstacle. The results for the inflated configuration on the wet sand beds are shown in Figure 6.7. This figure also indicates how the total distance travelled is computed. For the sloped simulations, the total distance travelled is the distance travelled along the slope, which is indicated with the red line in Figure 6.7a. This distance is estimated by using the horizontal and vertical displacement of the prototype. For the simulations of the flat sand bed with an obstacle, the total distance travelled is equal to the horizontal displacement of the robot, which is indicated with the red line in Figure 6.7b. An overview with the results from all simulations is presented in Table 6.4. Additionally, the travelled distances are also presented per simulation case in a bar plot, which are Figures 6.9 and 6.10. These bar plots show the differences in performance between different soil types and between the two robot configurations.

The computational time of these simulations are approximately 3 hours for the deflated configurations with only rigid bodies. For the more costly inflated configurations with the discretized flexbodies, the computational time is approximately 10 hours, except for the cases on dry sand, where the timestep

is decreased significantly to ensure simulation stability. This difference in simulation stability is due to excessive sinkage and loose particles between the chain of bodies and the rigid wheel hub, as shown in Figure 6.8. The lower timestep of these simulations results in a computational time of approximately 20 hours. All simulations are performed using an Intel® Core™ i7-8750H CPU with 12 cores and a clock speed of 2.20 GHz.

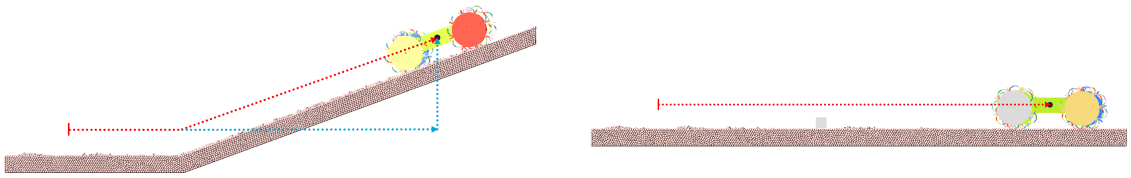

(a) sloped sand bed (b) flat sand bed with obstacle

Figure 6.7: Computation of the total distance travelled for both the sloped and flat sand beds.

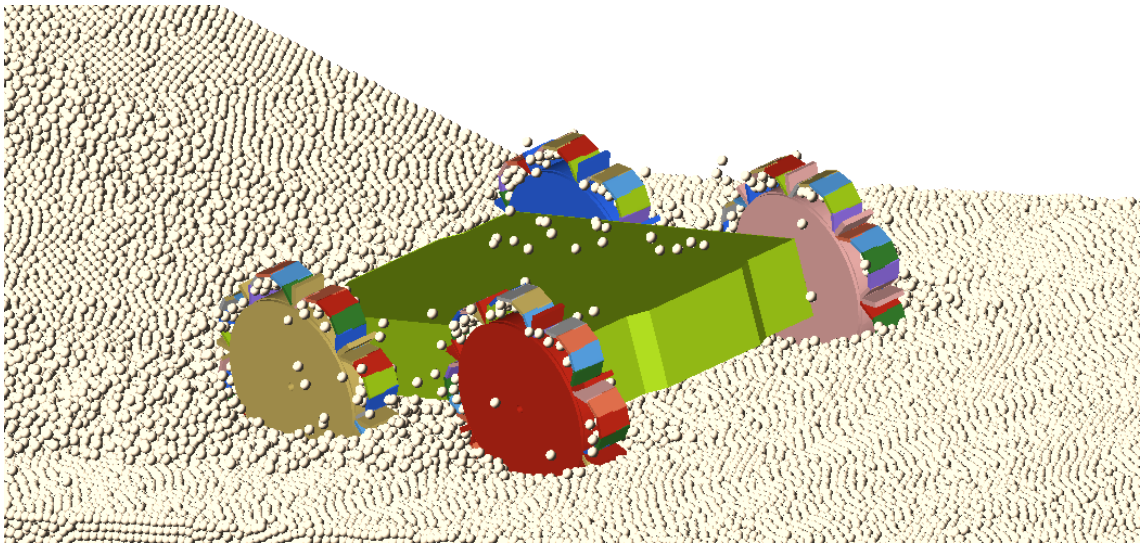

Figure 6.8: Results of the locomotion simulation for the slope of loose, dry sand.

Table 6.4: Overview of prototype locomotion simulations results.

simulation case	configuration	granular soil type	static sinkage (mm)	total distance travelled (mm)
slope	deflated	dry sand	25	754
slope	inflated	dry sand	13	639
slope	deflated	wet sand	16	1087
slope	inflated	wet sand	6	1234
slope	deflated	very wet sand	20	1170
slope	inflated	very wet sand	8	1197
obstacle	deflated	dry sand	24	753
obstacle	inflated	dry sand	12	891
obstacle	deflated	wet sand	15	1096
obstacle	inflated	wet sand	5	1278
obstacle	deflated	very wet sand	19	1142
obstacle	inflated	very wet sand	7	1242

Static sinkage is presented only in Table 6.4. In general, the sinkage of the inflated configurations is lower than for the deflated configurations. So, the inflated configuration minimizes sinkage. As a consequence, the effective wheel diameter is larger compared with the deflated configuration, which improves the travelling performance of the robot. The total distances travelled for each simulation on a sandy slope are also presented visually in Figure 6.9. This figure shows the inflated configuration has a better travelling performance than the deflated configuration on more cohesive sandy soils, due to the larger effective wheel diameter and less sinkage. For the loose, dry sand, the travelling performance is worse for the inflated configuration. It is observed that the inflated robot starts slipping in the loose, dry sand when climbing the slope. This is not the case for the deflated robot. Therefore, the deflated robot configuration with the lugged wheel outperforms the inflated configuration on loose, sandy slopes. This deflated configuration can generate a lot of traction and is therefore very suitable for travelling loose, sandy soils, where large sinkage occurs. The inflated configuration enables faster and more efficient locomotion on more cohesive sandy soils, where less sinkage occurs. Figure 6.9 also shows the difference in travelling performance between a dry sandy slope with no cohesion and a wet sandy slope with cohesion. Moving on dry loose sandy soils is more challenging compared to moving on cohesive sandy soils.

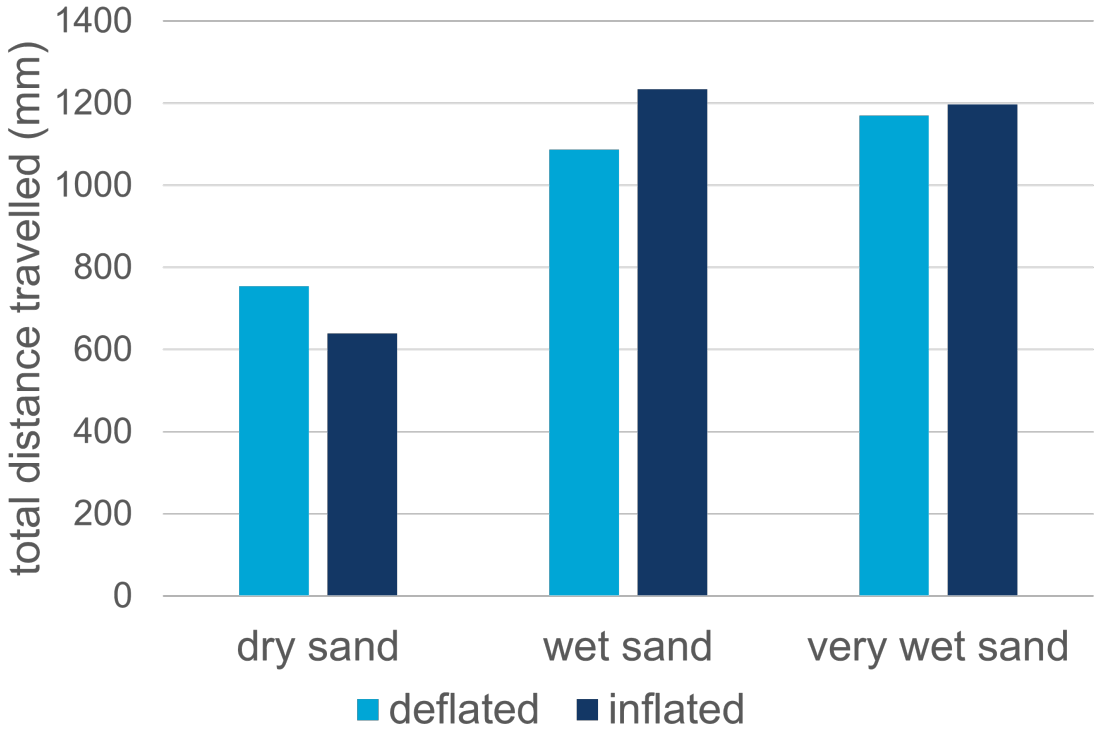

Figure 6.9: Prototype travelling performance on a sloped surface, simulated for three different sandy soils.

For the locomotion simulations with the obstacle, a clear pattern is observed in Figure 6.10. The inflated configurations are always performing better in travelling a flat sand bed with an obstacle. The total distance travelled for the inflated configurations is higher compared with the deflated configurations. When looking to the simulations it is observed that the inflated configurations tackle the obstacle more smoothly and efficiently than the deflated configuration. As a result, the climbing of the obstacle is much more efficient. Therefore, the inflated configuration is always a better choice for traversing obstacles. The soft, inflatable bodies can shape around obstacles, providing strong grip that enables fast and efficient movement. Even on the loose, dry sandy soil the inflated configuration still performs better than the deflated configuration.

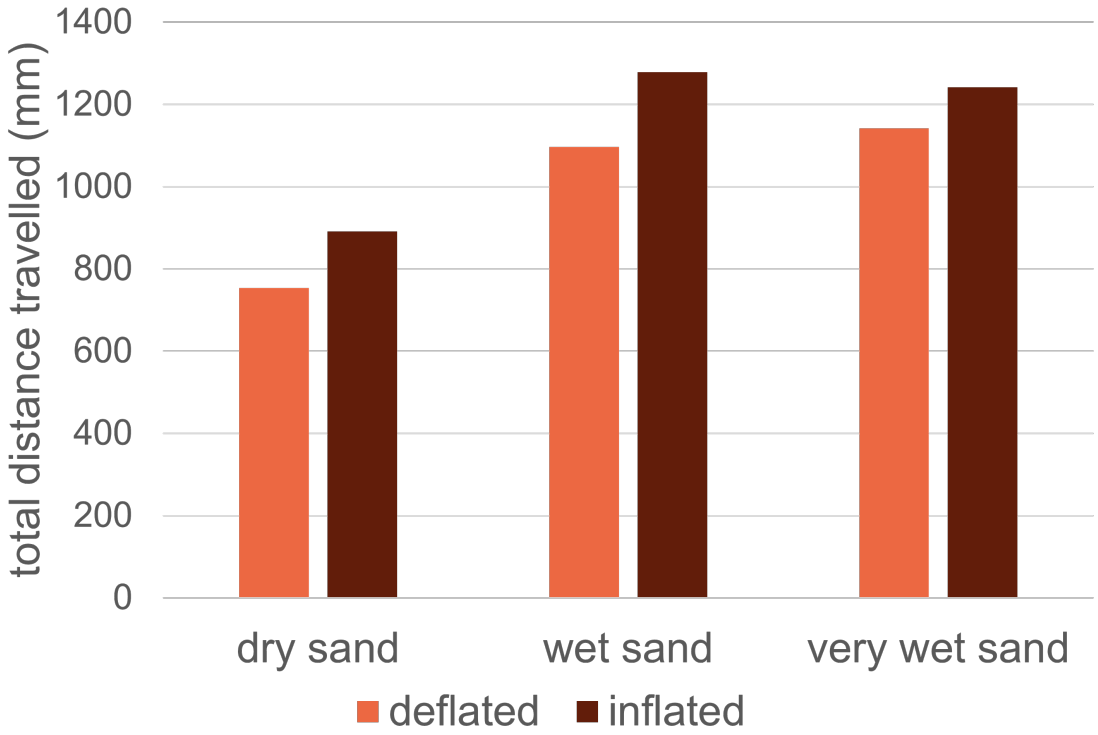

Figure 6.10: Prototype travelling performance on a flat surface with an obstacle, simulated for three different sandy soils.

The performance of a soft, flexible locomotion system can be evaluated using a co-simulation of DEM and MBD, where the soft bodies are modelled using the discretized flexbody representation. The results of the 12 prototype locomotion simulation show the added value of the shape-changing ability of the wheel. The lugged wheel configuration, with the soft bodies deflated, is very suited for travelling loose, sandy soils. The inflated configuration is well-suited for traversing cohesive sandy soils and overcoming obstacles. The added value of the soft, flexible elements in the wheel is clearly visible when travelling obstacles. The behaviour of the shape-adapted wheel is captured accurately. The tuning of the simulation parameters can be difficult, but once the required set of parameters is obtained, the performance of the robot could be evaluated for different configurations on various granular soils.

Chapter 7

Conclusions and Recommendations

The aim of this research was to explore how simulation-aided design could be utilized to develop robotic locomotion methods for sandy terrains. This research is particularly focused on the design of a soft, wheeled locomotion system. A co-simulation method of DEM and MBD is developed to simulate the locomotion of a soft, wheeled locomotion system for various sandy terrains. This simulation method is successfully used in the design process to evaluate the performance of different design configurations. A soft, shape-adapting wheel has been designed and a prototype is constructed. The performance of this prototype is evaluated with the locomotion simulations and the results clearly show the benefits of the shape-adapting wheel design. The use of DEM simulations makes it very easy to evaluate the robot performance on various granular terrains, for example on sandy terrains with a varying moisture content.

Various methods for robotic locomotion on granular surfaces are already available in literature. The most used locomotion methods were legged and wheeled locomotion, where a variety of designs already exist. Besides this, tracked, screw-based, undulatory and vibration-based locomotion methods are also possibilities that could be explored. This research focused on the design of a wheeled locomotion method, which ensures effective movement across longer distances. Multiple KPIs for evaluating the robot's performance are also discussed. KPIs related to manoeuvrability and traction are the most effective in assessing the travelling capabilities of a locomotion system.

Interactions between the robot and the granular terrains can be modelled by various tools. The integration of DEM with MBD simulation is considered the most promising modelling approach for capturing robotic locomotion on granular terrain, because it allows for accurate modelling of both the robot and the granular terrain. The MBD component of the simulation accurately captures the robot's motion and dynamics, while the DEM component effectively models the behaviour of the granular terrain during interaction with the robot. For this research, a particle diameter of 3 mm has been selected, while in reality, sand particles are smaller than 2 mm. A bigger particle diameter is needed to limit the computational cost of the simulations. The soft, flexible bodies can be modelled by using a modal flexbody representation, which is fast and efficient, but not very accurate. It is also possible to use the more accurate discretized flexbody representation. This method models the soft, flexible bodies as a chain of multiple rigid bodies, which are connected via bushings. The stiffness and damping is controlled by using multiple spring-damper systems. This method is more computationally expensive, due to the large number of different elements in this type of simulations. Besides this, it is also more complex to construct or adapt such a simulation model.

The two different flexbody modelling approaches are both used in the design process. The modal flexbody representation is used to evaluate the performance of different concept designs, because these types of models can be easily constructed and the required computational time is low. The selected concept is further detailed into the design of a prototype, where again the modal flexbody representation is used for the optimization of the design parameters. As a result, a shape-adapting wheel is designed, which can be shaped as a lugged wheel and a more circular wheel. Soft, inflatable elements have been placed between the lugs, which can be inflated to change the shape of the wheel. Next to the wheel designs, a robot chassis is designed, which is optimized around the selected motors and electronics, resulting in a lightweight, small robotic prototype with shape-adapting wheels.

The performance of the prototype is only evaluated by simulations and in this case the discretized flexbody representation is used. The locomotion performance of the prototype is evaluated for two robot configurations, inflated and deflated, and for two different cases: a sloped sand bed and a flat

sand bed with an obstacle. Each of these four different simulations is also evaluated for three different sandy soils: dry sand, wet sand and very wet sand. The interaction between the soft, flexible bodies and the granular soil or obstacles can be captured by the simulation, although it remains a simplified representation of reality, due to the small number of discrete bodies. The added-value of the soft, inflatable elements in the wheel can be demonstrated using these type of simulations. The performance of the robotic system on exploring sandy terrains with obstacles is significantly better for the inflated wheel, because the soft elements in the wheel facilitates easier climbing of obstacles. The lugged wheel configuration with deflated, soft elements performs significantly better on loose, dry sandy slopes where a lot of traction is required.

Future research on this topic should focus on utilizing more powerful computers to enhance the accuracy and efficiency of the simulations. By using GPUs and high-performance computing, it becomes feasible to model more complex and softer deformable bodies without significantly increasing the computational time. This would allow for the implementation of fully nodal FEM methods, offering higher accuracy in simulating soft, flexible structures. Increasing the number of bodies for the discretized flexbody representation and lowering the stiffness and damping parameters could improve the realism of the simulations. The stiffness and damping properties of the soft, flexible structures could be quantitatively measured to create a more accurate and realistic representation of the physical soft, flexible bodies. An important direction for future research is the experimental evaluation of the prototype's performance, with the results to be compared to the simulations. Such comparisons would allow for a more thorough assessment of the simulation method's accuracy and help identify areas where the simulation model may require improvements.

On the design side, future work should explore variations in the geometry of the wheel. For example, the shape of the lugs could be made curved or triangular, which may enhance the travelling performance of the robot. The use of stronger soft materials could improve the structural performance and the reliability under load. The soft material could be reinforced with fibres to create a strain-limited layer, which can be used to control the deformation of the soft, flexible structures in the desired directions. Developing more rubber-like wheel constructions with embedded reinforcements could lead to more durable and reliable designs, better suited for the demands of robotic locomotion on unstructured, granular terrains. Combined with improved simulation models, a simulation-aided design approach would enable efficient performance evaluation of various design configurations, minimizing the need for physical prototyping and lowering the development costs.

References

[1] F. Cordes, F. Kirchner, and A. Babu, "Design and field testing of a rover with an actively articulated suspension system in a Mars analog terrain," *Journal of Field Robotics*, vol. 35, no. 7, pp. 1149–1181, Sep. 2018. doi: 10.1002/rob.21808.

[2] J. Toon. "Planetary Exploration Rover Avoids Sand Traps with "Rear Rotator Pedaling"," Georgia Tech. (May 2020), [Online]. Available: https://research.gatech.edu/planetary-exploration-rover-avoids-sand-traps-rear-rotator-pedaling (visited on 11/01/2024).

[3] United Nations, "Percentage of total population living in coastal areas," Technical report, 2007. [Online]. Available: https://www.un.org/esa/sustdev/natlinfo/indicators/methodology_sheets/oceans_seas_coasts/pop_coastal_areas.pdf (visited on 05/19/2025).

[4] The World Factbook. "Field Listing - Coastline." (), [Online]. Available: https://www.cia.gov/the-world-factbook/field/coastline/ (visited on 05/07/2025).

[5] A. Giardino, J. Mulder, J. de Ronde, *et al.*, "Sustainable Development of the Dutch Coast: Present and Future," *Journal of Coastal Research*, no. 61, pp. 166–172, Dec. 2011. doi: 10.2112/SI61-001.11.

[6] A. Luijendijk, G. Hagenaars, R. Ranasinghe, F. Baart, G. Donchyts, and S. Aarninkhof, "The State of the World's Beaches," *Scientific Reports*, vol. 8, art. no. 6641, Apr. 2018. doi: 10.1038/s41598-018-24630-6.

[7] H. Li, J. Sun, and M. Herrmann, "Beyond jamming grippers: granular material in robotics," *Advanced Robotics*, vol. 38, no. 11, pp. 715–729, May 2024. doi: 10.1080/01691864.2024.2348544.

[8] Y. Wang and W. Wu, "A SPH Model Bridging Solid- and Fluid-Like Behaviour in Granular Materials," *Int. Journal for Numerical and Analytical Methods in Geomechanics*, vol. 49, no. 2, pp. 738–755, Feb. 2025. doi: 10.1002/nag.3899.

[9] S. Nilsson. "Pebbles on the Beach," Flickr. (Jun. 2015), [Online]. Available: https://www.flickr.com/photos/infomastern/19627081846 (visited on 04/10/2025).

[10] S. Shrivastava, A. Karsai, Y. Ozkan Aydin, *et al.*, "Material remodeling and unconventional gaits facilitate locomotion of a robophysical rover over granular terrain," *Science Robotics*, vol. 5, no. 42, art. no. eaba3499, May 2020. doi: 10.1126/scirobotics.aba3499.

[11] J. Ma, M. Zhu, T. Zhang, and X. Yue, "The wheel-legged robot for granular terrain: Guardian," in *Proc. 28th Int. Conf. on Mechatronics and Machine Vision in Practice (M2VIP)*, Nanjing, China, Nov. 2022, pp. 1–6. doi: 10.1109/M2VIP55626.2022.10041044.

[12] M.A. Elsheikh, "Design of a special rigid wheel for traversing loose soil," *Scientific Reports*, vol. 13, art. no. 171, Jan. 2023. doi: 10.1038/s41598-022-27312-6.

[13] J.H. Lugo, V. Ramadoss, M. Zoppi, and R. Molfino, "Conceptual design of tetrad-screw propelled omnidirectional all-terrain mobile robot," in *Proc. 2nd Int. Conf. on Control and Robotics Engineering (ICCRE)*, Bangkok, Thailand, Apr. 2017, pp. 13–17. doi: 10.1109/ICCRE.2017.7935033.

[14] X. Chen, F. Gao, Z. Wang, S. Yao, G. Xu, and X. Yao, "Mechanism principle and dynamics simulation on variable diameter walking wheel," in *Proc. Second Int. Conf. on Digital Manufacturing & Automation*, Zhangjiajie, China, Aug. 2011, pp. 723–727. doi: 10.1109/ICDMA.2011.180.

[15] J.V. Salazar Luces, S. Matsuzaki, and Y. Hirata, "RoVaLL: Design and Development of a Multi-Terrain Towed Robot With Variable Lug-Length Wheels," *IEEE Robotics and Automation Letters*, vol. 5, no. 4, pp. 6017–6024, Oct. 2020. doi: 10.1109/LRA.2020.3010495.

[16] Z. Liu, Z. Lu, and K. Karydis, "SoRX: a soft pneumatic hexapedal robot to traverse rough, steep and unstable terrain," in *Proc. IEEE Int. Conf. on Robotics and Automation (ICRA)*, Paris, France, May 2020, pp. 420–426. doi: 10.1109/ICRA40945.2020.9196731.

[17] L. Li, C. Zhao, S. He, Q. Qi, S. Kang, and S. Ma, "Enhancing undulation of soft robots in granular media: A numerical and experimental study on the effect of anisotropic scales," *Biomimetic Intelligence and Robotics*, vol. 4, art. no. 100158, Jun. 2024. doi: 10.1016/j.birob.2024.100158.

[18] D.T. Kühnel, T. Helps, and J. Rossiter, "Kinematic analysis of VibroBot: a soft, hopping robot with stiffness- and shape-changing abilities," *Frontiers in Robotics and AI*, vol. 3, art. no. 60, Oct. 2016. doi: 10.3389/frobt.2016.00060.

[19] H. Jin, J. Lin, W. Wu, Y. Lu, F. Han, and X. Shi, "Interaction mechanics model for screw-drive wheel of granary robot traveling on the loose grain terrain," *Journal of Field Robotics*, vol. 39, no. 6, pp. 827–839, May 2022. doi: 10.1002/rob.22081.

[20] P. Ravula, G. Acar, and B. Balachandran, "Discrete element method-based studies on dynamic interactions of a lugged wheel with granular media," *Journal of Terramechanics*, vol. 94, pp. 49–62, Jan. 2021. doi: 10.1016/j.jterra.2021.01.002.

[21] Altair Engineering, "What is DEM - Theoretical background behind the Discrete Element Method (DEM)." [Online]. Available: https://altair.com/docs/default-source/resource-library/ebook_what_is_dem_theoretical_background_behind_the_discrete_element_method.pdf (visited on 04/07/2025).

[22] R. Bharadwaj, "Using DEM to solve bulk material handling problems," *Chemical Engineering Progress*, vol. 108, no. 9, pp. 54–58, Sep. 2012.

[23] M.G. Catalano, M.J. Pollayil, G. Grioli, *et al.*, "Adaptive feet for quadrupedal walkers," *IEEE Transactions on Robotics*, vol. 38, no. 1, pp. 302–316, Feb. 2022. doi: 10.1109/TRO.2021.3088060.

[24] X. Xiong, A.D. Ames, and D.I. Goldman, "A stability region criterion for flat-footed bipedal walking on deformable granular terrain," in *Proc. IEEE/RSJ Int. Conf. on Intelligent Robots and Systems (IROS)*, Vancouver, Canada, Sep. 2017, pp. 4552–4559. doi: 10.1109/IROS.2017.8206323.

[25] J.R. Gosyne, C.M. Hubicki, X. Xiong, A.D. Ames, and D.I. Goldman, "Bipedal locomotion up sandy slopes: systematic experiments using zero moment point methods," in *Proc. IEEE-RAS 18th Int. Conf. on Humanoid Robots (Humanoids)*, Beijing, China, Nov. 2018, pp. 994–1001. doi: 10.1109/HUMANOIDS.2018.8624959.

[26] X. Guo, B. Blaise, J. Molnar, *et al.*, "Soft foot sensor design and terrain classification for dynamic legged locomotion," in *Proc. IEEE Int. Conf. on Soft Robotics (RoboSoft)*, New Haven, Connecticut, USA, May 2020, pp. 550–557. doi: 10.1109/RoboSoft48309.2020.9115990.

[27] X. Chen, J. Yi, and H. Wang, "Energy efficient foot-shape design for bipedal walkers on granular terrain," in *Proc. Modeling, Estimation and Control Conf. (MECC)*, Lake Tahoe, USA, Oct. 2023, pp. 601–606. doi: 10.1016/j.ifacol.2023.12.090.

[28] X. Chen, A. Anikode, J. Yi, and T. Liu, "Foot shape-dependent resistive force model for bipedal walkers on granular terrains," in *Proc. IEEE Int. Conf. on Robotics and Automation (ICRA)*, Yokahama, Japan, May 2024, pp. 13 093–13 099. doi: 10.1109/ICRA57147.2024.10610190.

[29] R. Zhang, X. Sun, D. Han, *et al.*, "A bionic mechanical foot with adaptive variable postures travelling on sand," *Journal of Terramechanics*, vol. 107, pp. 61–74, Mar. 2023. doi: 10.1016/j.jterra.2023.03.004.

[30] C.D. Remy, O. Baur, M. Latta, *et al.*, "Walking and crawling with ALoF: a robot for autonomous locomotion on four legs," *Industrial Robot*, vol. 38, no. 3, pp. 264–268, May 2011. doi: 10.1108/01439911111122761.

[31] S. Hauser, M. Mutlu, P. Banzet, and A.J. Ijspeert, "Compliant universal grippers as adaptive feet in legged robots," *Advanced Robotics*, vol. 32, no. 15, pp. 825–836, Jul. 2018. doi: 10.1080/01691864.2018.1496851.

[32] R. Käslin, H. Kolvenbach, L. Paez, K. Lika, and M. Hutter, "Towards a passive adaptive planar foot with ground orientation and contact force sensing for legged robots," in *Proc. IEEE/RSJ Int. Conf. on Intelligent Robots and Systems (IROS)*, Madrid, Spain, Oct. 2018, pp. 2707–2714. doi: 10.1109/IROS.2018.8593875.

[33] C. Yao, G. Shi, P. Xu, *et al.*, "STAF: Interaction-based design and evaluation of sensorized terrain-adaptive foot for legged robot traversing on soft slopes," *IEEE/ASME Transactions on Mechatronics*, pp. 1–12, Jan. 2024. doi: 10.1109/TMECH.2024.3350183.

[34] C. Li, P.B. Umbanhowar, H. Komsuoglu, and D.I. Goldman, "The effect of limb kinematics on the speed of a legged robot on granular media," *Experimental Mechanics*, vol. 50, pp. 1383–1393, Apr. 2010. doi: 10.1007/s11340-010-9347-1.

[35] L. Xu, X. Liang, M. Xu, B. Liu, and S. Zhang, "Interplay of theory and experiment in analysis of the advantage of the novel semi-elliptical leg moving on loose soil," in *Proc. IEEE/ASME Int. Conf. on Advanced Intelligent Mechatronics*, Wollongong, Australia, Jul. 2013, pp. 26–31. doi: 10.1109/AIM.2013.6584063.

[36] S. Zhang, X. Liang, L. Xu, and M. Xu, "Initial development of a novel amphibious robot with transformable fin-leg composite propulsion mechanisms," *Journal of Bionic Engineering*, vol. 10, no. 4, pp. 434–445, Oct. 2013. doi: 10.1016/S1672-6529(13)60247-4.

[37] C. Li, A.M. Hoover, P. Birkmeyer, P.B. Umbanhowar, R.S. Fearing, and D.I. Goldman, "Systematic study of the performance of small robots on controlled laboratory substrates," in *Proc. of SPIE 7679, Micro- and Nanotechnology Sensors, Systems, and Applications II*, vol. 76790Z, Orlando, Florida, USA, May 2010. doi: 10.1117/12.851047.

[38] T. Zhang, F. Qian, C. Li, *et al.*, "Ground fluidization promotes rapid running of a lightweight robot," *The International Journal of Robotics Research*, vol. 32, no. 7, pp. 859–869, Jul. 2013. doi: 10.1177/0278364913481690.

[39] C. Li, P.B. Umbanhowar, H. Komsuoglu, D.E. Koditschek, and D.I. Goldman, "Sensitive dependence of the motion of a legged robot on granular media," in *Proc. of the National Academy of Sciences of the United States of America*, vol. 106, Mar. 2009, pp. 3029–3034. doi: 10.1073/pnas.0809095106.

[40] F. Qian, T. Zhang, W. Korff, P.B. Umbanhowar, R.J. Full, and D.I. Goldman, "Principles of appendage design in robots and animals determining terradynamic performance on flowable ground," *Bioinspiration & Biomimetics*, vol. 10, no. 5, art. no. 056014, Oct. 2015. doi: 10.1088/1748-3190/10/5/056014.

[41] F. Qian, K. Daffon, T. Zhang, and D.I. Goldman, "An automated system for systematic testing of locomotion on heterogeneous granular media," in *Proc. of the 16th Int. Conf. on Climbing and Walking Robots (CLAWAR)*, 2013, pp. 1–8. doi: 10.1142/9789814525534_0069.

[42] C. Li, T. Zhang, and D.I. Goldman, "A terradynamics of legged locomotion on granular media," *Science*, vol. 339, no. 6126, pp. 1408–1412, Mar. 2013. doi: 10.1126/science.1229163.

[43] X. Zhu, D. Ran, C. Xiang, *et al.*, "Design, analysis and experiments of bionic hexapod robot with multilayer c-shape legs for unstructered terrain," in *Proc. 13th World Congress on Intelligent Control and Automation (WCICA)*, Changsha, China, Jul. 2018, pp. 438–443. doi: 10.1109/WCICA.2018.8630361.

[44] C. Li, T. Zhang, and D.I. Goldman, "A resistive force model for legged locomotion on granular media," in *Proc. of the 15th Int. Conf. on Climbing and Walking Robots (CLAWAR)*, Sep. 2012, pp. 433–440. doi: 10.1142/9789814415958_0056.

[45] H. Bagheri, V. Taduru, S. Panchal, S. White, and H. Marvi, "Animal and robotic locomotion on wet granular media," in *Proc. Biomimetic and Biohybrid Systems, Living Machines 2017*, Stanford, California, USA, Jul. 2017, pp. 13–24. doi: 10.1007/978-3-319-63537-8_2.

[46] H. Bagheri, V. Jayanetti, H.R. Burch, C.E. Brenner, B.R. Bethke, and H. Marvi, "Mechanics of bipedal and quadrupedal locomotion on dry and wet granular media," *Journal of Field Robotics*, vol. 40, no. 2, pp. 161–172, Sep. 2022. doi: 10.1002/rob.22121.

[47] K. Lee, S. Ahn, K.Y. Yoo, D. Yoon, and T. Seo, "Empirical study on characteristics of angled spoke-based wheels on granular media," *International Journal of Precision Engineering and Manufacturing*, vol. 23, pp. 1163–1171, Aug. 2022. doi: 10.1007/s12541-022-00693-4.

[48] X. Ma, G. Wang, and K. Liu, "Design and optimization of a multimode amphibious robot with propeller-leg," *IEEE Transactions on Robotics*, vol. 38, no. 6, pp. 3807–3820, Dec. 2022. doi: 10.1109/TRO.2022.3182880.

[49] N. Mazouchova, P.B. Umbanhowar, and D.I. Goldman, "Flipper-driven terrestrial locomotion of a sea turtle-inspired robot," *Bioinspiration & Biomimetics*, vol. 8, art. no. 026007, Apr. 2013. doi: 10.1088/1748-3182/8/2/026007.

[50] Y. Ozkan Aydin, B. Chong, C. Gong, *et al.*, "Geometric mechanics applied to tetrapod locomotion on granular media," in *Proc. Biomimetic and Biohybrid Systems, Living Machines 2017*, Stanford, California, USA, Jul. 2017, pp. 595–603. doi: 10.1007/978-3-319-63537-8_55.

[51] B. Chong, Y. Ozkan Aydin, C. Gong, *et al.*, "Coordination of lateral body bending and leg movements for sprawled posture quadrupedal locomotion," *The Int. Journal of Robotics Research*, vol. 40, no. 4-5, pp. 747–763, Jan. 2021. doi: 10.1177/0278364921991158.

[52] G. Chen, L. Qiao, B. Wang, L. Richter, and A. Ji, "Bionic design of multi-toe quadruped robot for planetary surface exploration," *Machines*, vol. 10, art. no. 827, Sep. 2022. doi: 10.3390/machines10100827.

[53] G. Chen, L. Qiao, Z. Zhou, X. Lei, L. Richter, and A. Ji, "Biomimetic lizard robot for adapting to Martian surface terrain," *Bioinspiration & Biomimetics*, vol. 19, art. no. 036005, Mar. 2024. doi: 10.1088/1748-3190/ad311d.

[54] S. Roberts and D.E. Koditschek, "Reactive velocity control reduces energetic cost of jumping with a virtual leg spring on simulated granular media," in *Proc. IEEE Int. Conf. on Robotics and Biomimetics (ROBIO)*, Kuala Lumpur, Malaysia, Dec. 2018, pp. 1397–1404. doi: 10.1109/ROBIO.2018.8664858.

[55] S. Roberts and D.E. Koditschek, "Mitigating energy loss in a robot hopping on a physically emulated dissipative substrate," in *Proc. Int. Conf. on Robotics and Automation (ICRA)*, Montreal, Canada, May 2019, pp. 6763–6769. doi: 10.1109/ICRA.2019.8793781.

[56] S. Roberts and D.E. Koditschek, "Virtual energy management for physical energy savings in a legged robot hopping on granular media," *Frontiers in Robotics and AI*, vol. 8, Dec. 2021. doi: 10.3389/frobt.2021.740927.

[57] T.J.K. Buchner, T. Fukushima, A. Kazemipour, *et al.*, "Electrohydraulic musculoskeletal robotic leg for agile, adaptive, yet energy-efficient locomotion," *Nature Communications*, vol. 15, art. no. 7634, Sep. 2024. doi: 10.1038/s41467-024-51568-3.

[58] T. Hojnik, R.A. Dungavell, P.D. Flick, and J.M. Roberts, "Wheeled rovers with posable hubs for terrestrial and extraterrestrial exploration," *IEEE Access*, vol. 8, pp. 154 318–154 328, Aug. 2020. doi: 10.1109/ACCESS.2020.3018429.

[59] D.N. Kuzmenko and E.A. Lazarev, "Investigation of a planetary rover locomotion system with wheel-walking propulsion by applying the method of object-oriented modeling," *Indian Journal of Science and Technology*, vol. 9, no. 42, pp. 1–13, Nov. 2016. doi: 10.17485/ijst/2016/v9i42/104267.

[60] G. Andrade, F.B. Amar, P. Bidaud, and R. Chatila, "Modeling robot-soil interaction for planetary rover motion control," in *Proc. IEEE/RSJ Int. Conf. on Intelligent Robots and Systems*, Victoria, Canada, Oct. 1998, pp. 576–581. doi: 10.1109/IROS.1998.724680.

[61] K. Nagatani, A. Ikeda, K. Sato, and K. Yoshida, "Accurate estimation of drawbar pull of wheeled mobile robots traversing sandy terrain using built-in force sensor array wheel," in *Proc. IEEE/RSJ Int. Conf. on Intelligent Robots and Systems*, St. Louis, Missouri, USA, Oct. 2009, pp. 2373–2378. doi: 10.1109/IROS.2009.5354566.

[62] K. Iizuka, T. Kubota, and T. Kubota, "Measurement of stress distribution of flexible wheel for lunar rover," in *Proc. Joint 41st Int. Symposium on Robotics and 6th German Conf. on Robotics (ISR/ROBOTIK)*, Munich, Germany, Jun. 2010, pp. 842–847. [Online]. Available: https://ieeexplore.ieee.org/document/5756886.

[63] M. Sutoh, K. Nagaoka, K. Nagatani, and K. Yoshida, "Evaluation of influence of surface shape of locomotion mechanism on traveling performance of planetary rovers," in *Proc. IEEE Int. Conf. on Robotics and Automation*, Saint Paul, Minnesota, USA, May 2012, pp. 3419–3424. doi: 10.1109/ICRA.2012.6225024.

[64] Y. Nakane, K. Iizuka, and T. Kubota, "Experimental study of grouser's effect for planetary rovers based on terramechanics," in *Proc. First Int. Conf. on Robot Intelligence Technology and Applications (RiTA)*, Gwangju, Korea, Dec. 2012, pp. 641–652. doi: 10.1007/978-3-642-37374-9_61.

[65] L. Ding, H. Gao, Y. Li, G. Liu, and Z. Deng, "Improved explicit-form equations for estimating dynamic wheel sinkage and compaction resistance on deformable terrain," *Mechanism and Machine Theory*, vol. 86, pp. 235–264, Jan. 2015. doi: 10.1016/j.mechmachtheory.2014.12.011.

[66] M. Laîné, C. Tamakoshi, M. Touboulic, J. Walker, and K. Yoshida, "Initial design characteristics, testing and performance optimisation for a lunar exploration micro-rover prototype," *Advances in Astronautics Science and Technology*, vol. 1, pp. 111–117, Aug. 2018. doi: 10.1007/s42423-018-0007-3.

[67] L. Huang, J. Zhu, Y. Yuan, and Y. Yin, "A dynamic resistive force model for designing mobile robot in granular media," *IEEE Robotics and Automation Letters*, vol. 7, no. 2, pp. 5357–5364, Apr. 2022. doi: 10.1109/LRA.2022.3156636.

[68] S.M. Felton, D.-Y. Lee, K.-J Cho, and R.J. Wood, "A passive, origami-inspired, continuously variable transmission," in *Proc. IEEE Int. Conf. on Robotics and Automation (ICRA)*, Hong Kong, China, May 2014, pp. 2913–2918. doi: 10.1109/ICRA.2014.6907278.

[69] L. Zheng, P. Zhang, Y. Hu, G. Yu, Z. Song, and J. Zhang, "A Novel High Adaptability Outdoor Mobile Robot with Diameter-variable Wheels," in *Proc. IEEE Int. Conf. on Information and Automation*, Shenzhen, China, Jun. 2011, pp. 169–174. doi: 10.1109/ICINFA.2011.5948982.

[70] S.-C. Chen, K.-J. Huang, W.-H. Chen, S.-Y. Shen, C.-H. Li, and P.-C. Lin, "Quattroped: A Leg–Wheel Transformable Robot," *IEEE/ASME Transactions on Mechatronics*, vol. 19, no. 2, pp. 730–742, Apr. 2014. doi: 10.1109/TMECH.2013.2253615.

[71] Y.-S. Kim, G.-P. Jung, H. Kim, K.-J. Cho, and C.-N. Chu, "Wheel Transformer: A Wheel-Leg Hybrid Robot With Passive Transformable Wheels," *IEEE Transactions on Robotics*, vol. 30, no. 6, pp. 1487–1498, Dec. 2014. doi: 10.1109/TRO.2014.2365651.

[72] W.-H. Chen, H.-S. Lin, Y.-M. Lin, and P.-C. Lin, "TurboQuad: A Novel Leg–Wheel Transformable Robot With Smooth and Fast Behavioral Transitions," *IEEE Transactions on Robotics*, vol. 33, no. 5, pp. 1025–1040, Oct. 2017. doi: 10.1109/TRO.2017.2696022.

[73] S.-S. Yun, J.-Y. Lee, G.-P. Jung, and K.-J. Cho, "Development of a Transformable Wheel Actuated by Soft Pneumatic Actuators," *Int. Journal of Control, Automation and Systems*, vol. 15, no. 1, pp. 36–44, Jan. 2017. doi: 10.1007/s12555-016-0477-9.

[74] H. Yoon, K. Lee, J. Lee, J. Kwon, and T. Seo, "The stiffness adjustable wheel mechanism based on compliant spoke deformation," *Scientific Reports*, vol. 14, art. no. 773, Jan. 2024. doi: 10.1038/s41598-024-51493-x.

[75] R. Gkliva and M. Kruusmaa, "Soft fluidic actuator for locomotion in multi-phase environments," *IEEE Robotics and Automation Letters*, vol. 7, no. 4, pp. 10 462–10 469, Oct. 2022. doi: 10.1109/LRA.2022.3192204.

[76] D. Fujiwara and K. Iizuka, "Study on bearing performance for inching worm locomotion using characteristics of wheel subsidence on loose soil," in *Proc. IEEE/ASME Int. Conf. on Advanced Intelligent Mechatronics (AIM)*, Auckland, New Zealand, Jul. 2018, pp. 930–935. doi: 10.1109/AIM.2018.8452437.

[77] D. Fuijwara, K. Iizuka, D. Asami, T. Kawamura, and S. Suzuki, "Study on traveling performance for variable wheel-base robot using subsidence effect," *International Journal of Mechanical Engineering and Robotics Research*, vol. 8, no. 2, pp. 233–238, Mar. 2019. doi: 10.18178/ijmerr.8.2.233-238.

[78] A.J.R. Lopez-Arreguin and S. Montenegro, "Towards bio-inspired robots for underground and surface exploration in planetary environments: An overview and novel developments inspired in sand-swimmers," *Heliyon*, vol. 6, art. no. e04148, Jun. 2020. doi: 10.1016/j.heliyon.2020.e04148.

[79] K. Nagatani, H. Kinoshita, K. Yoshida, K. Tadakuma, and E. Koyanagi, "Development of leg-track hybrid locomotion to traverse loose slopes and irregular terrain," *Journal of Field Robotics*, vol. 28, no. 6, pp. 950–960, Oct. 2011. doi: 10.1002/rob.20415.

[80] V. Gomez, M. Hernando, E. Aguado, R. Sanz, and C. Rossi, "ROBOMINER: Development of a Highly Configurable and Modular Scaled-Down Prototype of a Mining Robot," *Machines*, vol. 11, art. no. 809, Aug. 2023. doi: 10.3390/machines11080809.

[81] K. Nagaoka, M. Otsuki, T. Kubota, and S. Tanaka, "Terramechanics-based propulsive characteristics of mobile robot driven by Archimedean screw mechanism on soft soil," in *Proc. IEEE/RSJ Int. Conf. on Intelligent Robots and Systems*, Taipei, Taiwan, Oct. 2010, pp. 4946–4951. doi: 10.1109/IROS.2010.5651010.

[82] E. Marteau, L.P. Tosse, M. Veismann, *et al.*, "To boldly go where no robots have gone before - Part 3: Characterizing the performance of screw propulsion for robus surface and subsurface mobility of EELS on highly unknown terrains," presented at the AIAA SciTech Forum, Orlando, Florida, USA, Jan. 2024. doi: 10.2514/6.2024-1959.

[83] H. Jin, Y. Lu, W. Wu, and F. Han, "Influence of screw blades on the performance of a screw-drive granary robot," *Journal of Field Robotics*, vol. 41, no. 7, pp. 2133–2146, Jun. 2024. doi: 10.1002/rob.22220.

[84] R. Gkliva, W. Remmas, S. Godon, *et al.*, "A Multi-Terrain Robot Prototype With Archimedean Screw Actuators: Design, Realization, Modeling, and Control," *IEEE Access*, vol. 12, pp. 95 820–95 830, Jul. 2024. doi: 10.1109/ACCESS.2024.3426105.

[85] C. Branyan and Y. Mengüç, "Soft snake robots: Investigating the effects of gait parameters on locomotion in complex terrains," in *Proc. IEEE/RSJ Int. Conf. on Intelligent Robots and Systems (IROS)*, Madrid, Spain, Oct. 2018, pp. 7521–7526. doi: 10.1109/IROS.2018.8593404.

[86] H. Marvi, C. Gong, N. Gravish, *et al.*, "Sidewinding with minimal slip: Snake and robot ascent of sandy slopes," *Science*, vol. 346, no. 6206, pp. 224–229, Oct. 2014. doi: 10.1126/science.1255718.

[87] F. Rozaidi, E. Waters, O. Dawes, J. Yang, J.R. Davidson, and R.L. Hatton, "HISSbot: Sidewinding with a soft snake robot," in *Proc. IEEE Int. Conf. on Soft Robotics (RoboSoft)*, Singapore, Singapore, Apr. 2023, pp. 1–7. doi: 10.1109/RoboSoft55895.2023.10121961.

[88] L. Huang, H. Ming, and Y. Yin, "A novel sidewinding snake robot with non-zero slope in granular terrains modeled by DRFM," in *Proc. IEEE/ASME Int. Conf. on Advanced Intelligent Mechatronics (AIM)*, Seattle, Washington, USA, Jun. 2023, pp. 1238–1245. doi: 10.1109/AIM46323.2023.10196241.

[89] A.C. Quillen, R.C. Nelson, H. Askari, K. Chotkowski, E. Wright, and J.K. Shang, "A lightweight vibrational motor powered recoil robot that hops rapidly across granular media," *Journal of Mechanisms and Robotics*, vol. 11, art. no. 061001, Dec. 2019. doi: 10.1115/1.4044333.

[90] B. Liu, T. Wang, D. Kerimoglu, V. Kojouharov, F.L. Hammond III, and D.I. Goldman, "Robust self-propulsion in sand using simply controlled vibrating cubes," *Frontiers in Robotics and AI*, vol. 11, pp. 1–15, Aug. 2024. doi: 10.3389/frobt.2024.1298676.

[91] S. Chen, S. Kang, Y. Gao, Y. He, C. Zhao, and L. Li, "A simple sand-skier with internal excitation," in *Proc. Int. Symposium on Intelligent Robotics and Systems (ISoIRS)*, Changsha, China, Jun. 2024, pp. 133–137. doi: 10.1109/ISoIRS63136.2024.00033.

[92] C. Hu, J. Gao, J. Diao, and X. Song, "Numerical simulation of tire steering on sandy soil based on discrete element method," *AIP Advances*, vol. 11, art. no. 015015, Jan. 2021. doi: 10.1063/5.0034585.

[93] G. Ishigami and K. Yoshida, "Steering characteristics of an exploration rover on loose soil based on all-wheel dynamics model," in *Proc. IEEE/RSJ Int. Conf. on Intelligent Robots and Systems (IROS)*, Edmonton, Canada, Sep. 2005, pp. 3099–3104. doi: 10.1109/IROS.2005.1545277.

[94] S. Moreland, K. Skonieczny, D. Wettergreen, C. Creager, and V. Asnani, "Soil motion analysis system for examining wheel-soil shearing," presented at the Proc. 17th Int. Conf. of the Int. Society for Terrain-Vehicle Systems, Blacksburg, Virginia, USA, Sep. 2011. [Online]. Available: https://www.ri.cmu.edu/pub_files/2011/9/215MorelandSkonieczny CreagerAsnaniWettergreen.pdf.

[95] S. Scheraga, A. Mohammadi, T. Kim, and S. Baek, "Design of an underactuated peristaltic robot on soft terrain," in *Proc. IEEE/RSJ Int. Conf. on Intelligent Robots and Systems (IROS)*, Las Vegas, Nevada, USA, Oct. 2020, pp. 6419–6426. doi: 10.1109/IROS45743.2020.9340978.

[96] T. Zhang and D.I. Goldman, "The effectiveness of resistive force theory in granular locomotion," *Physics of Fluids*, vol. 26, art. no. 101308, Oct. 2014. doi: 10.1063/1.4898629.

[97] C. Li, Y. Ding, N. Gravish, *et al.*, "Towards a terramechanics for bio-inspired locomotion in granular environments," in *Proc. ASCE Earth & Space Conf.*, Pasadena, California, USA, Apr. 2012, pp. 264–273. doi: 10.1061/9780784412190.031.

[98] H.C. Astley, J.R. Mendelson III, J. Dai, *et al.*, "Surprising simplicities and syntheses in limbless self-propulsion in sand," *Journal of Experimental Biology*, vol. 223, no. 5, art. no. jeb103564, Feb. 2020. doi: 10.1242/jeb.103564.

[99] X. Ma, G. Wang, K. Liu, *et al.*, "Granular resistive foce theory extension for saturated wet sand ground," *Machines*, vol. 10, art. no. 721, Aug. 2022. doi: 10.3390/machines10090721.

[100] Q. Yu, C. Pavlov, W. Kim, and A.M. Johnson, "Modeling wheeled locomotion in granular media using 3D-RFT and sand deformation," *Journal of Terramechanics*, vol. 115, art. no. 100987, May 2024. doi: 10.1016/j.jterra.2024.100987.

[101] J. Zhu, M. Zou, Y. Shen, H. Cao, Z. Chen, and Y. Qi, "3D DEM-FEM simulation of the flexible metal wheel–soil interaction in low gravity environments," *Proc. of the Institution of Mechanincal Engineers, Part C*, vol. 237, no. 6, pp. 1267–1278, 2023. doi: 10.1177/09544062221126630.

[102] J. Zhang, H. Rui, X. Ran, K. Duan, S. Wen, and J. Zhang, "Research on Simulation Method of Soft Surface Crawling Performance of Amphibious Sea Turtle Robot Based on MBD-DEM," in *Proc. 3rd Int. Symposium on Robotics, Artificial Intelligence and Information Engineering (RAIIE)*, Singapore, Singapore, Jul. 2024, pp. 26–32. doi: 10.1145/3689299.3689304.

[103] K. Gao, H. Wei, W. Xu, Z. Meng, X. Sun, and L. Sun, "Simulation and analysis of propulsive performance for screw propulsion inspection robot," *Powder Technology*, vol. 434, art. no. 119300, Feb. 2024. doi: 10.1016/j.powtec.2023.119300.

[104] A. Candalot, J. Hurrell, M.-M. Hashim, B. Hickey, M. Laine, and K. Yoshida, "Sinkage Study in Granular Material for Space Exploration Legged Robot Gripper," in *Proc. 21st Int. and 12th Asia-Pacific Regional Conf. of the ISTVS*, Yokohama, Japan, Oct. 2024, art. no. 6422. doi: 10.56884/FLURUDA3.

[105] C. Zhang, X. Wang, M. Guo, J. Zhao, and M. Li, "A compacting device of rice dry direct-seeding planter based on DEM-MFBD coupling simulation significantly improves the seedbed uniformity and seedling emergence rate," *Biosystems Engineering*, vol. 246, pp. 26–40, Oct. 2024. doi: 10.1016/j.biosystemseng.2024.07.018.

[106] K. Zhang, Y. Zhang, J. Wu, and J. Shi, "Three-dimensional MFBD-DEM coupling simulation of flexible wire mesh wheel–soil over lunar rough terrain," *Computational Particle Mechanics*, Jun. 2024. doi: 10.1007/s40571-024-00781-4.

[107] K. Zhang, J. Wu, Y. Zhang, and J. Shi, "Dust emission evaluation of the flexible metal wheel over lunar terrain and fender effect," *Mechanics Based Design of Structures and Machines*, vol. 52, no. 2, pp. 7522–7547, Jan. 2024. doi: 10.1080/15397734.2024.2303657.

[108] X. Chai, J. Hu, T. Ma, *et al.*, "Construction and Characteristic Analysis of Dynamic Stress Coupling Simulation Models for the Attitude-Adjustable Chassis of a Combine Harvester," *Agronomy*, vol. 14, no. 8, art. no. 1874, Aug. 2024. doi: 10.3390/agronomy14081874.

[109] Altair Engineering. "Multibody Dynamics Simulation." (), [Online]. Available: https://help.altair.com/hwsolvers/os/topics/solvers/os/mbd_simulation_r.htm (visited on 04/07/2025).

[110] Altair Engineering. "Couple MotionSolve with EDEM." (), [Online]. Available: https://2024.help.altair.com/2024.1/hwsolvers/ms/topics/solvers/ms/discrete_element_simulation_motionsolve.htm (visited on 04/08/2025).

[111] S. Cole. "Simulating soft soils in EDEM with the Soils Starter Pack," Altair Engineering. (Oct. 2017), [Online]. Available: https://community.altair.com/discussion/33781/simulating-soft-soils-in-edem-with-the-soils-starter-pack (visited on 04/08/2025).

[112] Altair Engineering. "The Soils Starter Pack." (), [Online]. Available: https://2024.help.altair.com/2024.1/EDEM/topics/creator_tree_bulk_material/the_soils_starter_pack_c.htm (visited on 04/08/2025).

[113] Altair Engineering. "Hertz-Mindlin (no slip) Model." (), [Online]. Available: https://2024.help.altair.com/2024.1/edem/topics/creator_tree_physics/the_hertz_mindlin_no_slip_model_r.htm (visited on 06/02/2025).

[114] Altair Engineering. "Hertz-Mindlin with JKR Model." (), [Online]. Available: https://2024.help.altair.com/2024.1/edem/topics/creator_tree_physics/the_hertz_mindlin_with_jkr_model_r.htm (visited on 06/02/2025).

[115] Altair Engineering. "Edinburgh Elasto-Plastic Adhesion Model (EEPA)." (), [Online]. Available: https://2024.help.altair.com/2024.1/edem/topics/creator_tree_physics/the_edinburgh_elasto_plastic_adhesion_model_eepa_r.htm (visited on 06/02/2025).

[116] C.J. Coetzee, "Review: Calibration of the discrete element method," *Powder Technology*, vol. 310, pp. 104–142, Apr. 2017. doi: 10.1016/j.powtec.2017.01.015.

[117] International Organization for Standardization, "Geotechnical investigation and testing — Identification and classification of soil — Part 1: Identification and description," Geneva, Switzerland, ISO 14688-1:2017, 2017.

[118] S. Lommen, M. Mohajeri, G. Lodewijks, and D. Schott, "DEM particle upscaling for large-scale bulk handling equipment and material interaction," *Powder Technology*, vol. 352, pp. 273–282, Apr. 2019. doi: 10.1016/j.powtec.2019.04.034.

[119] Altair Engineering. "Volume Packing." (), [Online]. Available: https://2024.help.altair.com/2024.1/edem/topics/creator_tree_geometries/volume_packing_t.htm (visited on 04/08/2025).

[120] AZoMaterials. "Silicone Rubber." (), [Online]. Available: https://www.azom.com/properties.aspx?ArticleID=920 (visited on 04/10/2025).

[121] S. Farah, D.G. Anderson, and R. Langer, "Physical and mechanical properties of PLA, and their functions in widespread applications — A comprehensive review," *Advanced Drug Delivery Reviews*, vol. 107, pp. 367–392, Dec. 2016. doi: 10.1016/j.addr.2016.06.012.

[122] Altair Engineering. "MV-2000: Introduction to Flexible Bodies." (), [Online]. Available: https://2024.help.altair.com/2024.1/hwsolvers/ms/topics/solvers/ms/intro_to_flex_bodies_intro_r.htm (visited on 04/10/2025).

[123] Altair Engineering. "Define Linear Periodic Boundaries." (), [Online]. Available: https://2024.help.altair.com/2024.1/EDEM/topics/creator_tree_environment/defining_linear_periodic_boundaries_t.htm (visited on 04/08/2025).

[124] Altair Engineering. "Dynamic Domain." (), [Online]. Available: https://2024.help.altair.com/2024.1/EDEM/topics/edem_simulator/using_dynamic_domain_visualization_t.htm (visited on 04/08/2025).

[125] R. Ball, "Shear strength properties of sand with fines for various moisture contents," Dissertation Bachelor of Engineering, University of Southern Queensland, Toowoomba, Queensland, Australia, Oct. 2021. [Online]. Available: https://sear.unisq.edu.au/52063/1/BALL%20Ryan%20dissertation_redacted.pdf.

[126] *How to interpret the data of maxon motors?* Maxon Motor, 2010. [Online]. Available: https://www.maxongroup.com/medias/sys_master/8798985748510.pdf (visited on 05/16/2025).

[127] *Arduino® UNO R4 WiFi*, ABX00087, Arduino, 2023. [Online]. Available: https://www.farnell.com/datasheets/3971198.pdf (visited on 04/25/2025).

[128] *Gear Motor with Encoder*, FIT0186, DFRobot. [Online]. Available: https://www.farnell.com/datasheets/3708829.pdf (visited on 04/25/2025).

[129] *Dual DC motor driver*, DRI0041, DFRobot. [Online]. Available: https://www.farnell.com/datasheets/3708793.pdf (visited on 04/25/2025).

[130] *3 V to 24 V Input, 24 A microBUCK® DC/DC Converter*, SiC431, Vishay Siliconix. [Online]. Available: https://www.farnell.com/datasheets/3205191.pdf (visited on 04/25/2025).

[131] *Red Power LiPo accupack 14.8 V 5000 mAh 35 C Softcase XT90*, 19125, Conrad. [Online]. Available: https://www.conrad.nl/nl/p/red-power-lipo-accupack-14-8-v-5000-mah-35-c-softcase-xt90-3385538.html (visited on 04/25/2025).

[132] *MINI® Blade Fuses Rated 32V*, Littelfuse. [Online]. Available: https://www.farnell.com/datasheets/3741304.pdf (visited on 04/25/2025).

[133] *15A, 20V - 40V Schottky Barrier Rectifier*, SR1502 - SR1504, Taiwan Semiconductor. [Online]. Available: https://4donline.ihs.com/images/VipMasterIC/IC/TWSC/TWSC-S-A0013599748/TWSC-S-A0013599903-1.pdf?hkey=6D3A4C79FDBF58556ACFDE234799DDF0 (visited on 04/25/2025).

[134] *6 mm Koperen Inbus Montage*, 18059, RobotShop. [Online]. Available: https://eu.robotshop.com/nl/products/6-mm-koperen-inbus-montage (visited on 04/25/2025).

Appendix A

Silicone Molding Process

The soft, inflatable part of the wheel is made from silicone rubber. The silicone part is constructed by molding the silicone rubber using a 3D-printed mold. The main part of the mold is shown in Figure A.1. This part also contains the mold of the air inlet, which will be a small, silicone tube. The main part of the mold will be filled with silicone rubber. All molds have been sprayed with a mold release agent to ensure easy removal of the silicone part from the mold. The first cover (Figure A.2a) will be placed on top of the main part, creating the bottom and sides of the silicone part (Figure A.2b). After the curing time has elapsed, the first part of the mold can be removed. The silicone part created after the first molding step is shown in Figure A.3. The bottom, top, and sides of the silicone part all have a thickness of 3 mm. The surfaces to be inflated between the lugs are 2 mm thick, as indicated in Figure A.3a. The hexagon ring in the centre of the silicone part is 4 mm thick. The second cover of the mold is used to close the silicone structure, creating a hollow, soft, inflatable structure. The second cover (Figure A.4a) of the mold is filled with silicone rubber and the main part of the mold is placed on top of the second cover (Figure A.4b). After the curing time has elapsed, the silicone part can be removed from the mold and can be assembled into the wheel.

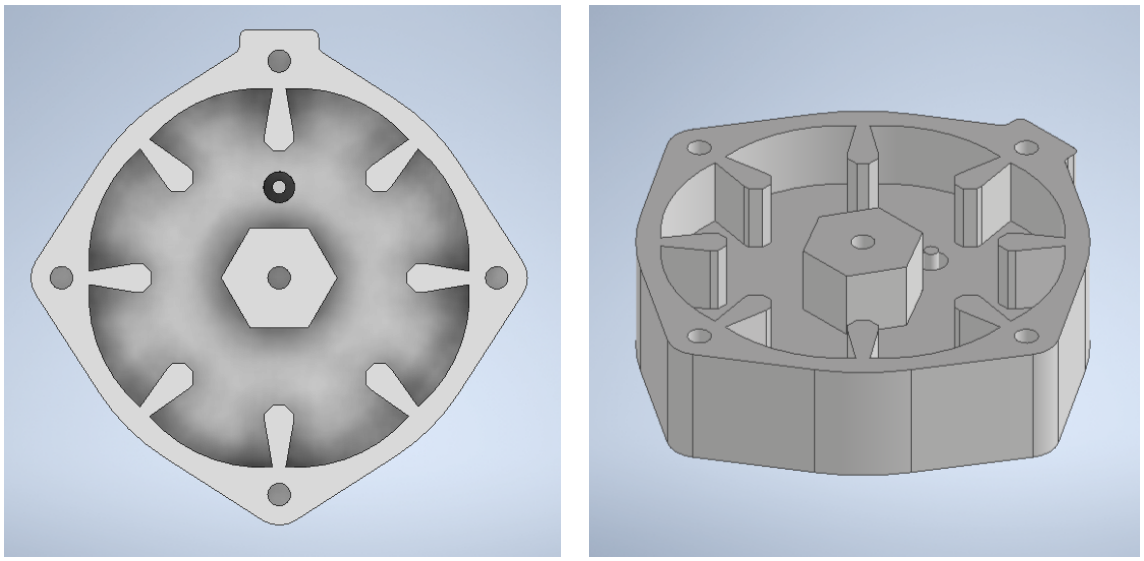

(a) top view (b) isometric view

Figure A.1: The main part of the silicone mold.

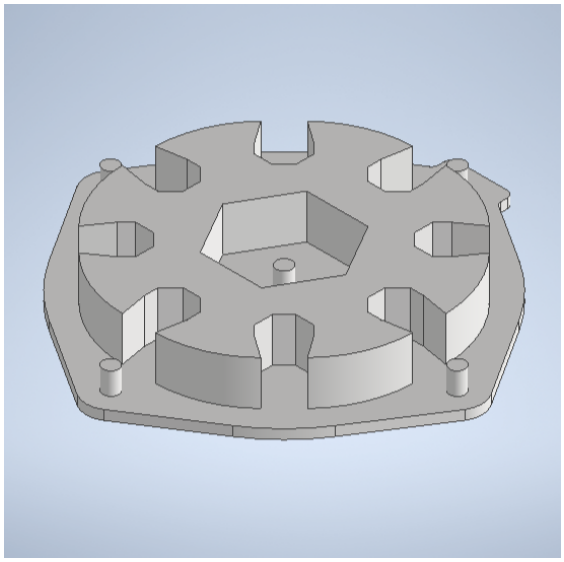

(a) isometric view of cover 1

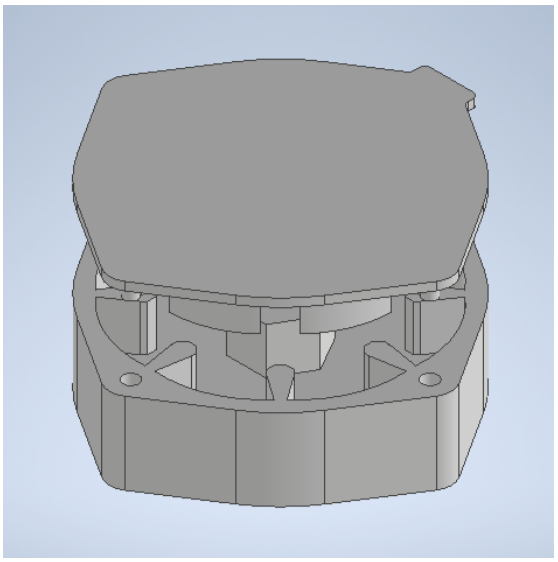

(b) cover 1 placed on top of the main part

Figure A.2: Overview of the first step of the silicone molding process.

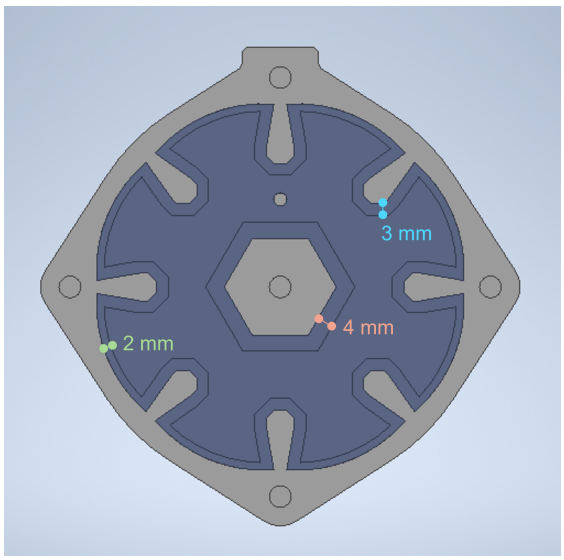

(a) top isometric view

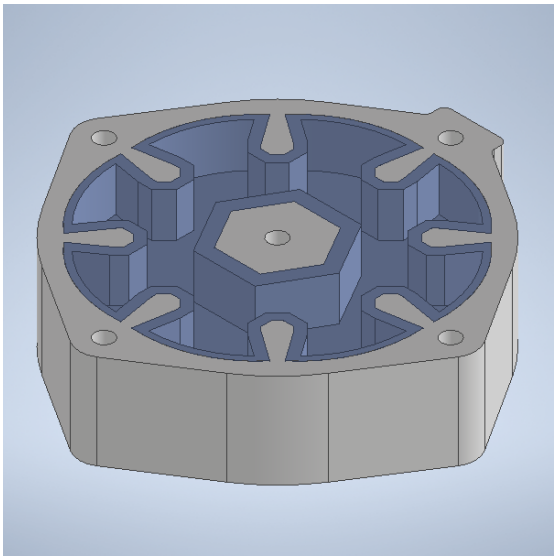

(b) bottom isometric view

Figure A.3: Overview of the silicone part after the first molding step.

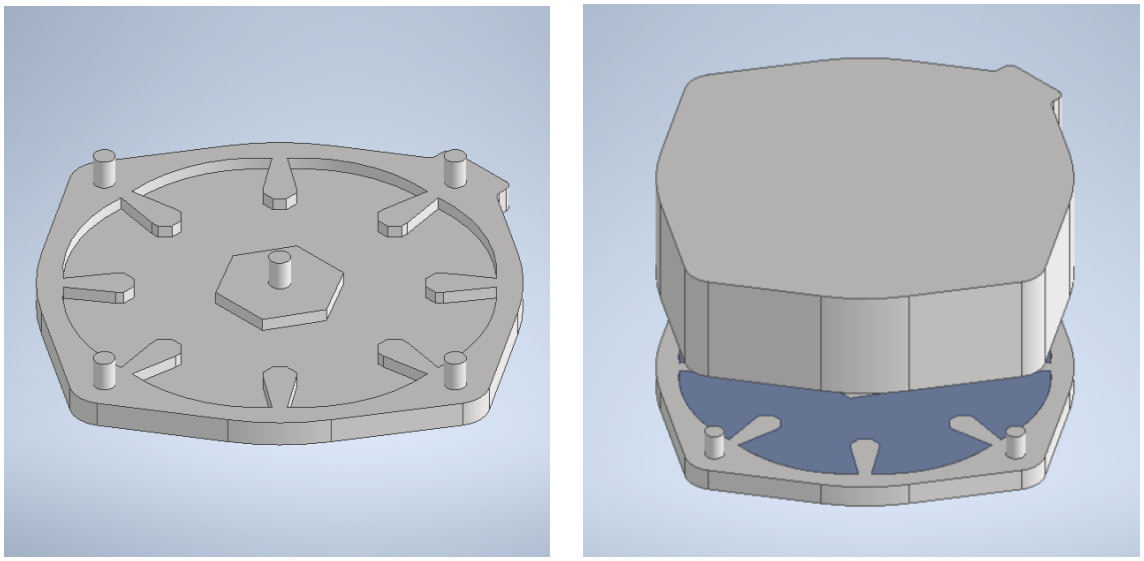

(a) isometric view of cover 2

(b) main part placed on top of cover 2

Figure A.4: Overview of the second step of the silicone molding process.

Appendix B

Prototype Part List

This appendix shows all the parts of the prototype. The 3D-printed structural parts of the robot are also included. The CAD models of these parts are included to illustrate their design. For the actuation and electronic components a list of important specifications and references is included. Lastly, Table B.2 shows the required fasteners and Table B.1 provides an overview of the prototype's weight. Figure B.1 shows the location of the centre of gravity (COG) of the prototype.

Table B.1: Overview of the weight of the prototype.

component	quantity	weight per pc. (g)	total weight (g)
chassis	1	160	160
wheel hub	4	35	140
wheel cover	4	20	80
silicone inflatable part	4	80	320
battery cover	1	20	20
motor bracket	4	5	20
DC/DC converter support	2	15	30
Arduino	1	35	35
DC motor	4	205	820
Motor driver	2	32	64
DC/DC converter	2	33	66
Battery	1	427	427
Fuse	2	0.57	1
Diode	4	1.70	7
Motor coupling nut	4	14	56
Fasteners	-	-	184
		total prototype weight	2430

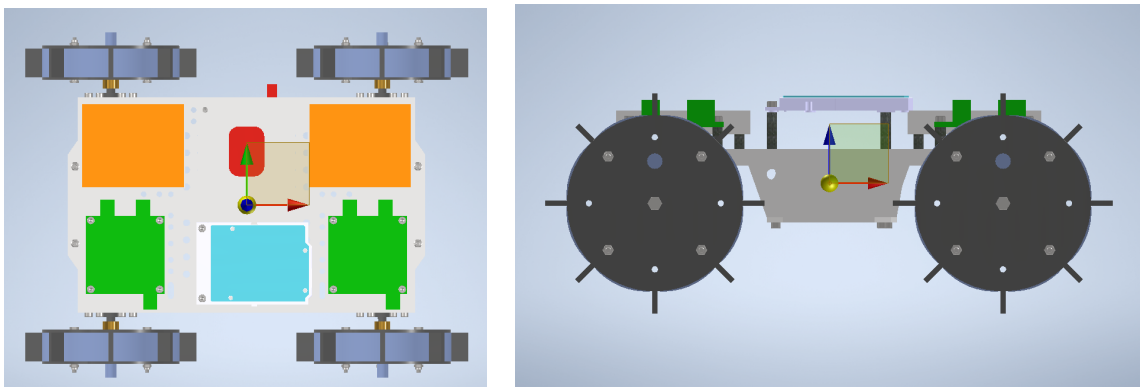

(a) top view (b) side view

Figure B.1: Location of the COG of the prototype.

Chassis

- Fabrication method: 3D-printed
- Material: PLA
- Quantity: 1
- Weight: $\pm$ 160 g

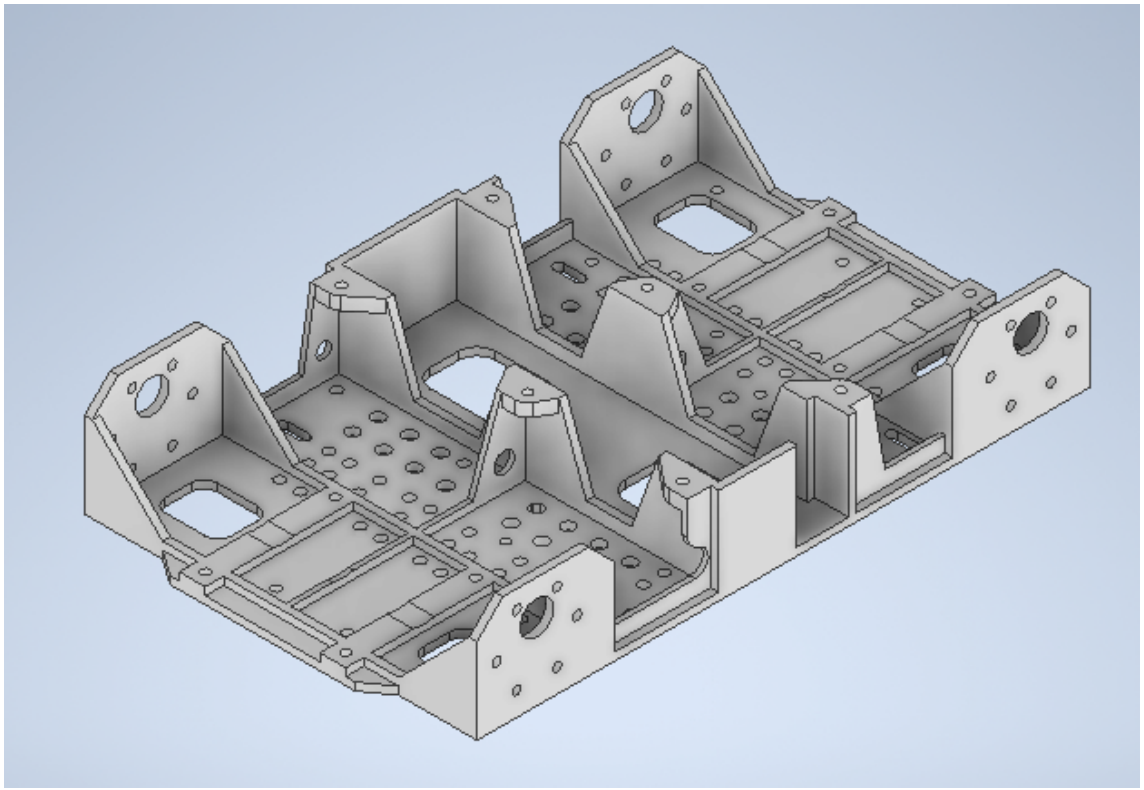

Figure B.2: CAD model of the chassis.

Wheel hub

- Fabrication method: 3D-printed
- Material: PLA

- Quantity: 4
- Weight: $\pm$ 35 g

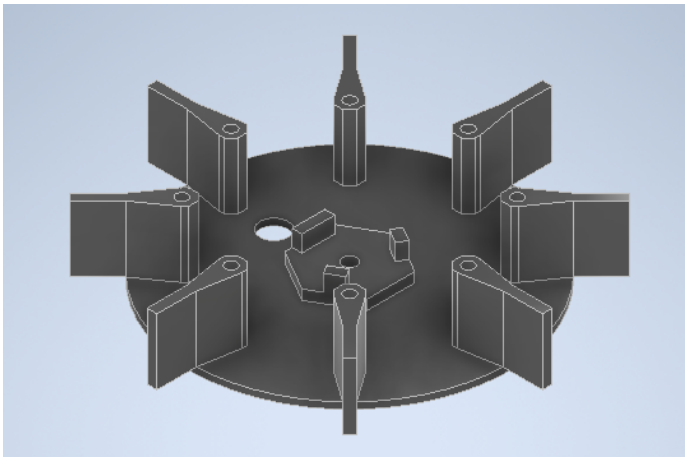

Figure B.3: CAD model of the wheel hub.

Wheel cover

- Fabrication method: 3D-printed
- Material: PLA
- Quantity: 4
- Weight: $\pm$ 20 g

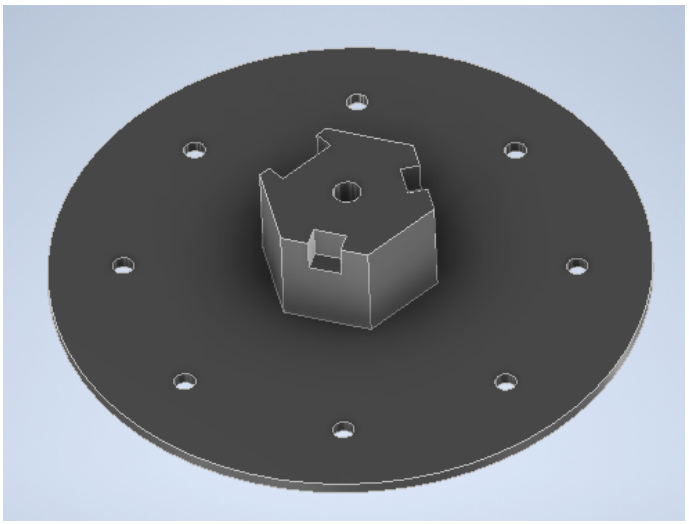

Figure B.4: CAD model of the wheel cover.

Silicone inflatable part

- Fabrication method: molded
- Material: Ecoflex^{TM} 00-50
- Quantity: 4
- Weight: $\pm$ 80 g

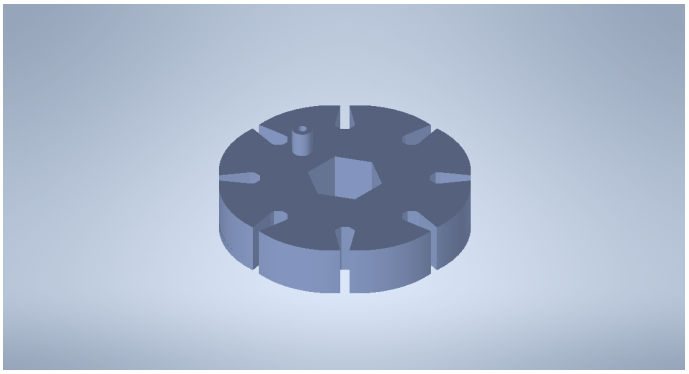

Figure B.5: CAD model of the silicone inflatable part.

Battery cover

- Fabrication method: 3D-printed
- Material: PLA
- Quantity: 1
- Weight: $\pm$ 20 g

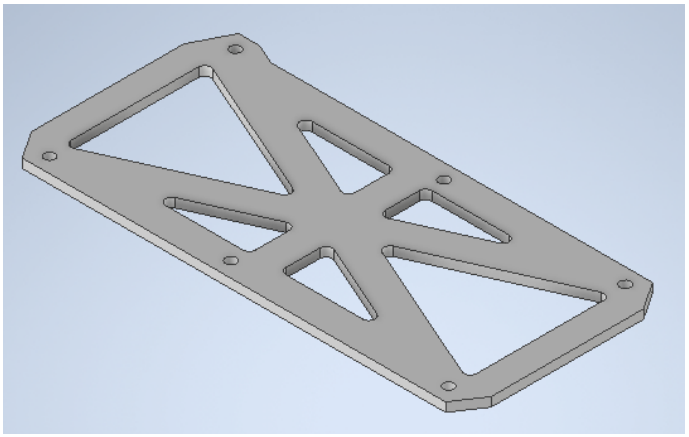

Figure B.6: CAD model of the battery cover.

Motor bracket

- Fabrication method: 3D-printed
- Material: PLA
- Quantity: 4
- Weight: $\pm$ 5 g

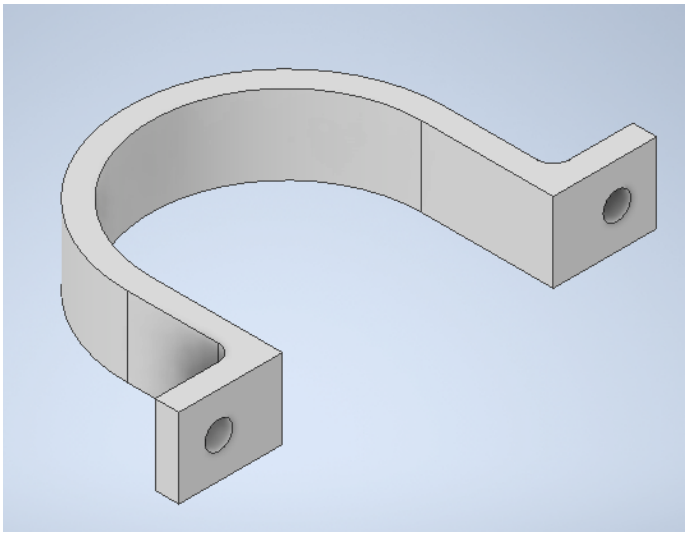

Figure B.7: CAD model of the motor bracket.

DC/DC converter support

- Fabrication method: 3D-printed
- Material: PLA
- Quantity: 2
- Weight: $\pm$ 15 g

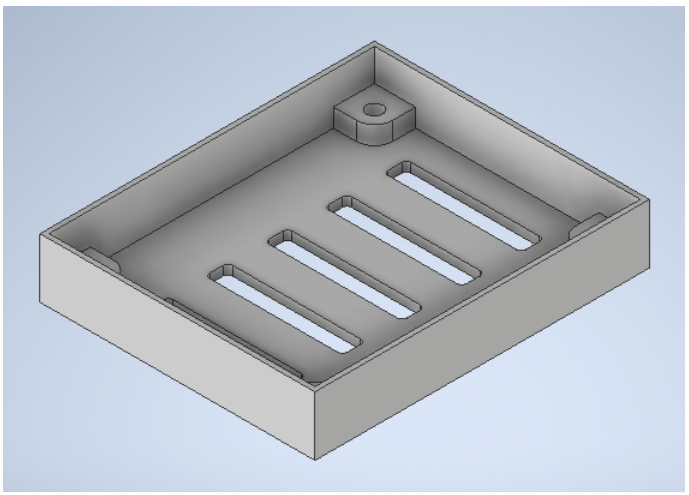

Figure B.8: CAD model of the DC/DC converter support.

Arduino Uno R4 WIFI [127]

- Manufacturer: Arduino
- Type number: ABX00087
- Variant: R4
- WIFI compatible
- Power via USB-C at 5 V
- Number of PWM pins: 6

- Quantity: 1
- Weight: 35 g

Metal DC geared motor with encoder [128]

- Manufacturer: DFRobot
- Type number: FIT0186
- Motor operating voltage: 12 V
- Gear ratio: 43.8:1
- No-load speed: 251 RPM
- No-load current: 350 mA
- Stall torque: 1.77 Nm
- Stall current: 7 A
- Diameter motor shaft: 6 mm
- Encoder type: Hall
- Encoder operating voltage: 5 V
- Encoder resolution: 16 CPR (motor shaft)/700 CPR (gearbox shaft)
- Quantity: 4
- Weight: 205 g

Dual DC motor driver [129]

- Manufacturer: DFRobot
- Type number: DRI0041
- Number of output channels: 2
- Input voltage: 7-24 V DC
- Maximum continuous operating current per channel: 7 A
- Peak current: 50 A
- Speed control: PWM
- Quantity: 2
- Weight: 32 g

Synchronous buck DC/DC converter [130]

- Manufacturer: Vishay Siliconix
- Type number: SIC431AEVB-A
- Input voltage: 3-24 V DC
- Output voltage: adjustable down to 0.6 V
- Maximum continuous current: 24 A
- Quantity: 2
- Weight: 33 g

LiPo accupack [131]

- Manufacturer: Red Power
- Type number: 19125
- Battery technology: LiPo
- Voltage: 14.8 V
- Capacity: 5000 mAh
- C-rate: 35 C
- Connector system: XT90
- Balancer plug-in: XH
- Quantity: 1
- Weight: 427 g

Fuse [132]

- Manufacturer: Littelfuse
- Type number: 0297020.WXNV
- Voltage rating: 32 V
- Current rating: 20 A
- Blow characteristic: fast acting
- Quantity: 2
- Weight: 0.57 g

Diode [133]

- Manufacturer: Taiwan Semiconductor
- Type number: SR1504
- Repetitive peak reverse voltage: 40 V
- Forward current: 15 A
- Diode case style: axial leaded
- Quantity: 4
- Weight: 1.70 g

Motor coupling nut [134]

- Manufacturer: Nexus Robot
- Type number: 18059
- Diameter motor shaft: 6 mm
- Nut size: 12 mm
- Threaded hole: M4
- Quantity: 4
- Weight: 14 g

Fasteners

Table B.2: Overview of the required fasteners for the prototype.

fastener type	size	quantity	weight per pc. (g)	total weight (g)
DIN 933 hex-head bolt	M4x16	4	2	8
DIN 933 hex-head bolt	M3x30	16	2	32
DIN 912 cylinder head cap screw	M3x12	14	1	14
DIN 912 cylinder head cap screw	M3x10	8	1	8
DIN 912 cylinder head cap screw	M3x6	56	1	56
DIN 985 hex lock nut	M3	30	1	30
hex spacer nut	M3x8	8	1	8
hex spacer nut	M3x12	8	2	16
hex spacer nut	M3x20	4	3	12
			total fastener weight	184

Appendix C

Low Damping Simulation Results

This appendix presents the results of the prototype locomotion simulations with a low value for the damping of the bushings. The initial translational and rotational damping of the bushings was set to 5 N·s/m and 5 N·m·s/rad, respectively, and the results of those simulations are presented in Table C.1. No results are available for the locomotion simulations on loose, dry sand, as these simulations were not stable for these low damping values. Additionally, only the results for the inflated robot configurations are presented, as damping is not applicable for the simulations of the deflated configurations.

Table C.1: Overview of the results of the prototype locomotion simulations for the initial low damping values of the bushings.

simulation case	configuration	granular soil type	static sinkage (mm)	total distance travelled (mm)
slope	inflated	dry sand	-	-
slope	inflated	wet sand	6	1174
slope	inflated	very wet sand	8	1130
obstacle	inflated	dry sand	-	-
obstacle	inflated	wet sand	6	1234
obstacle	inflated	very wet sand	8	1197

Appendix D

Scientific Research Paper

The research paper begins on the next page.

Reinventing the Wheel: A Simulation-Aided Design of a Soft, Shape-Adapting, Lugged Wheel for Locomotion on Sandy Terrains

P. Klaassen[a], H. Shi[a], J. Jovanova[a,*]

[a]*Department of Maritime and Transport Technology, Faculty of Mechanical Engineering, Delft University of Technology, 2628 CD, Delft, The Netherlands*

Abstract

Locomotion over granular terrain poses significant challenges for autonomous robotic systems, particularly in coastal regions characterized by loose, shifting sands. This paper presents a simulation-aided design approach to develop a soft, shape-adapting, wheeled locomotion system optimized for sandy terrains. A co-simulation framework combining the discrete element method (DEM) and multibody dynamics (MBD) is employed to simulate the locomotion of a wheeled robot on varying sandy soils, covering both dry and wet sandy soil conditions. A shape-adapting wheel design is proposed, incorporating soft, inflatable elements that enable the wheel to transform between lugged and circular configurations. A discretized flexbody approach is proposed to model the interactions between the sandy soil and the soft, flexible bodies of the shape-adapting wheel design. Simulation results demonstrate improved performance of the shape-adapting wheels across a variety of sandy terrains, including slopes and obstacles. Integrating softness into the wheel improves obstacle climbing performance, while a lugged wheel configuration performs particularly well on loose, dry sandy slopes. The DEM-MBD co-simulation enables efficient evaluation of locomotion strategies without the need for extensive physical prototyping.

Keywords: DEM, shape-adapting wheel, granular terrain, locomotion, simulation-aided design

1. Introduction

Locomotion on granular terrain has been a long-standing challenge in both space exploration and terrestrial applications. One of the most iconic examples is the Moon, where lunar soil poses significant difficulties for robotic mobility due to its fine, loosely packed particles. On Earth, desert environments, agricultural fields, and coastal regions represent key examples where robots must navigate loose and shifting substrates. Among these, coastal regions are especially significant. They serve as critical interfaces between land and sea, hosting a wide range of ecosystems, supporting major economic activities and providing habitat for over 40% of the world's population [1]. Globally, approximately 31% of all coastlines are sandy [2], while in the Netherlands approximately 75% of all coastlines consist of sandy beaches and dunes [3].

The exploration and monitoring of these sandy coastal zones have gained importance in a variety of fields, including maintenance and inspection of coastal structures, environmental monitoring and search-and-rescue operations. These tasks are conducted in areas that are difficult or dangerous for humans to access, making autonomous robotic systems a valuable tool. Ensuring that robots can avoid getting immobilized is a critical factor in making autonomous operations practical and safe in these challenging sandy terrains. When sand is compressed under the weight of the robot, the grains lock together and resist deformation. In this state the sand behaves like a solid, offering support and enabling traction. When sand is disturbed by movement of the robot, the grains lose contact and start flowing. In this state the sand behaves like a fluid, offering little resistance and allowing objects to sink into the sand [4, 5]. This unpredictable response of sandy soils or the presence of natural obstacles such as rocks, vegetation and slopes can lead to mission failure, especially if the robot becomes immobilized in the sandy terrain.

Robots use various strategies for locomotion on granular terrain. Robotic systems can be classified into six different categories: legged, wheeled, tracked, screw-based, undulatory and vibration-based locomotion, where legged and wheeled locomotion are the most commonly used strategies. Wheeled locomotion strategies are also combined with other locomotion strategies, to create improved systems. The so-called wheel-leg systems combine wheeled locomotion with legged locomotion [6, 7, 8], where the wheel is attached at the end of the leg. Wheg designs, which are wheel-like structures with multiple spokes or legs, also combine wheeled locomotion with legged locomotion [9, 10, 11]. Wheels with a wave-like surface combine wheeled locomotion with undulatory locomotion [12, 13] and wheel designs with a helical surface combine wheeled locomotion with screw-based locomotion [14, 15]. Various adaptable wheels have also already been developed, such as wheels with a variable diameter [16] or extendable lugs [17]. Soft robotic locomotion systems have been developed for legged [18], snake-like [19] or vibration-based [20] locomotion systems.

Evaluating the performance of different locomotion systems can be achieved through simulations, eliminating the need for physical prototyping. Therefore, developing a simula-

tion framework to model interactions between robotic structures and sandy terrains is essential for assessing the effectiveness of various design configurations. These interactions are often modelled with terramechanics-based models. Those terramechanics-based models are continuum-based models, which model the granular soil as a continuous medium and rely on empirical relations [21]. The use of discrete element method (DEM) modelling remains a relatively unexplored approach for evaluating robotic locomotion on sandy terrains. DEM is a numerical, particle-based modelling approach, which represents the granular soil as a finite number of discrete particles, each governed by Newton's laws of motion [22]. The interactions between particles, such as collisions, friction or bonding, are explicitly modelled using contact models, which account for normal and tangential forces, damping and sometimes cohesion. By coupling DEM with multibody dynamics (MBD) simulations, both the robot's motion and the granular terrain's behaviour can be accurately captured [23, 24]. To model soft, flexible robotic structures, DEM is coupled with multi-flexible-body dynamics (MFBD) simulations, where the DEM part is simulating the granular material and the MFBD part is another co-simulation of MBD and FEM [25, 26]. These types of models would require significant computational power.

Coupling DEM with MBD simulations provides a powerful approach for assessing robotic locomotion on sandy terrains. To fully leverage this framework, it is also necessary to model soft and flexible robotic systems. Incorporating softness into the robot design can enhance its ability to traverse obstacles and adapt to varying terrain conditions. The integration of soft robotic systems with wheeled locomotion offers a promising balance between adaptability and efficiency. The added flexibility allows the robot to better tackle unstructured terrains, while the wheeled mechanism ensures effective movement across longer distances. Therefore, the aim of this paper is to develop a simulation framework, which can be used to support the design of a soft, wheeled locomotion system for sandy terrains. The soft, wheeled locomotion system enables adaptation to varying terrain conditions and potential obstacles. Incorporating a co-simulation of DEM and MBD enables the evaluation of robotic performance on a variety of sandy terrains, including dry and wet sands commonly found in coastal environments.

Section 2 first presents the simulation framework used to evaluate the performance of robotic locomotion systems. Section 3 presents the design methodology to clarify how simulations are used in the design process. The resulting design of the soft, wheeled locomotion system is presented in Section 4. The performance of the final prototype design is evaluated with simulations, as explained in Section 5. Section 6 presents the conclusions of this paper and gives some recommendations for future research.

2. Simulation Framework

A coupled simulation of DEM and MBD is used to simulate the locomotion of a robot on sandy terrains. Altair EDEM is the used DEM simulation software and Altair MotionView/MotionSolve is the used MBD simulation software. The DEM simulation models the granular material and its interactions with equipment. DEM is a numerical modelling approach used to simulate the behaviour of granular materials. DEM represents the granular soil as a finite number of discrete particles, each governed by Newton's laws of motion. The interactions between particles, such as collisions, friction or bonding, are explicitly modelled using contact models. These contact models account for normal and tangential forces, damping and sometimes cohesion [22, 27]. The typical contact model used in DEM is shown in Figure 1. The particle-particle interactions are resolved using a spring-damping system in both normal and tangential direction. The normal and tangential component both include a spring-damper system with stiffness K and damping D, which models how particles resist compression and dissipate energy during collisions. The tangential force computed from the spring damper system is limited by the Coulomb friction law, where the maximum resistive tangential force is determined by the value of the friction coefficient μ.

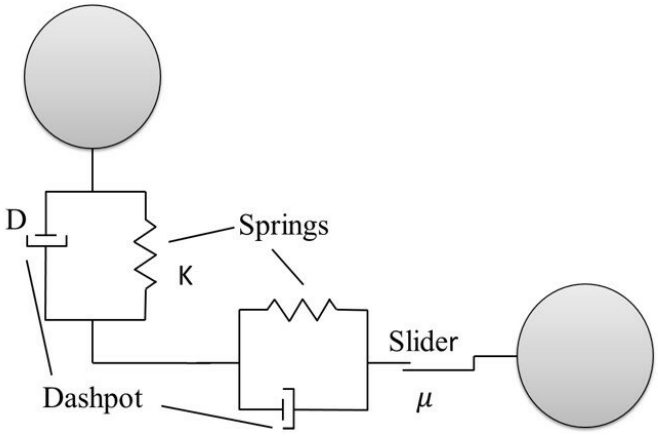

Figure 1: Schematic of the typical contact model used in DEM [28].

The multibody dynamics (MBD) simulation predicts the robot's motion based on the interacting forces and system constraints. A multibody system refers to a collection of interconnected bodies. The bodies in the simulation can be rigid or flexible. A transient analysis is performed to determine how the system responds to loads and movements that change over time. The system responses are displacements, velocities, accelerations and forces, which are calculated using the equations of motion [29]. Both simulations will run in separate processes, but there is bi-directional communication between the DEM and MBD software. The MBD software will provide at each timestep the positions and velocities of the interacting bodies and EDEM returns the forces exerted by the granular material on the interacting bodies.

The MBD model of the robot consists of one rigid chassis body and 4 wheels. Each wheel consists of a rigid wheel hub and a certain number of soft, flexible elements, depending on the wheel design. The rigid wheels are constrained to the chassis body with four revolute joints in the centre of each wheel, which is shown in Figure 2. The motion is applied at each of

the four joints, resulting in four-wheel-drive. The type of motion applied to the joints can vary from angular speed, angular acceleration or torque, depending on the goal of the simulation. The chassis of the robot is modelled as a solid body, where it is in reality a shell body with a certain thickness. The extra weight of the solid body compensates for the weight of all the actuation and electronic parts. The timestep of the DEM simulation should be set to a fixed value to ensure that the timestep of the DEM simulation is an exact multiple of the communication interval of the MBD simulation. The fixed value of the timestep in the DEM simulation is set to a value of 2.0e-05 or 2.5e-05 seconds, corresponding to a Rayleigh percentage of approximately 18%, which is suitable for most of the simulations. However, for the inflated configurations on the loose, dry sand, a lower timestep of 7.0e-06 seconds (≈5%) is used to ensure simulation stability. All simulations are performed by using an Intel® Core™ i7-8750H CPU with 12 cores and a clock speed of 2.20 GHz.

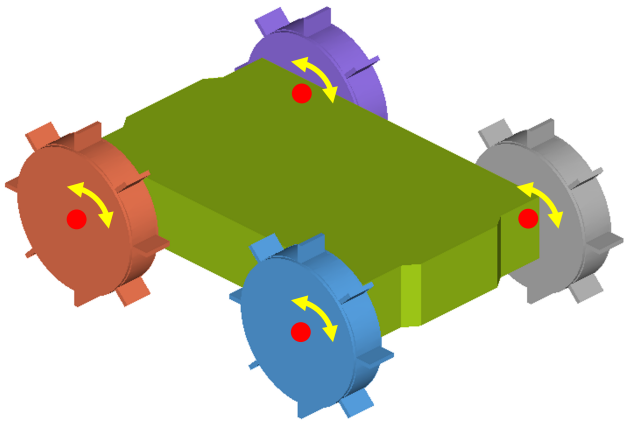

Figure 2: Simulation model of the robot with a rigid chassis and 4 rigid wheel bodies.

The next subsection explains the granular, sandy soils that have been used for the simulations. The input parameters related to the materials of the robot bodies for both the DEM and MBD simulations are given in Section 2.2. The modelling of the soft, flexible bodies is explained in Section 2.3.

2.1. Sandy Soils

Three different sandy soils have been selected, where each soil varies in moisture content. These granular soils are selected from the Soils Starter Pack of Altair EDEM [30]. The non-compressible dry soil is selected for representing dry sand and the non-compressible sticky soil is selected for representing wet sand. The compressible, sticky soils is selected to represent very wet sand or clay. The input parameters of the three sandy soil types are obtained from [31] and are given in Table 1. The associated contact model is also given in Table 1. The moisture content is represented by the cohesion of the soil, which is modelled by the surface energy. Compressibility of the soil is modelled via the plasticity ratio, applicable only to the compressible, sticky, very wet sand.

Only spherical particles are used to model the sandy soils, which minimizes the computational costs [35]. The size of the sand particles is upscaled to bigger particles of 3 mm, because modelling the sand particles with a realistic size of 0.063-2.0 mm [36] would be too computational expensive. Increasing the particle size by a factor of 1.5 doesn't influence the main behaviour of the granular material [37]. A particle size of 2 mm has also been considered, but the number of particles would then be around 700000. When using a 3 mm particle size, the number of particles is around 200.000, which is way better in terms of computational time. A simple locomotion simulation would take approximately 1.5 hours for 3 mm particles and 8.5 hours for 2 mm particles.

2.2. Equipment Materials

Other input parameters for the DEM simulations are related to the interactions between the equipment materials and the granular material or obstacle. The material properties of the equipment materials and the interaction parameters are all given in Table 2. The robot is designed using two different materials. The soft, flexible parts of the robot are made from silicone rubber. The material properties of standard silicone rubber [38] are used, as the values of the exact silicone rubber material are unknown. The rigid parts of the robot are all 3D-printed from polylactic acid (PLA), which material properties are obtained from [39]. The interaction properties between the rigid bodies of PLA and the granular soil are set to the default values of Altair EDEM (see Table 2), as these values are hard to find for the specific interactions between sandy soils and PLA. The interaction properties between the silicone soft parts of the robot and the granular soil are obtained from a study on tyre steering on sandy soils [40].

For the simulations with the obstacle, a contact is defined between the wheel bodies and the obstacle. The Poisson model is used to model the normal force of the contacts. The penalty of the normal force is set to a high value to reduce the penetration between the bodies and the coefficient of restitution is set to a low value to limit the bouncing (see Table 2). The friction values are set to the same values as for the friction between the particles and the equipment materials.

2.3. Discretized Flexbody Representation

Modelling the soft, flexible bodies as a finite element model would be too costly in terms of computational time. A more computational efficient method is the component mode synthesis (CMS) technique [41]. This technique reduces the degrees of freedom of the flexible body to a smaller set of modes. The computational time for CMS flexible bodies is significantly lower than that of full FEM simulations due to the reduced number of DOFs. However, CMS flexible bodies are only suitable for linear systems, so the deformations of the flexible body have to be small. Therefore, modelling the soft, flexible elements with a modal representation is only used for simulations to roughly evaluate the performance of a certain design.

Performing a co-simulation of DEM and MBD with flexible bodies with non-linear behaviour and large deformations is difficult to achieve. Therefore, a simplified approach is used to

Table 1: Input parameters of the three different sandy soils.

parameters	non-compressible dry sand	non-compressible, sticky, wet sand	compressible, sticky, very wet sand/clay
contact model	Hertz-Mindlin [32]	Hertz-Mindlin + JKR [33]	EEPA [34]
Poisson's ratio v	0.25	0.25	0.25
density ρ (kg/m^3)	2.6	2.6	2.6
shear modulus G (MPa)	10	10	10
co. of restitution e	0.55	0.55	0.55
co. of static friction μ_s	0.2	0.2	0.2
co. of rolling friction μ_r	0.1	0.1	0.1
surface energy γ_s (J/m^2)	-	3.75	50
contact plasticity ratio λ_p	-	-	0.7

Table 2: Input parameters for the equipment materials and their interactions with the granular material and the obstacle.

parameters	silicone rubber	polylactic acid (PLA)
Poisson's ratio v_g	0.47	0.36
density ρ_g (kg/m^3)	1100	1250
shear modulus G_g (MPa)	20	1287
co. of restitution e_g	0.48	0.5
co. of static friction μ_{sg}	0.55	0.5
co. of rolling friction μ_{rg}	0.37	0.01
normal force penalty	500000	500000
normal force co. of restitution	0.1	0.1

model the behaviour of the soft, flexible bodies in a more realistic way. These flexible bodies are discretized in multiple smaller bodies, which are connected with bushings to create a chain of bodies (Figure 3). Each small body is also connected to the centre of the wheel with a linear spring-damper, which represents the stiffness of the flexible body. This chain of small bodies can behave like a flexible body and it can undergo large deformations if the spring stiffness is low. In this case the chain of bodies consist of five different bodies to minimize the computational time. The number of bodies will determine the computational time of the simulation, as each extra body will also add an extra bushing and an extra spring-damper. An odd number of bodies is chosen so that the highest point, where initial contact with the surface occurs, is located at the centre of a body rather than at a connection point.

Eight different input parameters are required for the discretized flexbody representation. The bushings require translational and rotational stiffness values in all three directions, as well as corresponding translational and rotational damping values. Additionally, stiffness and damping coefficients have to be assigned for the spring-dampers. These parameters have been obtained by comparing the behaviour in simulations with the behaviour of the physical prototype (see Figure 4), when moving over a small obstacle of 15 mm high and 30 mm wide. The parameter set that produces the closest match to the observed behaviour was selected and is given in Table 3. The stiffness of the whole chain of discrete bodies is not solely dependent on the spring stiffness. The stiffness of the bushings is also playing a significant role and is set to relatively high values, which is required to achieve stable simulations. Low stiffness values would result in high deformations, which would require a smaller timestep to model those deformations. The damping values are also set to high values to reduce the bouncing in the simulation, which enables stable simulations for a higher timestep, and therefore minimizing the computational time.

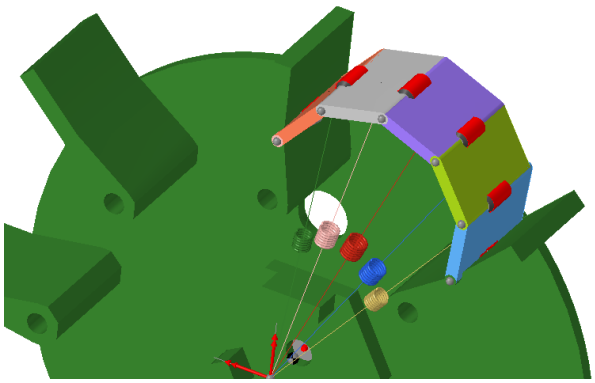

Figure 3: One section of the discretized flexbody representation.

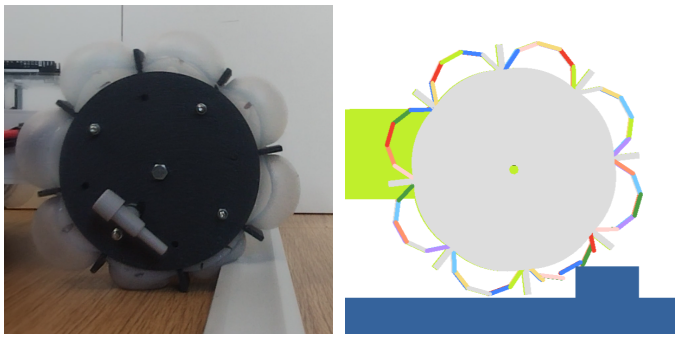

(a) physical prototype (b) simulated prototype

Figure 4: Comparison of the prototype and simulation at a key moment during traversal of a 15 mm high, 30 mm wide obstacle.

A limitation of this discretized flexbody representation is the ability to model deformation only in 2 directions. It is not possible to model the deformation of the soft, flexible bodies in the direction parallel to the wheel axis. Deformation in this direction is not desired for this design, so this limitation does not influence the simulation results. An additional disadvantage occurs when using these discretized flexbodies in DEM simulations with small particles. Those particles can go between the rigid wheel and the chain of discrete bodies, which can influence the results and the stability of the simulation. This is solved by decreasing the timestep for loose granular soils to ensure stable simulations. The construction of the simulation model is quite complex. Each body in the chain of discrete bodies must be imported individually into the simulation environment, and the bushings and spring-damper elements must be added and configured manually. As a result, any change in the design requires the construction of an entirely new simulation model from scratch. This low adaptability is not a concern for this research, as this method will only be used to evaluate the performance of one final design configuration.

Table 3: Input parameters for the discretized flexbody representation.

simulation parameter	setting
bushing translational stiffness (X,Y,Z)	1000 N/m
bushing rotational stiffness (X,Y,Z)	1000 N·m/rad
bushing translational damping (X,Y,Z)	15 N·s/m
bushing rotational damping (X,Y,Z)	15 N·m·s/rad
spring stiffness #1 & #5	15 N/m
spring stiffness #2 & #4	11 N/m
spring stiffness #3	7 N/m
spring damping	10 N·s/m

3. Design Methodology

The design methodology of developing a soft, wheeled locomotion method is presented schematically in Figure 5. The design process is supported with simulations. These simulations are used to evaluate the performance of different design configurations. The first design step is the concept design. Several concepts are developed to solve the design problem of the locomotion of soft, wheeled structures on sandy soils. The performance of the designed concepts is evaluated with locomotion simulations, where the soft, flexible bodies are represented with the modal flexbody representation. This modal flexbody representation has low computational cost, resulting in the ability to quickly assess the performance of different concept designs.

The selected concept is developed further into the design of a prototype. Several locomotion simulations are conducted to optimize the design of the wheels and the prototype, which is explained in more detail in the following subsections.

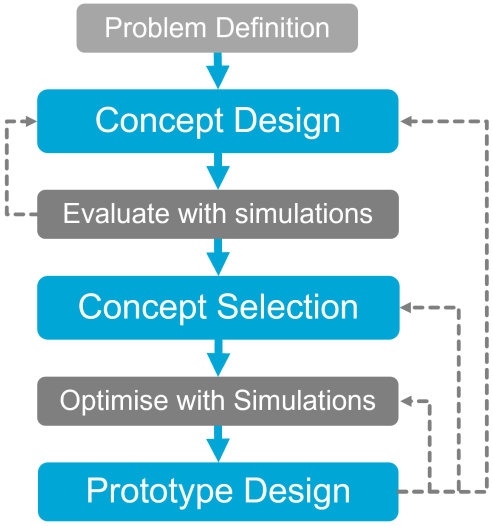

Figure 5: Schematic overview of the design methodology.

3.1. Wheel Design Optimization

Five different wheel parameters can be varied to create the optimal wheel design for locomotion on sandy soils: wheel thickness, wheel diameter, lug length, lug thickness and lug spacing.

The wheel diameter is indicated with the blue arrow in Figure 6, and is an important parameter for the performance of the robot. Bigger wheels means a larger travelling distance for the same speed. A minimum wheel diameter is required to maintain sufficient body clearance and prevent the robot from becoming stuck on an obstacle or from dragging its body on the ground. The body clearance of the robot is the distance between the soil and the bottom of the chassis and is indicated with the yellow arrow in Figure 6. So, the wheel diameter is based on this body clearance and the size of the robot.

The wheel thickness is not indicated in Figure 6, but corresponds to the width of the wheel in lateral direction, perpendicular to the direction of travel. Thicker wheels provide a larger contact area with the ground, resulting in increased friction and improved stability. However, thicker wheels also increase the weight of the robot and therefore influence the performance, especially on slopes. For steep slopes, thinner wheels have better performance due to their lower weight. On small slopes,

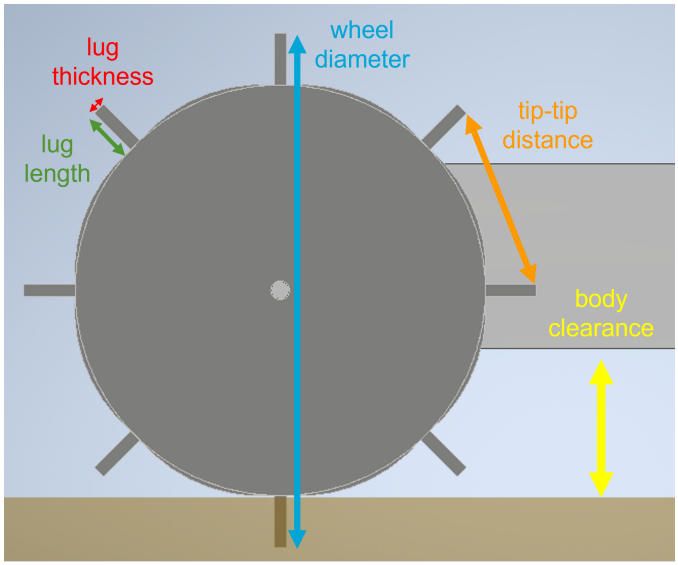

Figure 6: Schematic of the wheel parameters and the robot's body clearance.

thicker wheels have better performance, as they can generate more traction [42]. Therefore, the wheel thickness is based on the size and weight of the robot.

The lug length is indicated with the green arrow in Figure 6 and is the distance from the top of the lug to the top of the soft body in deflated configuration. Increasing the lug length increases the travelling performance of the robot [43, 42]. However, the lug length is also determined by the design of the inflatable elements. When inflated, these elements should protrude beyond the wheel's surface, meaning the lug length must be less than or equal to the maximum extension achieved through inflation. The soft, inflatable elements will be made of silicone rubber, which can be easily stretched to more than 200%. However, inflating the soft element for a greater inflation distance would also affect the shape of the soft, inflated element. Therefore, the lug length is set to a conservative value to make sure the soft elements can be inflated without interference.

The lug thickness is indicated with the red arrow in Figure 6. Increasing the lug thickness will decrease the tip-tip distance, which is indicated with the orange arrow in Figure 6. The influence of the lug thickness on the wheel performance is not found in any literature. To investigate this, four motion simulations have been performed to investigate four different lug thicknesses: 2 mm, 5 mm, 10 mm and 15 mm. The performance of each configuration is evaluated by one KPI: the total distance travelled. The wheel thickness is then selected based on the outcomes of the simulations. These simulations are simulations with only rigid bodies to minimize the computational cost.

The lug spacing can be indicated with different measures, namely the tip-tip distance (see Figure 6), angle between two lugs or the number of lugs on the whole wheel. The lug spacing has influence on the traction, but also on the ability to traverse obstacles. In general, the smaller the lug spacing, the better the generated traction [43]. However, the tip-tip distance should be at least smaller than the rupture distance, which is dependent on the lug length and the granular material [43]. The soil in front of the lug is pushed, which creates a destructive phase in the soil. The rupture distance is the horizontal distance of the destructive phase of soil and is dependent on the internal friction angle of the soil [43]. A larger tip-tip distance is also beneficial for the traversing of obstacles, as the robot can climb larger obstacles when the tip-tip distance is larger. To investigate the optimal lug spacing for both soil and obstacles, a few simulations of different lug spacings have been performed. Three different configurations are evaluated: wheels with 6, 8 or 10 lugs. Some obstacles, composed of four spheres arranged in a pyramid shape, are added to evaluate the influence of the lug spacing on the obstacle climbing performance. The performance is evaluated using one KPI: the total distance travelled. Again, the simulations use only rigid bodies to minimize the computational cost.

3.2. Integrated Robot Design

The chassis of the robot is completely designed around the selected motors and corresponding electronics. Each wheel is individually driven by a single geared DC motor. The required motor torque is obtained by performing some simulations to measure the maximum torque on the wheels. The torque is estimated for a rotational speed of 3 rad/s (≈29 RPM) and 15 rad/s (≈143 RPM), which is set as the maximum speed the robot should achieve. The electronics are all selected based on the specifications of the selected motor. The chassis is designed around the motors and electronics to achieve an optimal, lightweight robot prototype. The battery, which is the heaviest component, will be placed in the middle of the chassis for an optimal weight distribution.

4. Design Results

The results of the design process are presented in this section. This includes the optimized wheel design, the soft, inflatable elements design and the integrated robot design. For the selection of the wheel parameters, locomotion simulations have been performed to optimize the lug thickness and the lug spacing. Four different lug thicknesses are evaluated by a simple locomotion simulation. The results, given in Table 4, show that the travelling performance decreases when the lug thickness increases. Therefore, the optimal lug thickness should be minimized, constrained only by the structural strength required to maintain integrity. Therefore, the lug thickness is set to 3 mm to ensure the structural integrity of the lugs.

Table 4: Total distances travelled for wheels with four different lug thicknesses.

lug thickness (mm)	distance travelled (mm)
2	620
5	610
10	580
15	540

For the lug spacing, three different configurations are evaluated. The results, given in Table 5, show that the travelling performance increases with an increasing number of lugs, which is as expected from the literature [43]. The selected number of lugs is 8, which is the best combination of a large tip-tip distance for the performance on obstacles and a high number of lugs for the performance on granular soils.

Table 5: Total distances travelled for wheels with three different lug spacings.

number of lugs	angle between lugs (deg)	tip-tip distance (mm)	distance travelled (mm)
6	60	47	710
8	45	35	770
10	36	28	830

The optimized design of the shape-adapting wheel is shown in Figure 7. The selected values for all five wheel parameters are given in Table 6. The wheel is 3D-printed and consists of two parts which can be connected. The lugs are not connected to the centre of the wheel, to leave space for the soft, inflatable elements. With this design, the soft, inflatable elements can be combined into one soft body, which requires only one air inlet instead of requiring separate air inlets for each element. The soft elements are placed between the lugs and are connected via a ring in the centre of the wheel. The two halves of the wheel are fastened with M3 bolts, securing the soft body inside. The soft inflatable element has been fabricated by pouring silicone rubber into a mold. The used material is the Smooth-On Ecoflex^{TM} 00-50 rubber. The Ecoflex^{TM} 00-50 material was selected from the available materials because it has the highest shore hardness (00-50). The air inlet is constructed by attaching a small tube on the outside of the soft part. A small throttle valve is inserted into the small tube to control the air pressure inside the soft part, as shown in Figure 7b. The assembled wheel is inflated by pressurizing the soft part via the throttle valve, which creates the inflated configuration of the wheel shown in Figure 7b.

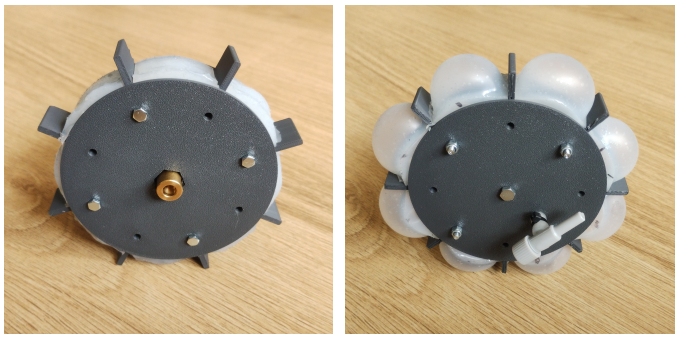

(a) deflated (b) inflated

Figure 7: Assembled wheel in inflated and deflated configuration.

The centre of the wheel is also connected to the motor via a coupling nut, which is visible in Figure 7a. The chassis of the robot is designed around the motors and electronic components, which results in the total prototype shown in Figure 8. For the motor selection, the required torque has been estimated by using locomotion simulations. The estimated nominal torque is 0.2 Nm and the estimated peak torque is 0.71 Nm. Therefore, a motor with a no-load speed of 200 RPM is required to ensure that the motor generates enough torque at the desired speed of approximately 143 RPM (15 rad/s). The stall torque of the motor should be above 1.0 Nm to ensure that enough torque is available at the desired motor speed. The 12 V geared DC motors are connected to the sides of the chassis. All the electronic components are placed on top of the robot chassis by using spacer nuts to create some air flow for the cooling. The motors are controlled using two dual motor drivers in combination with an Arduino. The input voltage of the motor drivers is regulated by two DC-DC converters. A lithium-ion polymer (LiPo) battery of 14.8 V powers the robot, placed in the middle of the chassis. The total weight of one wheel is around 135 g and the total weight of the prototype around 2.5 kg.

Table 6: Overview of the wheel parameters for the optimized wheel design.

wheel parameter	value
wheel diameter	120 mm
wheel thickness	20 mm
lug length	12 mm
lug thickness	3 mm
lug spacing	8 lugs

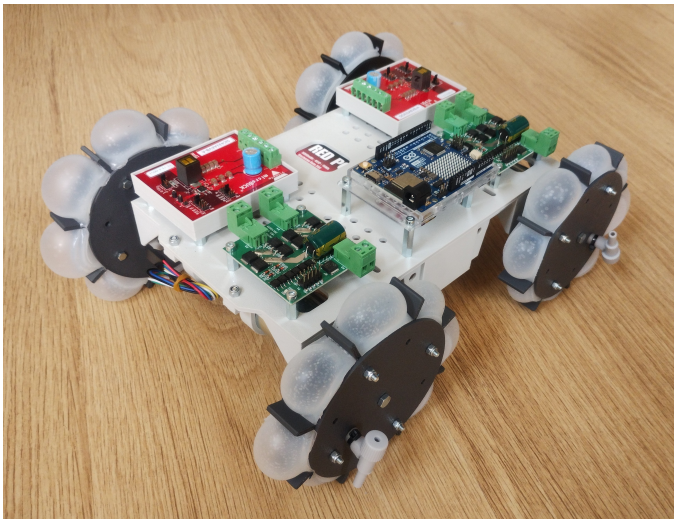

Figure 8: Isometric view of the assembled prototype with inflated wheels.

5. Prototype Locomotion Simulations

The performance of the prototype design is evaluated with various simulations of different cases and different soil types. Two configurations of the prototype have been evaluated. For the deflated configuration, shown in Figures 2 and 7a, the

Table 7: Overview of the prototype locomotion simulation results.

simulation case	configuration	granular soil type	simulation duration (s)	timestep (s) (Rayleigh %)	torque (%)	static sinkage (mm)	total distance travelled (mm)
slope	deflated	dry sand	3.0	2.5e-05 (≈18%)	75	25	754
slope	inflated	dry sand	3.0	5.0e-06 (≈5%)	75	13	639
slope	deflated	wet sand	3.0	2.5e-05 (≈18%)	50	16	1087
slope	inflated	wet sand	3.0	2.0e-05 (≈18%)	50	6	1234
slope	deflated	very wet sand	3.0	2.5e-05 (≈18%)	50	20	1170
slope	inflated	very wet sand	3.0	2.0e-05 (≈18%)	50	8	1197
obstacle	deflated	dry sand	2.5	2.5e-05 (≈18%)	50	24	753
obstacle	inflated	dry sand	2.5	7.0e-06 (≈5%)	50	12	891
obstacle	deflated	wet sand	2.5	2.5e-05 (≈18%)	50	15	1096
obstacle	inflated	wet sand	2.5	2.5e-05 (≈18%)	50	5	1278
obstacle	deflated	very wet sand	2.5	2.5e-05 (≈18%)	50	19	1142
obstacle	inflated	very wet sand	2.5	2.5e-05 (≈18%)	50	7	1242

wheels are modelled as rigid bodies. For this configuration, the soft, inflatable elements will not have any significant influence on the performance, since the granular soil contacts only the rigid sides of the wheel. The inflated configuration, shown in Figures 7b and 9, is simulated by using the discretized flexbody approach.

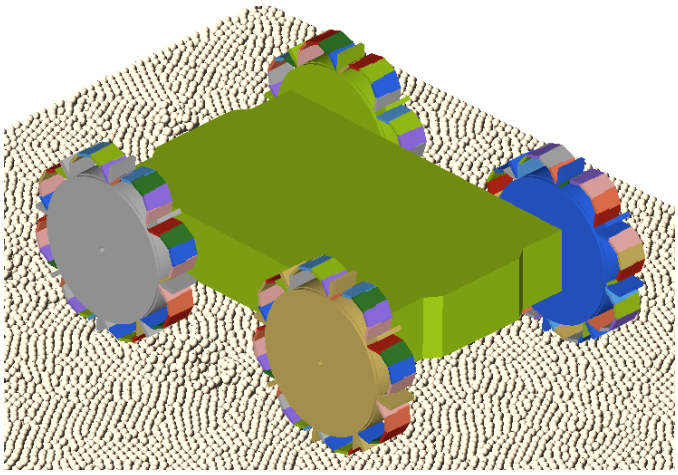

Figure 9: Simulation model of the prototype in inflated configuration.

The performance of the prototype is evaluated for two different cases. The first case is evaluating the performance of the prototype when climbing a slope of 20 degrees. The generated sand bed is shown in Figure 10a, where the total length, width and thickness of the sand bed are 1500 mm, 500 mm and 50 mm respectively. The second case is evaluating the performance of the prototype on a flat, sandy surface that includes a rigid 30x30 mm square beam obstacle, shown in Figure 10b. The dimensions of the flat sand bed are equal to the dimensions of the sloped sand bed. Both cases are evaluated for two configurations of the prototype across three types of sandy surfaces with varying moisture content. These surfaces are selected to represent different levels of soil cohesion: dry sand (low cohesion), wet sand (medium cohesion), and very wet sand (high cohesion). An overview of all simulations is given in Table 7, where also the timestep of each simulation is given. The motion of the wheels is generated by applying a certain torque, which is dependent on the angular velocity of the wheel, similar to the speed-torque relationship of a DC motor.

Simulations are evaluated using two KPIs: static sinkage and total distance travelled. Static sinkage refers to the vertical displacement of the prototype while it is stationary. Wheel motion begins after 0.5 seconds, allowing the prototype to sink into the sandy soil, enabling static sinkage to be estimated at 0.5 seconds. This metric is important, as it affects the prototype's travelling performance. Less sinkage can enable higher speeds, while greater sinkage may improve traction. The second KPI is the estimation of the total distance travelled by the prototype. This KPI reflects the prototype's overall locomotion capability and is used to assess how effectively the prototype moves across the sandy terrains.

The results of all simulations are presented in Table 7. In general, the sinkage of the inflated configurations is lower than for the deflated configurations. As a consequence, the effective wheel diameter is larger compared with the deflated configuration, which improves the travelling performance of the robot. The total distances travelled for each simulation on a sandy slope are also presented visually in Figure 11. This figure shows the inflated configuration has a better travelling performance than the deflated configuration on more cohesive sandy soils, due to the larger effective wheel diameter and less sinkage. For the loose, dry sand, the travelling performance is worse for the inflated configuration. It is observed that the inflated robot starts slipping in the loose, dry sand when climbing the slope. This is not the case for the deflated robot. Therefore, the deflated robot configuration with the lugged wheel outperforms the inflated configuration on loose, sandy slopes. The inflated

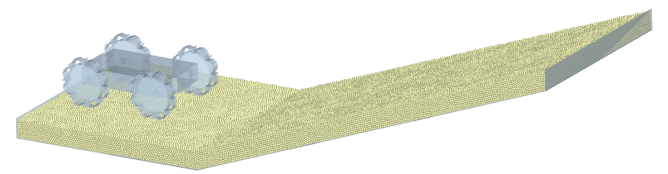

(a) sloped sand bed

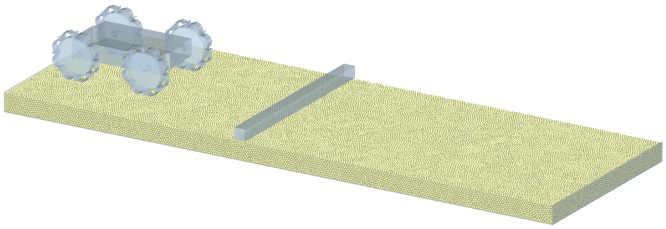

(b) flat sand bed with obstacle

Figure 10: Overview of the two different simulation cases.

configuration enables faster and more efficient locomotion on more cohesive sandy soils, where less sinkage occurs.

For the locomotion simulations with the obstacle, a clear pattern is observed in Figure 12. The inflated configurations are always performing better in travelling a flat sand bed with an obstacle. The total distance travelled for the inflated configurations is higher compared with the deflated configurations. When looking to the simulations it is observed that the inflated configurations tackles the obstacle more smoothly and efficiently than the deflated configuration. As a result, the climbing of the obstacle is much more efficient. Therefore, the inflated configuration is always a better choice for traversing obstacles. The soft, inflatable bodies can shape around the obstacles, providing strong grip on the obstacles, which enables fast and efficient movement. Even on the loose, dry sandy soil the inflated configuration still performs better than the deflated configuration.

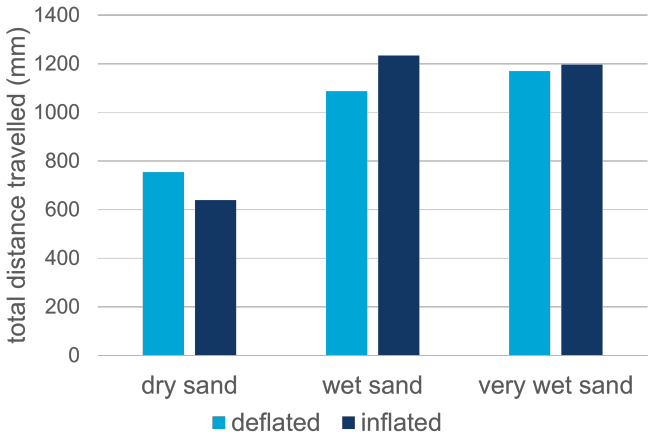

Figure 11: Prototype travelling performance on a sloped surface, simulated for three different sandy soils.

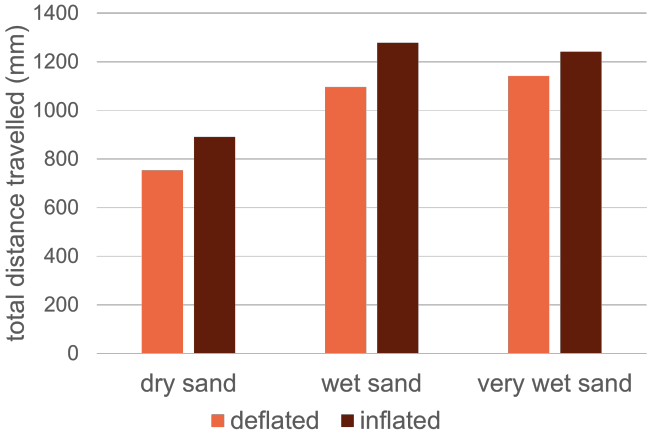

Figure 12: Prototype travelling performance on a flat surface with an obstacle, simulated for three different sandy soils.

6. Conclusions and Recommendations

Capturing the complex interactions between the robot and granular material involves integrating DEM with MBD simulations to simulate the behaviour of both the robot and the granular material. This simulation method is successfully used in the design process to evaluate the performance of different design configurations. A soft, shape-adapting wheel has been designed and a prototype is constructed. The performance of this prototype is evaluated with the locomotion simulations and the results clearly show the benefits of the shape-adapting wheel design. The use of DEM simulations makes it very easy to evaluate the robot performance on various granular terrains, for example on sandy terrains with a varying moisture content.

Various methods for robotic locomotion on granular surfaces are already available in literature. The most used locomotion methods were legged and wheeled locomotion, where a variety of designs already exist. Besides this, tracked, screw-based, undulatory and vibration-based locomotion methods are also possibilities that could be explored. KPIs related to manoeuvrability and traction are the most effective in assessing the travelling capabilities of a locomotion system.

The integration of DEM with MBD simulation is considered the most promising modelling approach for capturing robotic locomotion on granular terrain, as it allows for accurate modelling of both the robot and the granular terrain. The MBD component of the simulation accurately captures the robot's motion and dynamics, while the DEM component effectively models the behaviour of the granular terrain during interaction with the robot. The soft, flexible bodies can be accurately modelled by using a discretized flexbody representation. This method models the soft, flexible bodies as a chain of multiple rigid bodies, which are connected via bushings. The stiffness and damping is controlled by using multiple spring-damper systems.

The simulation method is used to support the design process. As a result, a shape-adapting wheel is designed, which can be shaped as a lugged wheel and a more circular wheel. Soft, inflatable elements have been placed between the lugs, which can

be inflated to change the shape of the wheel. Next to the wheel designs, a robot chassis is designed, which is optimized around the selected motors and electronics, resulting in a lightweight, small robotic prototype with shape-adapting wheels.

The performance of the prototype is only evaluated by simulations for two robot configurations, inflated and deflated, and for two different cases: a sloped sand bed and a flat sand bed including an obstacle. Each of these four different simulations is also evaluated for three different sandy soils: dry sand, wet sand and very wet sand. The interaction between the soft, flexible bodies and the granular soil or obstacles can be captured by the simulation, although it remains a simplified representation of reality, due to the small number of discrete bodies. The performance of the robotic system on exploring sandy terrains with obstacles is significantly better for the inflated wheel, because the soft elements in the wheel enhance the obstacle climbing performance. The deflated, lugged wheel configuration is performing significantly better on loose, dry sandy slopes where a lot of traction is required.

Future research on this topic should focus on utilizing more powerful computers to enhance accuracy and efficiency of the simulations. By using GPUs and high-performance computing, it becomes feasible to model more complex and softer deformable bodies without significantly increasing the computational time. An important direction for future research is the experimental evaluation of the prototype's performance, with the results to be compared to the simulations. Such comparisons would allow for a more thorough assessment of the simulation method's accuracy and help identify areas where the simulation model may require improvements.

On the design side, future work should explore variations in the geometry of the wheel. For example, the shape of the lugs could be made curved or triangular, which may enhance the travelling performance of the robot. The soft material could be reinforced with fibres to create a strain-limited layer, which can be used to control the deformation of the soft, flexible structures in the desired directions. Developing more rubber-like wheel constructions with embedded reinforcements could lead to more durable and reliable designs, better suited for the demands of robotic locomotion on unstructured, granular terrains. Combined with improved simulation models, a simulation-aided design approach would enable efficient performance evaluation of various design configurations, minimizing the need for physical prototyping and lowering the development costs.

Acknowledgements

The authors would like to acknowledge the support and resources made available by Altair Engineering for developing the simulation framework. We also thank Vittorio Garofano from the Transport Engineering and Logistics section at TU Delft for the insightful discussions and assistance in selecting the actuators and electronics of the prototype.

References

[1] United Nations. (2007) Percentage of total population living in coastal areas. [Online]. Available: https://www.un.org/esa/sustdev/natlinfo/indicators/methodology_sheets/oceans_seas_coasts/pop_coastal_areas.pdf

[2] A. Luijendijk, G. Hagenaars, R. Ranasinghe, F. Baart, G. Donchyts, and S. Aarninkhof, "The State of the World's Beaches," *Scientific Reports*, vol. 8, 4 2018.

[3] A. Giardino, J. Mulder, J. de Ronde, J. Stronkhorst, M. Shi, L. Zhu, M. Zhang, and L. Xu, "Sustainable Development of the Dutch Coast: Present and Future," *Journal of Coastal Research*, no. 61, pp. 166–172, 12 2011.

[4] H. Li, J. Sun, and M. Herrmann, "Beyond jamming grippers: granular material in robotics," *Advanced Robotics*, vol. 38, no. 11, pp. 715–729, 5 2024.

[5] Y. Wang and W. Wu, "A SPH Model Bridging Solid- and Fluid-Like Behaviour in Granular Materials," *Int. Journal for Numerical and Analytical Methods in Geomechanics*, vol. 49, no. 2, pp. 738–755, 2 2025.

[6] F. Cordes, F. Kirchner, and A. Babu, "Design and field testing of a rover with an actively articulated suspension system in a Mars analog terrain," *Journal of Field Robotics*, vol. 35, no. 7, pp. 1149–1181, 9 2018.

[7] S. Shrivastava, A. Karsai, Y. Ozkan Aydin, R. Pettinger, W. Bluethmann, R.O. Ambrose, and D.I. Goldman, "Material remodeling and unconventional gaits facilitate locomotion of a robophysical rover over granular terrain," *Science Robotics*, vol. 5, no. 42, 5 2020.

[8] J. Ma, M. Zhu, T. Zhang, and X. Yue, "The wheel-legged robot for granular terrain: Guardian," in *Proc. 28th Int. Conf. on Mechatronics and Machine Vision in Practice (M2VIP)*, 11 2022, pp. 1–6.

[9] H. Bagheri, V. Jayanetti, H.R. Burch, C.E. Brenner, B.R. Bethke, and H. Marvi, "Mechanics of bipedal and quadrupedal locomotion on dry and wet granular media," *Journal of Field Robotics*, vol. 40, no. 2, pp. 161–172, 9 2022.

[10] W.-H. Chen, H.-S. Lin, Y.-M. Lin, and P.-C. Lin, "TurboQuad: A Novel Leg–Wheel Transformable Robot With Smooth and Fast Behavioral Transitions," *IEEE Transactions on Robotics*, vol. 33, no. 5, pp. 1025–1040, 10 2017.

[11] S.-S. Yun, J.-Y. Lee, G.-P. Jung, and K.-J. Cho, "Development of a Transformable Wheel Actuated by Soft Pneumatic Actuators," *Int. Journal of Control, Automation and Systems*, vol. 15, no. 1, pp. 36–44, 1 2017.

[12] M.A. Elsheikh, "Design of a special rigid wheel for traversing loose soil," *Scientific Reports*, vol. 13, 1 2023.

[13] A.J.R. Lopez-Arreguin and S. Montenegro, "Towards bio-inspired robots for underground and surface exploration in planetary environments: An overview and novel developments inspired in sand-swimmers," *Heliyon*, vol. 6, 6 2020.

[14] J.H. Lugo, V. Ramadoss, M. Zoppi, and R. Molfino, "Conceptual design of tetrad-screw propelled omnidirectional all-terrain mobile robot," in *Proc. 2nd Int. Conf. on Control and Robotics Engineering (ICCRE)*, 4 2017, pp. 13–17.

[15] L. Huang, J. Zhu, Y. Yuan, and Y. Yin, "A dynamic resistive force model for designing mobile robot in granular media," *IEEE Robotics and Automation Letters*, vol. 7, no. 2, pp. 5357–5364, 4 2022.

[16] X. Chen, F. Gao, Z. Wang, S. Yao, G. Xu, and X. Yao, "Mechanism principle and dynamics simulation on variable diameter walking wheel," in *Proc. Second Int. Conf. on Digital Manufacturing & Automation*, 8 2011, pp. 723–727.

[17] J.V. Salazar Luces, S. Matsuzaki, and Y. Hirata, "RoVaLL: Design and Development of a Multi-Terrain Towed Robot With Variable Lug-Length Wheels," *IEEE Robotics and Automation Letters*, vol. 5, no. 4, pp. 6017–6024, 10 2020.

[18] Z. Liu, Z. Lu, and K. Karydis, "SoRX: a soft pneumatic hexapedal robot to traverse rough, steep and unstable terrain," in *Proc. IEEE Int. Conf. on Robotics and Automation (ICRA)*, 5 2020, pp. 420–426.

[19] L. Li, C. Zhao, S. He, Q. Qi, S. Kang, and S. Ma, "Enhancing undulation of soft robots in granular media: A numerical and experimental study on the effect of anisotropic scales," *Biomimetic Intelligence and Robotics*, vol. 4, 6 2024.

[20] D.T. Kühnel, T. Helps, and J. Rossiter, "Kinematic analysis of VibroBot: a soft, hopping robot with stiffness- and shape-changing abilities," *Frontiers in Robotics and AI*, vol. 3, 10 2016.

[21] H. Jin, J. Lin, W. Wu, Y. Lu, F. Han, and X. Shi, "Interaction mechanics model for screw-drive wheel of granary robot traveling on the loose grain terrain," *Journal of Field Robotics*, vol. 39, no. 6, pp. 827–839, 5 2022.

[22] P. Ravula, G. Acar, and B. Balachandran, "Discrete element method-based studies on dynamic interactions of a lugged wheel with granular media," *Journal of Terramechanics*, vol. 94, pp. 49–62, 1 2021.
[23] H. Jin, Y. Lu, W. Wu, and F. Han, "Influence of screw blades on the performance of a screw-drive granary robot," *Journal of Field Robotics*, vol. 41, no. 7, pp. 2133–2146, 6 2024.
[24] K. Gao, H. Wei, W. Xu, Z. Meng, X. Sun, and L. Sun, "Simulation and analysis of propulsive performance for screw propulsion inspection robot," *Powder Technology*, vol. 434, 2 2024.
[25] K. Zhang, J. Wu, Y. Zhang, and J. Shi, "Dust emission evaluation of the flexible metal wheel over lunar terrain and fender effect," *Mechanics Based Design of Structures and Machines*, vol. 52, no. 2, pp. 7522–7547, 1 2024.
[26] K. Zhang, Y. Zhang, J. Wu, and J. Shi, "Three-dimensional MFBD-DEM coupling simulation of flexible wire mesh wheel–soil over lunar rough terrain," *Computational Particle Mechanics*, 6 2024.
[27] Altair Engineering. What is DEM - Theoretical background behind the Discrete Element Method (DEM). [Online]. Available: https://altair.com/docs/default-source/resource-library/ebook_what_is_dem_theoretical_background_behind_the_discrete_element_method.pdf
[28] R. Bharadwaj, "Using DEM to solve bulk material handling problems," *Chemical Engineering Progress*, vol. 108, no. 9, pp. 54–58, 9 2012.
[29] Altair Engineering. Multibody Dynamics Simulation. [Online]. Available: https://help.altair.com/hwsolvers/os/topics/solvers/os/mbd_simulation_r.htm
[30] S. Cole. (2017, 10) Simulating soft soils in EDEM with the Soils Starter Pack. Altair Engineering. [Online]. Available: https://community.altair.com/discussion/33781/simulating-soft-soils-in-edem-with-the-soils-starter-pack
[31] Altair Engineering. The Soils Starter Pack. [Online]. Available: https://2024.help.altair.com/2024.1/EDEM/topics/creator_tree_bulk_material/the_soils_starter_pack_c.htm
[32] Altair Engineering. Hertz-Mindlin (no slip) Model. [Online]. Available: https://2024.help.altair.com/2024.1/edem/topics/creator_tree_physics/the_hertz_mindlin_no_slip_model_r.htm
[33] Altair Engineering. Hertz-Mindlin with JKR Model. [Online]. Available: https://2024.help.altair.com/2024.1/edem/topics/creator_tree_physics/the_hertz_mindlin_with_jkr_model_r.htm
[34] Altair Engineering. Edinburgh Elasto-Plastic Adhesion Model (EEPA). [Online]. Available: https://2024.help.altair.com/2024.1/edem/topics/creator_tree_physics/the_edinburgh_elasto_plastic_adhesion_model_eepa_r.htm
[35] C.J. Coetzee, "Review: Calibration of the discrete element method," *Powder Technology*, vol. 310, pp. 104–142, 4 2017.
[36] International Organization for Standardization. (2017) Geotechnical investigation and testing — Identification and classification of soil — Part 1: Identification and description.
[37] S. Lommen, M. Mohajeri, G. Lodewijks, and D. Schott, "DEM particle upscaling for large-scale bulk handling equipment and material interaction," *Powder Technology*, vol. 352, pp. 273–282, 4 2019.
[38] AZoMaterials. Silicone Rubber. [Online]. Available: https://www.azom.com/properties.aspx?ArticleID=920
[39] S. Farah, D.G. Anderson, and R. Langer, "Physical and mechanical properties of PLA, and their functions in widespread applications — A comprehensive review," *Advanced Drug Delivery Reviews*, vol. 107, pp. 367–392, 12 2016.
[40] C. Hu, J. Gao, J. Diao, and X. Song, "Numerical simulation of tire steering on sandy soil based on discrete element method," *AIP Advances*, vol. 11, 1 2021.
[41] Altair Engineering. MV-2000: Introduction to Flexible Bodies. [Online]. Available: https://2024.help.altair.com/2024.1/hwsolvers/ms/topics/solvers/ms/intro_to_flex_bodies_intro_r.htm
[42] M. Laîné, C. Tamakoshi, M. Touboulic, J. Walker, and K. Yoshida, "Initial design characteristics, testing and performance optimisation for a lunar exploration micro-rover prototype," *Advances in Astronautics Science and Technology*, vol. 1, pp. 111–117, 8 2018.
[43] M. Sutoh, K. Nagaoka, K. Nagatani, and K. Yoshida, "Evaluation of influence of surface shape of locomotion mechanism on traveling performance of planetary rovers," in *Proc. IEEE Int. Conf. on Robotics and Automation*, 5 2012, pp. 3419–3424.